An Operational Computational Terminal Area PBL Prediction System

NASA Grant NCC-1-220

Calendar Year 97 Annual Report

submitted to the
NASA Langley Research Center

Dr. Yuh-Lang Lin
Dr. Michael L. Kaplan

Department of Marine, Earth, and Atmospheric Sciences
North Carolina State University
Raleigh, North Carolina 27695-8208
Tel:/FAX: (919)515-1438/1683

February 1998

1. Objectives and Goals of the Research

There are two fundamental goals of this research project which are listed here in terms of priority, i.e., a primary and secondary goal. The first and primary goal is to develop a prognostic system which could satisfy the operational weather prediction requirements of the meteorological subsystem within the Aircraft Vortex Spacing System (AVOSS), i.e., an operational computational Terminal Area PBL Prediction System (TAPPS). The second goal is to perform indepth diagnostic analyses of the meteorological conditions during the special wake vortex deployments at Memphis and Dallas during August 95 and September 97, respectively. These two goals are interdependent because a thorough understanding of the atmospheric dynamical processes which produced the unique meteorology during the Memphis and Dallas deployments will help us design a prognostic system for the planetary boundary layer (PBL) which could be utilized to support the meteorological subsystem within AVOSS.

Concerning the primary goal, TAPPS Stage II was tested on the Memphis data and is about to be tested on the Dallas case studies. Furthermore benchmark tests have been undertaken to select the appropriate platform to run TAPPS in real time in support of the DFW AVOSS system. In addition, a technique to improve the initial data over the region surrounding Dallas was also tested and modified for potential operational use in TAPPS. The secondary goal involved several sensitivity simulations and comparisons to Memphis observational data sets in an effort to diagnose what specific atmospheric phenomena where occurring which may have impacted the dynamics of atmospheric wake vortices.

2. Work Accomplished During the Period 2/97-1/98

2.1 Advanced Mesoscale Analyses and Numerical Simulations of the Memphis August 95 Deployment Days

During early calendar year 97, several case studies from the Memphis 95 deployment were simulated with the MASS model (Kaplan et al. 1982; Bauman et al. 1997; Kaplan et al. 1997; Kaplan et al. 1998), which forms the focal point of TAPPS Stage II. Most of the analyses of results and comparisons with the special observational data sets prepared by MIT Lincoln

Table of Contents

Laboratory, involved four case studies, i.e., 11 August, 15 August, 16 August, and 24 August 1995. Of these simulations the 15 and 16 August simulations were the most interesting because of the extraordinary success of the 15th and the problems with the 16th. While the 11th and 24th were accurately simulated, the 15th and 16th represented examples of extremely accurate and disappointing simulations, respectively. Therefore, our focus was on diagnosing the problems with the simulation of the 16th and determining how to improve said simulation.

As can be seen in Figure 1b, we utilized a 29 km and 15 km nested-grid version of the MASS model for the numerical simulation experiments. Table 1 defines the model characteristics while Figure 1a depicts the 15 km average terrain near Memphis which was employed in the early simulation studies. All simulations were performed on a DEC-ALPHA 300 workstation in the Department of Marine, Earth, and Atmospheric Sciences at North Carolina State University.

We revisited the August 16 case study several times during calendar year 97 because of the inability of the MASS model to replicate the observed high frequency features in the MIT Lincoln Laboratory-generated wind and potential temperature profiles. In many ways this case study represents the ultimate forecast/simulation challenge because, as can be seen in Figures 2a and 2b, Memphis is firmly under a surface ridge of high pressure and time sections of observed cross runway (u wind velocity component) 5 minute flow show little indication of the prolonged dominance of easterly or westerly flow, unlike the 15th where a strong signal of a westerly jet is evident (Note Figures 3a and 3b). Furthermore, the simulation errors of ~0.5-1 m/s are on the order of the error in the observed wind profiles. It is most interesting that the strong signal of nocturnal jetogenesis both observed and simulated on the previous evening, i.e., 15 August, also occurred under a ridge of high pressure at the surface. This is to be expected as the meteorological scientific literature indicate that nocturnal jets form as a result of two processes: 1) the decoupling of the flow directly above the near-surface layer from friction by the intensification of a nocturnal radiational inversion, thus reducing the effect of frictional stresses which would allow the undiminished effects of the Coriolis force on atmospheric parcels (Blackadar 1957) and 2) accelerations accompanying local pressure gradients just above complex terrain resulting from the

differential radiational cooling above the sloping terrain relative to the nearby free atmosphere (McNider and Pielke 1981).

These two nocturnal jet mechanisms are very effective in producing a strong PBL vertical wind shear on the 15th of August, while much less effective on the 16th. As can seen in Figure 4, the 15 km numerical simulation of the 15 August jet produces a 4 m/s/40 m (0.1/s) shear zone near the 100 m level after 0530 UTC which in location, timing, and magnitude is very similar to the observations. This shear zone is responsible for the maximum of turbulence kinetic energy observed and simulated at Memphis. By contrasting the accurate simulation on the 15th (Figs. 3 and 4 versus 5 and 6) with the less than accurate simulation on the 16th it will become evident that we needed to perform indepth simulation studies to determine both how well and the modeling requirements which were necessary to simulate the less well-defined dynamics on the night of the 16th of August.

A close comparison of the observed mean sea level pressure observations valid at 0000 UTC on the 15th and 16th of August depicted in Figures 2a-2b unambiguously indicate that Memphis is under the sprawling ridge of high pressure oriented northeast-southwest from the Ohio River Valley to the Louisiana Gulf Coastal region. However, one can see that on the 15th a relatively pronounced northward-directed pressure gradient is evident between central Louisiana and northern Arkansas, and that on the 16th this feature is much weaker actually being surpassed in magnitude by the southwestward-directed pressure gradient located over the Ohio River Valley to the north. These differences reflect in part the slight westward shift in the ridge axis on the 16th relative to the 15th. Also evident from Figures 2c and 2d are the fact that during the 0000 UTC - 0600 UTC time periods on both nights there is a significant difference in the mean sea level pressure change fields. On the 15th the pressures rise from west of Memphis to eastern Oklahoma producing a larger scale eastward-directed pressure gradient force in time, while on the 16th the mean sea level pressure rise fields indicate maxima both to the west and east of Memphis. Therefore, Memphis is in between pressure rise zones and is isolated from a dominant large scale forcing mechanism. Hence, very small scale forcing mechanisms due to local pressure changes

can dominate on the 16th compared to the 15th. These subtle differences in the environment surrounding Memphis suggest unambiguously that dramatic differences in the observed local wind profiles observed in Figures 3a and 3b are at least somewhat influenced by the larger scale distribution of pressure near Memphis. However, it is not intuitively obvious how these larger scale pressure perturbations will affect the local winds at Memphis other than to enhance the westerly flow on the 15th and isolate Memphis in between two competing flows on the 16th. Therefore, numerical simulations are necessary to sort out the differences in forcing mechanisms responsible for the different wind regimes.

Figures 7-8 represent subtle differences in atmospheric forcing which are evident from the 15 km MASS model simulations. On the 15th, there is an unambiguous dominance of the northward-directed pressure gradient force on the 980 mb (~200 m level) just east of the Ouachita Mountains of west central Arkansas and just west of the Mississippi River Valley (Fig. 7a). This maximum reflects the combined effects of the background synoptic northward-directed low-level pressure gradient force over Louisiana and Arkansas, as well as the leeside nocturnal temperature gradient resulting from the difference between the elevated radiational cooling above the Ouachitas relative to the downstream free atmosphere over eastern Arkansas. Since the cooling reinforces the increase of pressure over the sloping mountains, a north-northeast/south-southwest ridge of high pressure just west of Memphis becomes evident in Figure 8a. This feature accelerates the flow towards the north which in time produces the shallow southwesterly jet most apparent on the 15th in Figure 7a during the 0400 UTC - 0600 UTC time period. This jet maximizes in magnitude near the 200 m level very similar to the observations in Figure 3a as the intense shallow inversion decouples the wind from the effects of surface friction allowing the Coriolis force to turn the northward-accelerated flow to the east.

On the 16th, significantly different and much more complex processes are at work. The 980 mb pressure gradient force vectors in Figure 7b indicate a less uniform distribution of south-southwesterly forcing when compared to the 15 August simulation. The significant southerly vectors are displaced to the southwest over southern Arkansas and northern Louisiana while a large

region of predominantly easterly vectors can be seen over northeastern Arkansas, western Alabama, western Kentucky, western Tennessee, and southern Illinois (Fig. 7b). A narrow local mesoscale maximum of northeasterly vectors is located from just northwest of Memphis to just southeast of Memphis. This very isolated feature reflects the very weak mesoscale trough and ridge which are oriented northwest to southeast from northeastern Arkansas to northeastern Mississippi in Figure 8b. This 100-150 km wide feature is apparently the result of the development of a local drainage flow of cold air off the shallow hills just east-northeast and east-southeast of Memphis and is so weak and isolated it is only apparent when a very detailed analysis of the local height distribution is performed. When we employ, as has been done in Figure 7b, the same contour height interval as Figure 7a, the area over Memphis and the adjacent hills appears to be isolated from any significant pressure gradient directly under a large scale high pressure ridge. These hills near Memphis were unable to produce a local pressure/temperature perturbation on the 15th because of the dominance of the larger scale pressure perturbation southwest of Memphis. However, the retrogression of the synoptic scale high pressure ridge over the region allowed virtually every terrain feature to produce a relatively subtle but not insignificant mass perturbation. This would render the more important radiationally-driven pressure rise zones: 1) to the west of Memphis and east of the Ouachita Mountains and 2) well east of Memphis and west of the Cumberland Plateau over central Tennessee less dominant in controlling the winds over Memphis. Hence, as can be seen in Figures 7b and 8b, local pressure rise zones develop just east of Memphis accompanying the local drainage flow over the slightly elevated hills to the east. Weak northeasterly flow accompanying the westward-directed pressure gradient near Memphis is capable of "counter-balancing" the stronger southwesterly jet east of the Ouachita Mountains which cannot "penetrate" as far east as Memphis unlike the 15th where the jet penetrated to just west of Nashville, Tennessee. However, a comparison between the observed (Figure 3b) and simulated (Figure 5b) time sections of u wind component indicate that while the model accurately indicates a very different flow regime from the 15th, the simulation of u wind component on the 16th leaves much to be desired at Memphis. In particular, the model indicates the observed transition from

predominately weak westerly to easterly flow in opposition to the pattern on the 15th. However, the timing of this transition is clearly late and, most importantly, the short period wind fluctuations evident in the lowest layers of the observations are not replicated in this particular simulation *at all.* Therefore, one could assume that the model is capturing the gross effects of the local drainage flow jet in retarding the eastward propagation of the west-southwesterly jet, yet is incapable in its present configuration of producing the magnitude and timing of the easterly jet's arrival as well as simulating the structure of the near-surface flow perturbations.

A strong indicator of the differences in the observed dynamics on the 15th and 16th are the Memphis microbarograph traces and 5 minute potential temperature time sections depicted in Figures 9-10. On close examination, it is apparent that the potential temperature time sections differ in two notable ways: first, the inversion is shallower and much more intense on the 16th relative to the 15th and second, longer period and larger amplitude waves appear in the potential temperature time sections on the 16th relative to the 15th. This dominance of wave signals is also apparent in the microbarograph trace from the 16th relative to the 15th as several 30-60 minute pressure increases ranging from 0.25 to 0.5 mb develop on the 16th, while much less wave activity is evident on the 15th. These differences indicate relatively higher numbers and larger amplitude of hydraulic phenomena on the 16th compared to the 15th. This is so because of the much more robust wave signals as well as the stronger inversion layer on the 16th indicating a much higher Brunt-Vaisala frequency and as specified by the Froude number:

$$Fr=NH/U \tag{1}$$

where N is the buoyancy frequency, H the terrain height, and U the wind velocity; the numbers on the 16th are indicative of highly subcritical flow relative to the 15th where the inversion is much weaker. Such a flow regime favors nonlinear hydraulic phenomena such as bores and hydraulic jumps which would form in conjunction with and ahead of a propagating density current accompanying a nocturnal drainage flow down from a local elevated plateau (e.g., Simpson 1987). Thus, the blocking effect of the synoptic scale high pressure region would allow the shallow

hydraulic phenomena to develop over the hills just east-northeast of Memphis and propagate southwestwards towards the airport. These phenomena would develop as cold air slowly drains off the plateau in a southwestward direction resulting in the impulsive forcing of more rapidly-propagating bores and hydraulic jumps on the inversion layer. These phenomena would be superimposed upon the background synoptic scale flow and mesoscale nocturnal jet signals in the Memphis wind profiles. However, the simulation of these phenomena represents a more daunting challenge for the numerical model. This is so because the wavelength of these slowly propagating features is very short both in the vertical and horizontal (Simpson 1987). For example, since the observed wind and theta perturbations have periods ~20-40 minutes and if we assume they are arriving from the hills ~15-20 km northeast of Memphis, that means an average of ~17.5 km in ~30 minute velocity of propagation or ~2.5 ms^{-1}. This assumes an approximate wavelength of 17.5 km. Hence, the numerical model horizontal resolution of ~15 km is clearly insufficient to resolve 17.5 km wavelengths, the model vertical resolutions of 10-20 m near the surface marginal at best for waves with a 30-60 m depth, and 15 km average terrain clearly not detailed enough to define the true structure of the hills northeast of Memphis which organize the nonlinear hydraulic phenomena.

In an effort to improve the simulation, enhancements to the terrain and model resolution were implemented for a series of simulation studies. Two additional simulation experiments were undertaken. First, the 15 km (8 minute) terrain data base constructed by averaging 15 km terrain observations was replaced by these actual nonaveraged terrain observations. This resulted in a less smoothed "silhouette" terrain depicted in Figure 11a which should be compared to the averaged terrain depicted in Figure 1a. This nonaveraged terrain, in turn, was interpolated to 7.5 km resolution as can be seen depicted in Figure 11b. This was utilized for a second nested-grid simulation to 7.5 km resolution. This allowed for the resolution of a north-south terrain gradient northeast of Memphis on the east side of the Mississippi River which was not resolved in the averaged terrain data base. It was hypothesized that these improvements in terrain would both enhance the accuracy of the simulated drainage flow just northeast of Memphis as well as the

accuracy of the hydraulic signals within the inversion below the drainage flow. Although, these resolutions are likely still nearly 100% too coarse to define the hydraulic waves accurately even with the model's fourth-order accurate advection scheme.

Figures 12a and 12b depict the 980 mb pressure gradient force for the for the 15 km nested-grid silhouette terrain and 7.5 km second (doubly) nested-grid silhouette terrain simulations. Quite obvious is the fact that the use of silhouette terrain and improved horizontal resolution in the 7.5 km simulation enhances the magnitude of the southwestward-directed pressure gradient force just northeast of Memphis with an approximate doubling of its magnitude in the 15 km silhouette terrain simulation (Fig. 12a) over the average terrain 15 km simulation (Fig. 7b) and a nearly 5-fold increase in its magnitude in the 7.5 km silhouette terrain simulation (Fig. 12b). Furthermore, with each model improvement the pressure gradient force maximum migrates further north-northwestward. This has profound effects on the simulated mass and momentum fields as can be diagnosed from Figures 13a-b and 14a-b. The higher resolution silhouette terrain simulations show a turning of the 980 mb flow north-northeast of and at Memphis to the east with larger magnitudes and earlier arrival easterly time periods than does the average terrain. As the model resolution is increased to 7.5 km, it is apparent that the simulated 980 mb heights are higher over the nearby hills just north-northeast of Memphis allowing a more distinct density current/drainage flow signal to develop as the nocturnal cooling precedes over these hills. The time sections of u wind velocity depicted in Figures 14a-b indicate an earlier and more robust signal of easterly flow arriving at Memphis as the terrain and horizontal resolution are improved. The 7.5 km simulation actually shows that the arrival of easterly flow is on time occurring just before 0430 UTC with a maximum magnitude of ~2 m/s. However, even the improved 7.5 km silhouette terrain simulation cannot replicate the lower-level and higher frequency hydraulic signals of near-surface wind maxima and minima which were observed and depicted in Figure 3b. The 7.5 km silhouette terrain virtual potential temperature fields depicted in Figure 15a clearly underestimate the magnitude of the observed theta perturbations depicted in Figure 10b and are clearly too deep in the simulation although they are beginning to display classic hydraulic jump and bore-like structures (note

Karyampudi et al. 1995). This is apparent in the cross section depicted in Figure 15b wherein undulations develop in the isentropic fields over the hill just east-northeast of Memphis but these undulations in the theta fields are too deep and too weak to produce the rapid wind period oscillations observed in the MIT Lincoln Lab time sections depicted in Figure 3b.

A comparison of simulated turbulence kinetic energy fields indicates that, in spite of the remaining inadequacies in the 7.5 km simulation on the 16th, the primary "spike" of observed turbulence kinetic energy depicted in Figure 4b is much better resolved in the 7.5 km simulation with silhouette terrain when compared to the 15 km average terrain simulation. Note Figures 6b, 16a-b, and 17 which depict the simulated 15 km average terrain MASS, 15 km silhouette terrain MASS, 7.5 km silhouette terrain MASS, and 29 km NWS MESO-ETA model time sections of turbulence kinetic energy, respectively. Clearly evident is the improvement in timing of the primary spike near 0500 UTC and the early and later weaker spikes by the most comprehensive MASS model simulation. This indicates that as the model physics improve, the key shear zone is better simulated even in a case where the local meso-gamma scale terrain effects dominate. Furthermore, the high frequency data sets available from MASS aid in its improved TKE calculations when compared to the sparse data available from the NWS MESO-ETA model. However, we clearly need to rerun the numerical model with at least twice the horizontal resolution and improved vertical resolution to properly resolve the hydraulic wave phenomena, i. e., 17.5 km nonlinear waves require at least five grid points to properly resolve them, hence, experiments are presently being performed with a 3.75 km grid as well as enhanced vertical resolution to determine if the numerical model can accurately replicate these phenomena. In addition, idealized numerical experiments with a 2-dimensional very high resolution (1 km horizontal and 1 m vertical) version of the North Carolina State University Geophysical Fluid Dynamics model are also underway to better understand the dynamics of the hydraulic phenomena observed at Memphis.

In summary, improved physics and numerics indicate that the most challenging forecast problems involving the Memphis deployment data sets are not insurmountable. The scenario evident on 16 August, where local forcing becomes very important resulting in density currents,

hydraulic jumps, and bores, represents an extreme challenge to potentially operational numerical weather prediction models and computational capabilities. However, we are very close to replicating these phenomena which could affect the dynamics of wake vortices on an operational basis.

2.2 Development and Testing of a Wind Profiler Mass Data Retrieval Technique

One of the most important problems in numerical weather prediction concerns the issue of the proper specification of the numerical model's initial conditions. Data bases used for model initialization typically lack the resolution of information necessary to properly specify the most detailed relationship among mass, momentum, internal energy, and water substance. This is exacerbated by the fact that the primary source of data for the initialization of numerical weather prediction models over North American continental locations, i.e., the rawinsonde, is available only every 12 hours and typically only every 200-400 km apart. Therefore, rawinsonde data is often not available if short period, i.e. 1-3 hour forecasts are to be made as are planned for TAPPS at Dallas. In an effort to fill these data gaps, the National Oceanographic and Atmospheric Administration (NOAA) recently implemented an operational network of 23 continuously recording wind profilers over the central United States (note Figure 18). This network provides hourly averages of wind velocity and direction from ~850 mb to the lower stratosphere. As can be seen in Figure 18, these observations are taken relatively close to Dallas, Texas, the location of the forthcoming AVOSS operational demonstration site. Most of the wind profilers are in nearby Oklahoma and Kansas. Hence, they could act as an important supplemental source of data for use in the development and operation of TAPPS when implemented for forecasting at the DFW airport. However, wind data without mass data represents a questionable source of information for use in numerical weather prediction models because unless the new winds and the existing model mass field are in the appropriate state of dynamical balance, artificial nonrepresentative imbalances can easily be generated which actually produce fictitious features in a numerical time integration which reduce the accuracy of a forecast. However, if the new wind data can be properly balanced with the mass field, especially if done so in a manner which *does not arbitrarily filter out mesoscale*

circulations, this data has the potential to significantly improve the accuracy of short-term mesoscale forecasts. Therefore, we deemed it appropriate to apply and improve an existing technique which retrieves mass information from profiler wind data as part of the initialization software for a potential operational system which includes TAPPS.

Cram et al. (1990), Karyampudi et al. (1995), and Adams (1996) report on a technique for synthesizing profiler-derived wind data with the complete two-dimensional velocity divergence equation. By using the complete unfiltered form of the divergence equation, a state of balance between the wind and mass field can be derived which allows for highly divergent circulations representative of the mesoscale motions which we want to simulate with TAPPS. Summarized briefly the technique is as follows:

Step (1): the two-dimensional velocity divergence equation

$$\frac{d\,(D)}{dt} = (D)^2 - \nabla\omega \bullet \frac{\partial V}{\partial P} + f\zeta + 2J\,(u,v) - \nabla^2\phi - \beta u + + \gamma v + \frac{\partial F_u}{\partial x} + \frac{\partial F_v}{\partial y} \qquad (2)$$

is expressed in a manner which allows for its iterative solution

$$\begin{aligned} -\,m^2\,\nabla^2\phi = {} & \frac{\partial D'}{\partial t} + m^2\left(u\,\frac{\partial D}{\partial x} + v\,\frac{\partial D}{\partial y}\right) + m^2\,(D)^2 + 2m^2\left(\frac{\partial v}{\partial x}\,\frac{\partial u}{\partial y} - \frac{\partial u}{\partial x}\,\frac{\partial v}{\partial y}\right) \\ & + \omega\,\frac{\partial D'}{\partial P} + m\left(\frac{\partial \omega}{\partial x}\,\frac{\partial u}{\partial P} + \frac{\partial \omega}{\partial y}\,\frac{\partial v}{\partial P}\right) - m\gamma v + m\beta u - f\zeta \equiv F \end{aligned} \qquad (3)$$

where m is the map factor and

$$D' = m^2\,\nabla \bullet V / m. \qquad (4)$$

Step (2): equation (3) is solved iteratively for a residual in an effort to derive the value of the geopotential heights:

$$\left(\Phi_1 + \Phi_2 + \Phi_3 + \Phi_4 - 4\,\Phi_0\right) - F = \hat{R} \qquad (5)$$

Step (3): finally, the hypsometric equation is utilized to derive hydrostatically consistent temperatures from the new height fields:

$$\phi(Z_u) - \phi(Z_l) = R \int_{P_u}^{P_l} T \, d \ln P = R\bar{T} \ln \frac{P_l}{P_u} \qquad (6)$$

This approach suffers from one fundamental limitation, i.e., because it does not include the effects of friction, it is less useful in its present form within the planetary boundary layer. Hence, in applying the technique, our goal was to improve it for use in the planetary boundary layer over the Great Plains where Dallas is located by including frictional forcing. Therefore, we first tested the technique in its nonfrictional form and then modified it to include friction for use over the Great Plains in both the stable and convective planetary boundary layers.

First, we will describe its use without friction over the Great Plains for the August 15 and 16, 1995 case studies. These two case studies represent powerful examples of why such a technique is so useful because of the observed mesoscale circulations which develop in between the rawinsonde times. Figure 19 depicts a sequence of NWS aviation surface analyses valid from 0200 UTC to 0800 UTC 15 August 1995. Evident is a strong inverted trough oriented northeast-southwest from the Texas Panhandle to southern Iowa. This feature represents a slow moving cold frontal boundary across which can be seen substantial surface wind shear and numerous reports of convection. Occurring as this circulation system does in between rawinsonde observation times, such a feature represents a short-term forecasting challenge as very little data exist above the earth's surface during this specific time period to initialize a numerical model in an effort to simulate said feature's short-term evolution. The utility of the profiler data becomes readily apparent for such a synoptic situation when one compares linearly time-interpolated (12-hourly) rawinsonde observations to actual hourly profiler-derived wind analyses at 850 mb as depicted in Figure 20. A comparison indicates that while the rawinsonde analyses shows virtually no indication of a low-level convergence zone, the hourly profilers clearly indicate an active region of converging winds accompanying multiple mesoscale circulations from western Texas to northwestern Missouri. As a matter of fact, two subsynoptic scale circulations are apparent during the 0200 UTC - 0600 UTC time period. One convergence zone which evolves into a vortex occurs near the Red River along the border of west Texas and Oklahoma. While this is occurring, another region of cyclonic

circulation persists near the Kansas and Missouri border regions. One can readily see in Figure 20 that these circulations evolve significantly over time periods as short as 2 hours in the profiler-derived analyses while very little change is apparent in the rawinsonde-derived wind fields over short time intervals.

Figure 21 depicts the evolution of linearly time-interpolated rawinsonde-derived 850 mb heights and those derived from the profiler data retrieval technique described above employing equations (2)-(6). Note that the profiler-derived height fields differ by as much as 30 m from the rawinsonde-interpolated fields. These differences include two persistent low pressure troughs in the height field. The most pronounced trough peaks in magnitude in between 0400 UTC and 0600 UTC over the Texas Panhandle and Red River Valley region along the western Texas-Oklahoma border. This feature includes the region surrounding Dallas. A second and somewhat weaker trough can be seen to fluctuate in amplitude over eastern Kansas and western Missouri. These troughs in the height field are a direct reflection of vortices in the profiler-derived wind fields. They unambiguously depict the short-period adjustment of the heights to the profiler-derived velocity divergence fields. As such they are considerably more representative of the observed rapidly-changing mesoscale weather conditions should initialization of a model be planned for the 0200 UTC-0600 UTC period. This profiler-derived information would be vital when initialization is contemplated in between rawinsonde observation times when compared to data which could be derived from earlier (0000 UTC) *synoptic scale* rawinsonde observations alone.

The second case study is very clearly typical of a nocturnal low-level jet over the Great Plains. Figure 22 depicts a sequence of NWS aviation surface observations valid from 0300 UTC through 0600 UTC 16 August 1995. While the cold front, inverted trough, and accompanying convection are no longer present as was the case on 15 August, a slowly-amplifying surface trough is evident from southeastern Colorado to the Red River Valley region of Texas. A local maximum of surface southerly wind flow is evident over the Texas and Oklahoma Panhandle regions as well as the western part of the Red River Valley. Figure 23 depicts the evolution of 850 mb time-interpolated rawinsonde winds in comparison to profiler-derived wind analyses from 0300 UTC -

0900 UTC 16 August. Most evident as differences between the two wind analyses is the developing wind maximum in between the Texas Panhandle and central Oklahoma during the 0300 UTC - 0500 UTC time period. This profiler-derived feature is twice as strong as the one in the interpolated rawinsonde analyses by 0500 UTC. Furthermore, the rawinsonde analyses do not capture the southerly wind maximum over western Kansas and central Nebraska as is evident in the profiler data analyses. By 0900 UTC there is a well-defined low-level jet in the profiler analyses extending from the western Red River region to northwestern Missouri.

The 850 mb height field comparisons depicted in Figure 24 reflect these wind differences as the development of dual troughs oriented northwest-southeast over the high plains region can be seen in the retrieved height field but not in the time-interpolated rawinsonde fields. One trough can be seen over the Texas and Oklahoma Panhandles and a second trough forms over central Kansas. These intensifying troughs in the height fields reflect the adjustment in the mass field to the accelerating wind flow from the Texas Panhandle to northern Kansas, therefore the cross-state height gradients are stronger by ~15% in the profiler-derived fields than in the time-interpolated rawinsonde data. The adjustment scheme acts to modify the height gradient to what it should be given the divergence in the profiler data accompanying the low-level jet features.

Finally, we will now describe the improvement to the mass retrieval scheme which we have formulated based upon the addition of friction. As was noted earlier, the frictional stress term has not previously been included in the total divergence equation for the retrieval of heights from profiler winds. This was done primarily because the profiler data sets did not include winds close to the earth's surface. Over the high plains, the earth's surface is much closer to the 850 mb level where profiler observations start. Therefore, the profiler data can be utilized for part of the boundary layer. A technique was formulated to include the frictional stresses in the divergence equation. The stresses were formulated assuming that both surface drag and turbulent mixing comprise the frictional force. These were approximated using formulations analogous to Bluestein and Crawford (1997). The algorithm requires an estimation of the height of the planetary boundary layer. Since the observations do not tell us this, we must use a first guess coarse mesh

MASS model simulation to provide a first guess of the height of the PBL. Once this estimate is known at a location and time, the retrieval technique has been modified to logarithmically interpolate the profiler and observed surface wind data to determine the wind profile at the top of the PBL. This information in turn is used to calculate the frictional stresses due to surface drag employing a bulk aerodynamic formulation and the turbulent stresses using the covariance relationships among the horizontal and vertical wind velocities employing Prandtl mixing length theory. Once these frictional stresses are formulated they are differentiated to produce a frictional force term in the divergence equation as noted by term 10 in equation (2). Said force then is available to include in the forcing function for the divergence equation which is, in turn, relaxed to determine the height residual as specified in equations (2-6). Employing the 15 and 16 August 1995 case studies during both the stable and convective PBL have revealed that the frictional term is very weak contributing only a meter or two height perturbation as can be diagnosed from the comparisons for the 0900 UTC and 1900 UTC time periods for the 15 August case study depicted in Figure 25. Here one can see that for this case study, as was the case for the 16 August case study, the addition of the frictional force has minimal impact of ~<1 m for the stable and ~1 m for the unstable PBL. However, these are weak midsummer case studies and therefore one could speculate that during a strong dryline case study or an intense cyclone case study, the frictional stresses might very well have a much larger magnitude and, therefore, have a greater impact on the magnitude of the retrieved height data.

2.3 Testing TAPPS During Nocturnal PBL Jetogenesis Over the Great Plains

As described in the previous section, the night of August 16 produced a classic low-level jet over the southern and central Great Plains. Because of this jet's location, i.e., near Dallas, it represented an opportunity to test the ability of the TAPPS Stage II system to simulate a representative Great Plains nocturnal jet. Recent observational climatological studies such as those by Mitchell et al. (1995), Whiteman et al. (1997) and Arritt et al. (1997) highlight the shallow nature of these jets often maximizing as low as 300 m above the surface of the elevated Great Plains.

As can be seen in Figure 23 a pronounced 850 mb south-southwesterly wind maximum develops over the Oklahoma and Texas Panhandle region by 0400 UTC 16 August. This feature occurs in response to both the formation of a nocturnal inversion layer and differential cooling above the sloping High Plains surface and the adjacent atmosphere. In time, the jet builds northeastwards so by 1200 UTC it extends from the Texas Panhandle to northern Missouri (note Fig. 26d). Quite evident from the rapidly-evolving profiler analyses in Figure 23, but not so evident in the rawinsonde analyses, is the development of a region of slower wind velocities just northwest of the core of the low-level jet over northwestern Kansas. The simulation of this speed minimum feature represents a special challenge for the modeling system. The bold northwest-southeast-oriented line on Figure 26a represents the location of a vertical cross section of model-simulated winds depicted in Figure 27 where we will determine if the model can capture this crucial mesoscale zone of reduced wind velocities over northwestern Kansas as well as the finescale structure of the jet's wind maximum. The TAPPS Stage II system comprised of a 15 km resolution version of the MASS model employing average terrain was initialized from NCAR reanalyses data sets, reanalyzed rawinsonde, and surface data sets at 0000 UTC 16 August for a 12 hour simulation.

Figure 26 depicts the 850 mb winds and heights simulated over the central Great Plains by the numerical model and valid at 0600 UTC, 0900 UTC, and 1200 UTC 16 August 1995. By 0600 UTC, a southerly jet forms from the western part of the Red River Valley region of Texas into southwestern Nebraska. As can be seen in Figures 26 and 27, the core of this jet forms over the border region encompassing the Texas and Oklahoma Panhandle region just above the inversion layer at between 300 and 500 m above the earth's surface. The location in the vertical is consistent with recent climatologies such as those by Mitchell et al. (1995), Arritt et al. (1997), and Whiteman et al. (1997) and in the horizontal is quite consistent with the profiler observations depicted in Figure 23. Quite interesting is the fact that the flow is directed to the left of the simulated height field indicative of a wind field which is accelerating in response to rapid pressure falls accompanying leeside troughing east of the Colorado Rocky Mountains. This troughing can

be inferred from Figure 24 where the retrieved height fields indicate an intensifying trough oriented southeastward from Colorado to the Oklahoma Panhandle during this time period. By 0900 UTC, Figures 26 and 27 unambiguously indicate that the core of the 850 mb jet is propagating north-northeastwards into southwestern Kansas as the individual wind vectors turn from a southerly to southwesterly direction analogous to the observations depicted in Figure 23. Hence, the isallobaric forcing evident at and likely well before 0600 UTC is being replaced by an inertial-advective response driven by the Coriolis force after 0600 UTC which is highly typical of a Great Plains nocturnal low-level jet. Figures 26-27 show that by 1200 UTC, the jet continues to build northeastward into Missouri with the maximum values broken into two lobes, i.e., one lobe just northwest of Wichita, Kansas and a second lobe over the Texas Panhandle. These simulated fields are consistent with the profiler observations which indicate this split into multiple wind maxima. Furthermore Figures 26-27 also indicate that the numerical model is capable of simulating the observed profiler-derived wind velocity minimum over northwestern Kansas. Both the simulated and observed fields indicate that this minimum over northwestern Kansas lies to the southeast of another jet over north central and northwestern Nebraska. Hence, the simulated fields are in good agreement with the temporally-evolving mesoscale features observed in the profiler data sets. This includes the simulated 850 mb heights which are quite consistent with the profiler-derived height fields over the Plains as can be seen by comparing Figures 24 and 26. Finally, by 1200 UTC, the simulated jet reaches its maximum intensity along the cross sections depicted in Figure 27 of >16 m/s just southeast of Wichita consistent with observations. Figure 26 depicts the strongest vertical wind shears at this time of ~6 m/s/180 m or ~.033/s. The intensity of the simulated jet is very similar to the observed jet depicted in Figure 23.

2.4 Rawinsonde Data Gathering and Meteorological Overview During the DFW Deployment

During the second half of September, 1997, North Carolina State scientists participated in the Dallas AVOSS deployment. The purpose of the deployment was to gather data on the effect of meteorological conditions on wake vortex evolution. In particular, our interest was in coordinating the launching and collection of rawinsonde data for use in verifying numerical model simulations of the Dallas deployment case studies.

Five balloon sites were active during the 10 day period which included 15-19 and 22-26 September. These were located at: 1) the DFW airport north site, 2) Waxahatchie, Texas, 3) Plano, Texas, 4) the Fort Worth, Texas National Weather Service office, and 5) Denton, Texas. Balloons were launched at 0900 UTC, 1200 UTC, 1500 UTC, 2100 UTC, 0000 UTC, and 0300 UTC each day up to the 300 mb level in an effort to capture the transitional boundary layer dynamics and the upper-air dynamical processes above the boundary layer. All but a small number of the balloon launches were successful. These data were then archived at North Carolina State University for comparison to 1998 simulations employing the TAPPS Stage II and III systems.

During the first week of the deployment, a massive area of high pressure covered the region surrounding Dallas. This afforded the collection of data on several days where relatively uninterrupted diurnal PBL evolution occurred. This included nocturnal jets during the stabilizing PBL and a deep well-mixed convective PBL with extraordinarily hot surface temperatures. The second week was marked by transient cyclonic disturbances more indicative of early autumn in north Texas.

3. Work in Progress and Objectives for the Period 2/98-1/99

3.1 DFW Deployment Simulations

At present, we are performing simulation experiments with the TAPPS Stage II system. These simulations include two "coarse" mesh 60 km horizontal resolution simulations for each 15 hour period during which special rawinsonde observations were acquired including the periods from the 15th-19th and the 22nd-26th of September 97. The 60 km "coarse" mesh simulations

initialized at 0000 UTC from NCAR reanalyses data sets and rawinsonde as well as surface data were integrated through 1500 UTC and then nested at 0300 UTC each day and integrated foreward in time until 1500 UTC for 12 hour 10 km "fine" mesh simulations for the morning PBL dynamics. For the afternoon/evening PBL dynamics, a 60 km run was initialized at 1200 UTC and integrated through 0300 UTC and then nested to 10 km at 1500 UTC and integrated through 0300 UTC the next day. These simulations employ version 5.10 of the MASS model including 50 vertical layers, a 40x40 point "coarse" and 80x80 point "fine" mesh horizontal matrix of grid points, and silhouette terrain. During the remaining period of the winter and spring of calendar year 1998 these simulations will be completed and direct comparisons made between model-simulated fields and observed soundings at all five rawinsonde balloon sites.

3.2 DFW Deployment Observational Analyses

We are presently analyzing the Dallas deployment rawinsonde observations. This involves producing high resolution analyses at all mandatory levels, every 25 mb within the PBL, as well as the earth's surface of standard dependent variables from information compiled from the five balloon sites. These analyses fields will soon be employed for direct comparisons to the model-simulated data sets over Dallas and the nearby region at the same times.

3.3 TAPPS Stage II Operational System Benchmark Testing

We are presently performing benchmark tests with the TAPPS Stage II system on various computer workstations. Our first test was performed in December 1997 utilizing a 200 megahertz SUN-ULTRA computer system with 1 processor. This test included a 60 minute real-time simulation employing the MASS model version 5.10 with a 60x55x50 grid point matrix and 15 km horizontal resolution. This yielded an ~2.5:1 ratio of real time to wall clock time. We have just completed the process of benchmarking the same model version on a much faster DEC-ALPHA with a 433 megahertz processor. This benchmark produced an improvement over the SUN-ULTRA system to a ~5.2:1 ratio of real time to wall clock time. This indicates that an existing DEC-ALPHA system with a 533 megahertz processor will be very close to being fast enough to run TAPPS Stage II in real-time for the Dallas AVOSS operational system later this calendar year.

Simple linear extrapolation would allow such a system to produce a ~6.4:1 ratio of real time to wall clock time. We will be benchmarking the model on this 533 megahertz in preparation for possible use in real-time.

3.4 TAPPS Stage II Development and Implementation for DFW

We are presently in the process of planning the operational system configuration for TAPPS Stage II at DFW later in calendar year 1998. We will be spending the next six months preparing the software for its operational implementation planned to be late in the summer of calendar year 1998. One of the improvements which will be available for the operational model will be the addition of a 1 km silhouette terrain data base.

3.5 TAPPS Stages III-IV Research and Development Effort

We will be testing the TASS model (Proctor 1998) with initial conditions and lateral boundary conditions derived from the nested- grid MASS model simulations. This represents a movement towards a TAPPS which includes high resolution and LES simulations from TASS initialized from the MASS nested-grid model.

4. Acknowledgments

The principal investigators wish to sincerely thank Dr. F.H. Proctor, D.A. Hinton, and B. Perry at NASA LaRC for their support, and Dr. R.P. Weglarz at NC State University for performing all the MASS model simulations and for discussions on interpreting model results.

We also thank Mr. Dan Shaltanis for his work with the Midwest profiler data, and Mr. Darrell Ensley for help postprocessing model data using GEMPAK meteorological software. We sincerely wish to thank Mel DeFeo for her time and efforts in helping draft the final version of this report.

5. References

Adams, M. E., 1996: Terrain-induced midtropospheric frontogenesis and jet streak development during STORM-FEST IOP-17, 8 and 9 March 1992. *PhD. Dissertation*, Department of

Marine, Earth, and Atmospheric Sciences, North Carolina State University, Raleigh, NC 27695-8208. 214 pp.

Arritt, R. W., T. D. Rink, M. Segal, D. P. Todey, C. A. Clark, M.J. Mitchell, and K. M. Labas, 1997: The Great Plains low-level jet during the warm season of 1993. *Mon. Wea. Rev.*, **125**, 2176-2192.

Bauman W. H. III, M. L. Kaplan, and S. Businger, 1997: Nowcasting convective activity for space shuttle landings during easterly flow regimes. *Wea. Forecasting*, **12**, 79-107.

Blackadar, A. K., 1957: Boundary layer wind maxima and their significance for the growth of the nocturnal inversion. Bull. Amer. Meteor. Soc., 38, 283-290.

Bluestein, H. B., and T. M. Crawford, 1997: Mesoscale dynamics of the near-dryline environment: Analysis of data from COPS-91, 1997: *Mon. Wea. Rev.*, **125**, 2161-2175.

Cram, J. M., M. L. Kaplan, C. A. Mattocks, and J. W. Zack, 1991: The use and analysis of profiler winds to derive mesoscale height and temperature fields: Simulation and real data experiments. *Mon. Wea. Rev.*, **119**, 1040-1056.

Kaplan, M.L., J. W. Zack, V. C. Wong, and J. J. Tuccillo, 1982: Initial results from a mesoscale atmospheric simulation system and comparison with the AVE-SESAME I data set. *Mon. Wea. Rev.*, **110**, 1564-1590.

_____, S. E. Koch, Y.-L. Lin, R. P. Weglarz, and R. A. Rozumalski, 1997: Numerical simulations of a gravity wave event over CCOPE. Part I: The role of geostrophic adjustment in mesoscale jetlet formation. *Mon. Wea. Rev.*, **125**, 1185-1211.

_____, R. P. Weglarz, Y.-L. Lin, and D. Shaltanis, 1998: The predictability of shallow terrain-induced meso-beta scale jetogenesis within the nocturnal PBL. Preprints, *12th Conference on Numerical Weather Prediction*, Amer. Meteor. Soc., Phoenix, AZ, 65-68.

Karyampudi, V. M., M. L. Kaplan, S. E. Koch, and R. J. Zamora, 1995; The influence of the Rocky Mountains on the 13-14 April 1986 severe weather outbreak. Part I: Mesoscale lee cyclogenesis and its relationship to severe weather and duststorms. *Mon. Wea. Rev.*, **123**, 1394-1422.

_____, S. E. Koch, C. Chen, J. W. Rottman, and M. L. Kaplan, 1995: The influence of the Rocky Mountains on the 13-14 April 1986 Severe Weather Outbreak. Part II: Evolution of a prefrontal bore and its role in triggering a squall line. *Mon. Wea. Rev.*, **123**, 1423-1446.

McNider, R. T. and R. A. Pielke, 1981: Diurnal boundary layer development over sloping terrain. *J. Atmos. Sci.*, **80**, 165-189.

Mitchell, M. J., R. W. Arritt, and K. Labas, 1995: A climatology of the warm season Great Plains low-level jet using wind profiler observations. *Wea. Forecasting*, **10**, 576-591.

Proctor, F. H., 1998: The NASA-Langley Wake Vortex Modelling Effort in Support of an Operational Aircraft Spacing System. AIAA 98-0589, Preprints, *36th Aerospace Sciences Meeting and Exhibit*, American Institute of Aeronautics and Astronautics, Reno, Nevada, 19 pp.

Simpson, J. E., 1987: *Gravity Currents in the Environment and the Laboratory*. John Wiley and Sons, New York, NY, 244 pp.

Whiteman, C. W., X. Bian, and S. Zhong, 1997: Low-level jet climatology from enhanced rawinsonde observations at a site in the southern Great Plains. *J. Appl. Meteor.*, **36**, 1363-1376.

6. Papers Submitted in Calendar Year 1997-1998

Kaplan, M. L., R. P. Weglarz, Y.-L. Lin, and D. Shaltanis, 1998: The predictability of shallow terrain-induced meso-beta scale jetogenesis within the nocturnal PBL. Preprints, *12th Conference on Numerical Weather Prediction*, American Meteorological Society, Phoenix, Arizona, 65-68.

7. Papers in Preparation in Calendar Year 1997-1998

Kaplan, M. L., R. P. Weglarz, Y.-L. Lin, D. Shaltanis, and D. Ensley, 1998: The predictability of shallow terrain-induced meso-beta scale jetogenesis and hydraulic surges within the nocturnal PBL. In preparation, *Mon. Wea. Rev.*

8. List of Tables

9. List of Figures

8. MASS nested-grid 15 km average terrain simulation of 980 mb height (solid in m), wind vectors, wind velocity (shaded > 5 m/s), and temperature (dashed in C) valid at ~0430 UTC a) 15 August 1995 and b) 16 August 1995.

9. Observed National Weather Service microbarograph trace (in.) valid from ~0000 UTC 15 August 1995 to ~1900 UTC 16 August 1995. Arrows highlight key evening periods on the 15th and 16th in between 0000 UTC and 0500 UTC.

10. Observed time sections of 200 m deep vertical profiles of potential temperature (K) at Memphis, Tennessee valid from 0300 UTC to 0600 UTC a) 15 August 1995 and b) 16 August 1995.

11. a) Analysed 15 km silhouette terrain (m) MASS model data base employed in the Memphis 95 simulations. b) Analysed interpolated 7.5 km silhouette terrain (m) MASS model data base employed in the Memphis 95 simulations.

12. a) MASS nested-grid 15 km silhouette terrain simulation of 980 mb pressure gradient force vectors ($m/s^2 \times 10^5$) valid at ~0430 UTC 16 August 1995. b) MASS doubly nested-grid 7.5 km silhouette terrain simulation of 980 mb pressure gradient force vectors ($m/s^2 \times 10^5$) valid at ~0445 UTC 16 August 1995.

13. a) MASS nested-grid 15 km silhouette terrain simulation of 980 mb height (solid in m), wind vectors, wind velocity (shaded > 5m/s), and temperature (dashed in C) valid at ~0500 UTC 16 August 1995. b) MASS doubly nested-grid 7.5 km silhouette terrain simulation of 980 mb height (solid in m), wind vectors, wind velocity (shaded > 5m/s), and temperature (dashed in C) valid at ~0500 UTC 16 August 1995.

14. a) MASS nested-grid 15 km silhouette terrain simulation of a time section of 200 m deep vertical profiles of u wind velocity component (m/s) at Memphis, Tennessee valid from 0200 UTC to 0600 UTC 16 August 1995. b) MASS doubly nested-grid 7.5 km silhouette terrain simulation of a time section of 200 m deep vertical profiles of u wind velocity component (m/s) at Memphis, Tennessee valid from 0200 UTC to 0600 UTC 16 August 1995.

15. a) MASS doubly nested-grid 7.5 km silhouette terrain simulation of a time section of 200 m deep vertical profiles of virtual potential temperature (K) at Memphis, Tennessee valid from 0200 UTC to 0600 UTC 16 August 1995. b) MASS doubly nested-grid 7.5 km silhouette terrain simulation vertical cross section from Little Rock, Arkansas (LIT) to Nashville, Tennessee (BNA) of potential temperature (thick solid in K), wind vectors (m/s), and omega (thin solid downward and thin dashed upward in microbars/s) valid at 0500 UTC 16 August 1995.

16. a) MASS nested-grid 15 km silhouette terrain simulation of a time section of 200 m deep vertical profiles of turbulence kinetic energy (m^2/s^2) at Memphis, Tennessee valid from 0200 UTC to 0600 UTC 16 August 1995. b) MASS doubly nested-grid 7.5 km silhouette terrain simulation of a time section of 200 m deep vertical profiles of turbulence kinetic energy (m^2/s^2) at Memphis, Tennessee valid from 0200 UTC to ~0630 UTC 16 August 1995. Shaded areas have Richardson numbers <0.25.

17. National Weather Service MESOETA model simulation of a time section of 200 m deep vertical profiles of turbulence kinetic energy (m^2/s^2) at Memphis, Tennessee valid from 0300 UTC to 0600 UTC 16 August 1995. Shaded areas have Richardson numbers <0.25.

18. Location of the NOAA operational wind profiler network (asterisks) relative to the standard NOAA operational rawinsonde network (stars) and the NCAR special experiment CLASS sounding sites (circled stars) over the Great Plains (Source-Adams (1996)).

19. National Weather Service observed mean sea level pressure (mb) and surface weather analyses valid at a) 0200 UTC, b) 0400 UTC, c) 0600 UTC, and d) 0800 UTC 15 August 1995.

20. Comparisons of analyses of linearly temporally interpolated 12-hourly 850 mb rawinsonde and hourly profiler wind vectors and isotachs (m/s) valid at a) 0200 UTC, b) 0400 UTC, c) 0600 UTC, and d) 0800 UTC 15 August 1995.

21. Comparisons of analyses of linearly temporally interpolated 12-hourly 850 mb rawinsonde-derived height and hourly profiler-retrieved height (m) valid at a) 0200 UTC, b) 0400 UTC,

c) 0600 UTC, and d) 0800 UTC 15 August 1995. Differences between retrieved and interpolated fields (m) are shown as dashed lines.

22. National Weather Service observed mean sea level pressure (mb) and surface weather analyses valid at a) 0300 UTC, b) 0400 UTC, c) 0500 UTC, d) 0600 UTC, and e) 0900 UTC 15 August 1995.

23. Comparisons of analyses of linearly temporally interpolated 12-hourly 850 mb rawinsonde and hourly profiler wind vectors and isotachs (m/s) valid at a) 0300 UTC, b) 0400 UTC, c) 0500 UTC, d) 0600 UTC, and e) 0900 UTC 16 August 1995.

24. Comparisons of analyses of linearly temporally interpolated 12-hourly 850 mb rawinsonde-derived height and hourly profiler-retrieved height (m) valid at a) 0300 UTC, b) 0400 UTC, c) 0500 UTC, d) 0600 UTC, and e) 0900 UTC 16 August 1995. Differences between retrieved and interpolated fields (m) are shown as dashed lines.

25. a) Comparisons of profiler-retrieved 900 mb height (m) for the nocturnal PBL with no friction (thick solid) and friction (thick dashed) and valid at 0900 UTC 15 August 1995. Differences between friction and no friction (m) are shown as thin solid and dashed. b) Comparisons of profiler-retrieved 900 mb height (m) for the convective PBL with no friction (thick solid) and friction (thick dashed) and valid at 1900 UTC 15 August 1995. Differences between friction and no friction (m) are shown as thin solid and dashed.

26. MASS nested-grid 15 km average terrain simulation of 850 mb height (solid in m), wind vectors and velocity (shaded >5m/s), and temperature (dashed in C) valid at a) 0600 UTC, b) 0900 UTC, and c) 1200 UTC 16 August 1995. d) Observed 850 mb profiler wind vectors and isotachs (m/s) valid at 1200 UTC 16 August 1995.

27. MASS nested-grid 15 km average terrain simulation of a vertical cross section from Scottsbluff, Nebraska (BFF) and Memphis, Tennessee (MEM) of potential temperature (K), wind vectors and velocity (shaded >5m/s), and temperature (dashed in C) valid at a) 0600 UTC, b) 0900 UTC, c) 1200 UTC 16 August 1995. Location of vertical cross section depicted in Figure 26a.

Table 1: MASS 5.10 model components (Source-MESO Inc.)

Summary of MASS Version 5.10

Initialization
• 3-D multivariate OI procedure used to blend a first guess fields (e.g. previous MASS simulation, NCEP model output, archived GOI data etc.) with observations from a variety of sensing systems (e.g. surface, rawinsonde etc.)
• Synthetic relative humidity profiles derived from surface cloud observations, pilot reports, manually digitized radar (MDR) data and infrared and visible satellite data
Numerical Techniques
• Hydrostatic primitive equations in terrain-following (s_p) vertical coordinate with 4th order accurate finite differencing
• MPDATA positive definite advection scheme
• One-way interactive nesting with arbitrary coarse/fine grid spacing ratio and unrestricted number of nested domains
Boundary Layer/ Surface Physics
• TKE (k-e) or Blackadar boundary layer parameterization with surface layer based on similarity theory formulation
• Surface energy budget includes separate equations for soil and the vegetation canopy and heterogeneous subgrid scales areas
• Surface hydrology includes budget equations for three moisture reservoirs (cover layer, shallow and deep soil layers) and snow cover which incorporates the effects of accumulation, settling, melting and sublimation
Moisture Physics
• Option of diagnostic or prognostic scheme. Prognostic equations for cloud water, cloud ice, rain water and snow using a bulk microphysics parameterization
• Option of Kuo-type cumulus parameterization with moist downdraft physics or Fritsch-Chappell scheme
Radiation
• Longwave and shortwave radiation parameterized in surface energy budget and in the free atmosphere. Interaction with atmospheric water vapor, liquid/frozen water, and parameterized sub-grid clouds

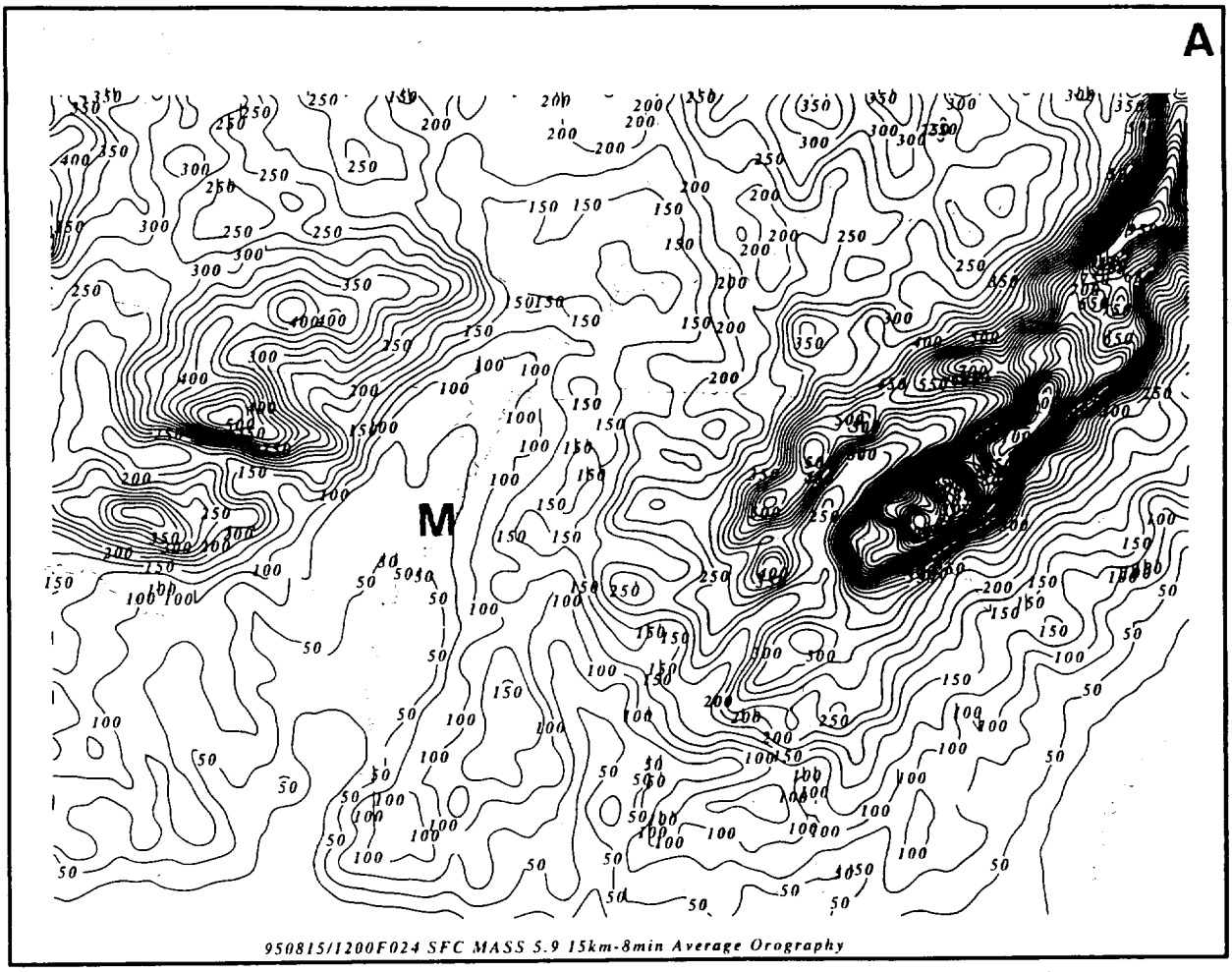
A
M
950815/1200F024 SFC MASS 5.9 15km-8min Average Orography

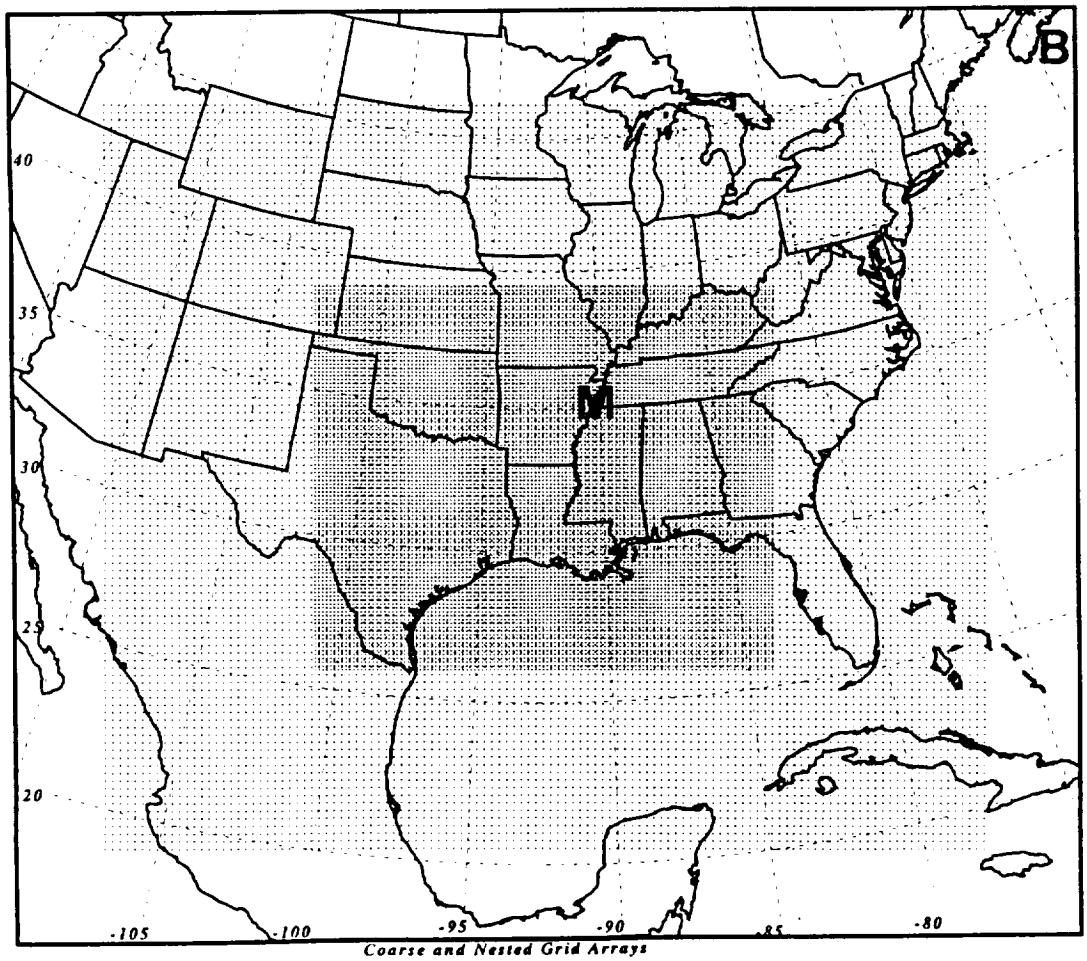
B
M
40
35
30
25
20
-105
-100
-95
-90
-85
-80
Coarse and Nested Grid Arrays

FIG. 1A-B

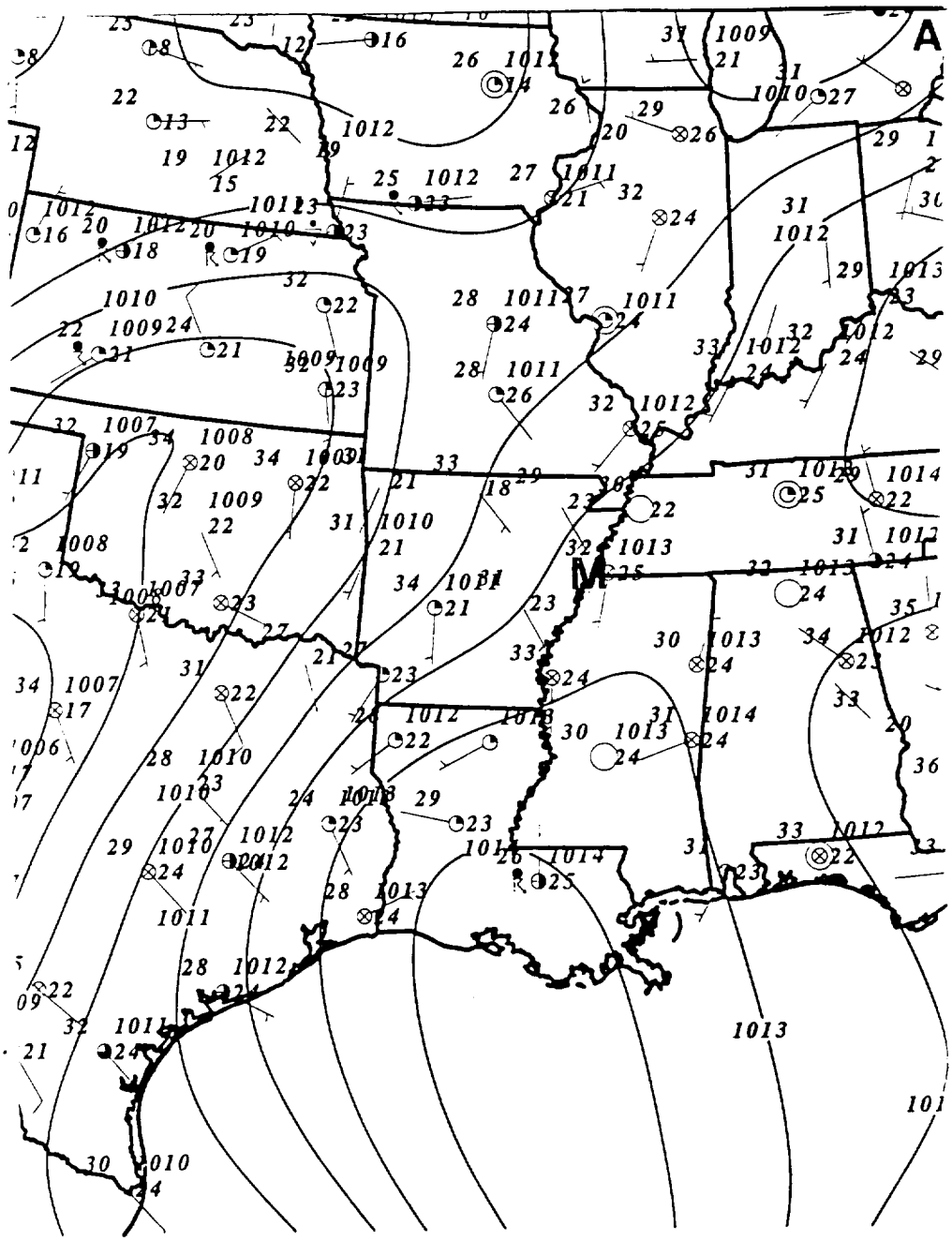

SFC 950815/0000 Observed Surface Data

FIG. 2A

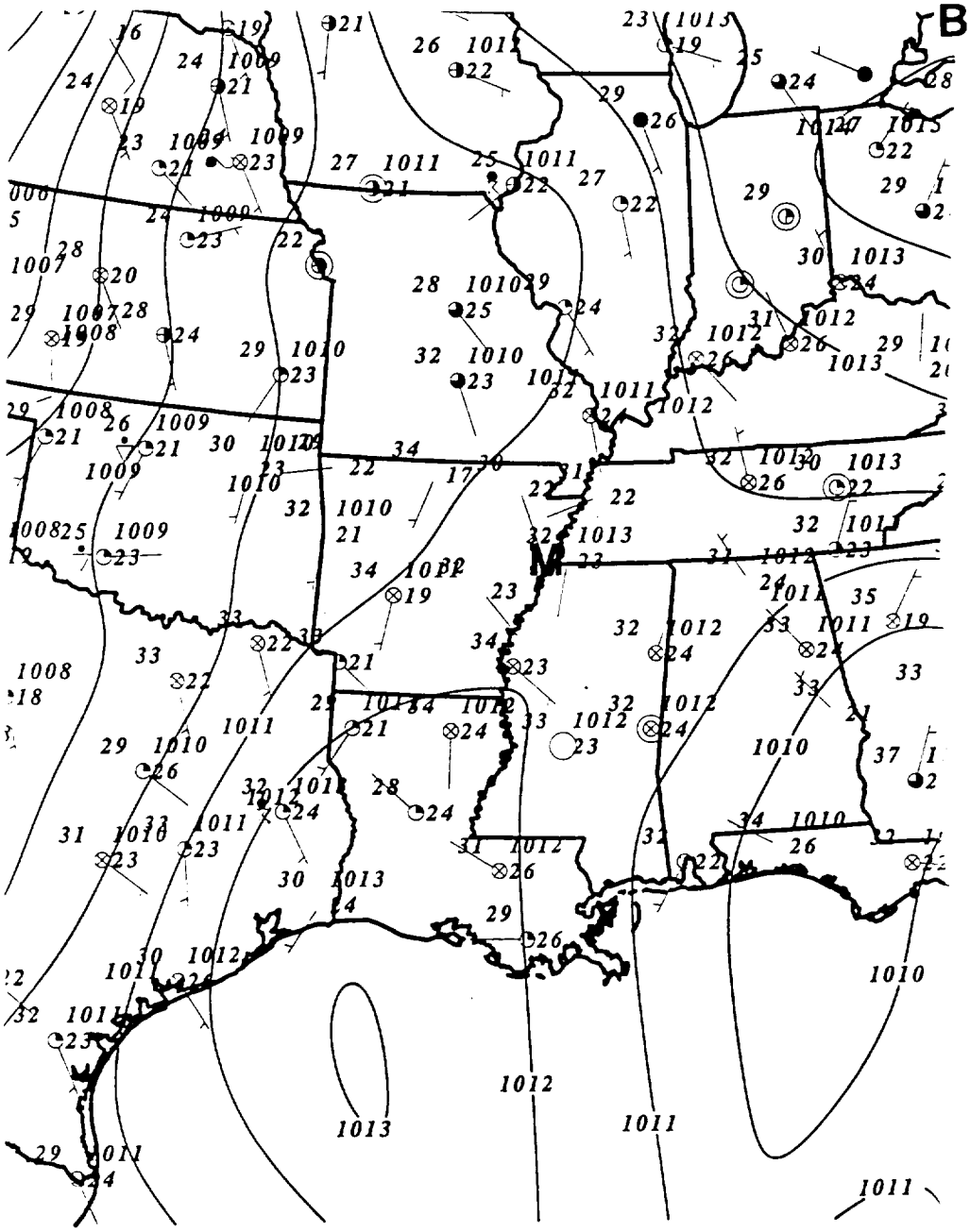

FIG. 2B

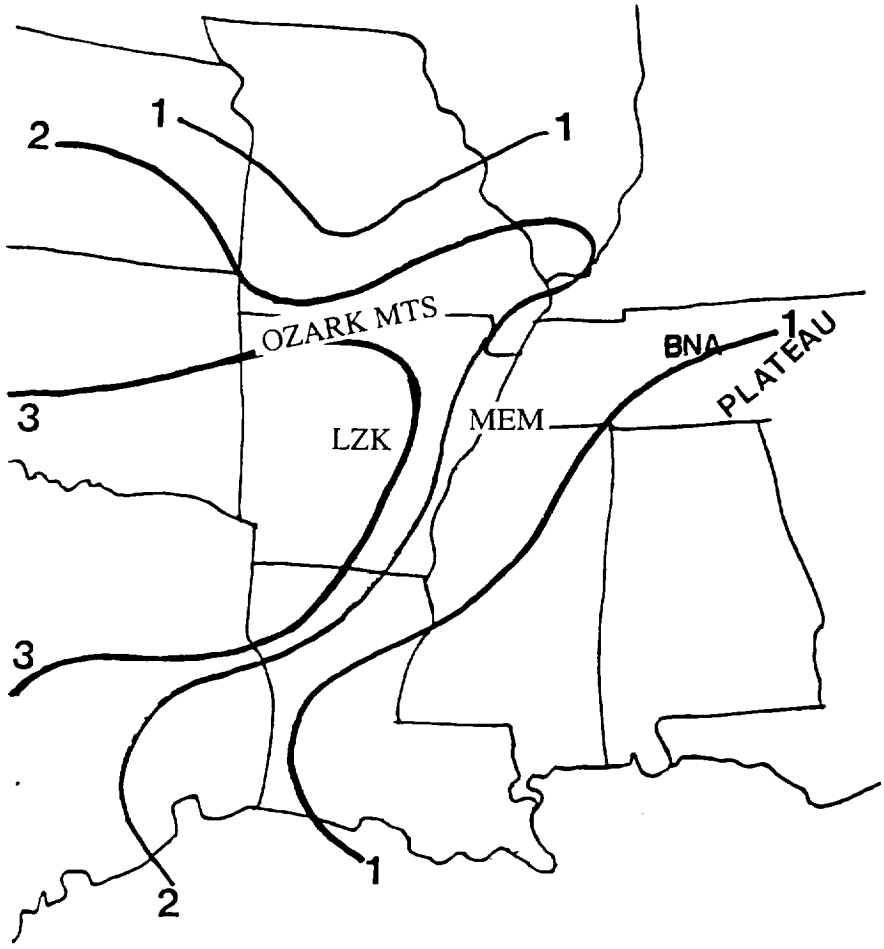
C
1
2
1
1
OZARK MTS
BNA
1
PLATEAU
3
LZK
MEM
3
1
2

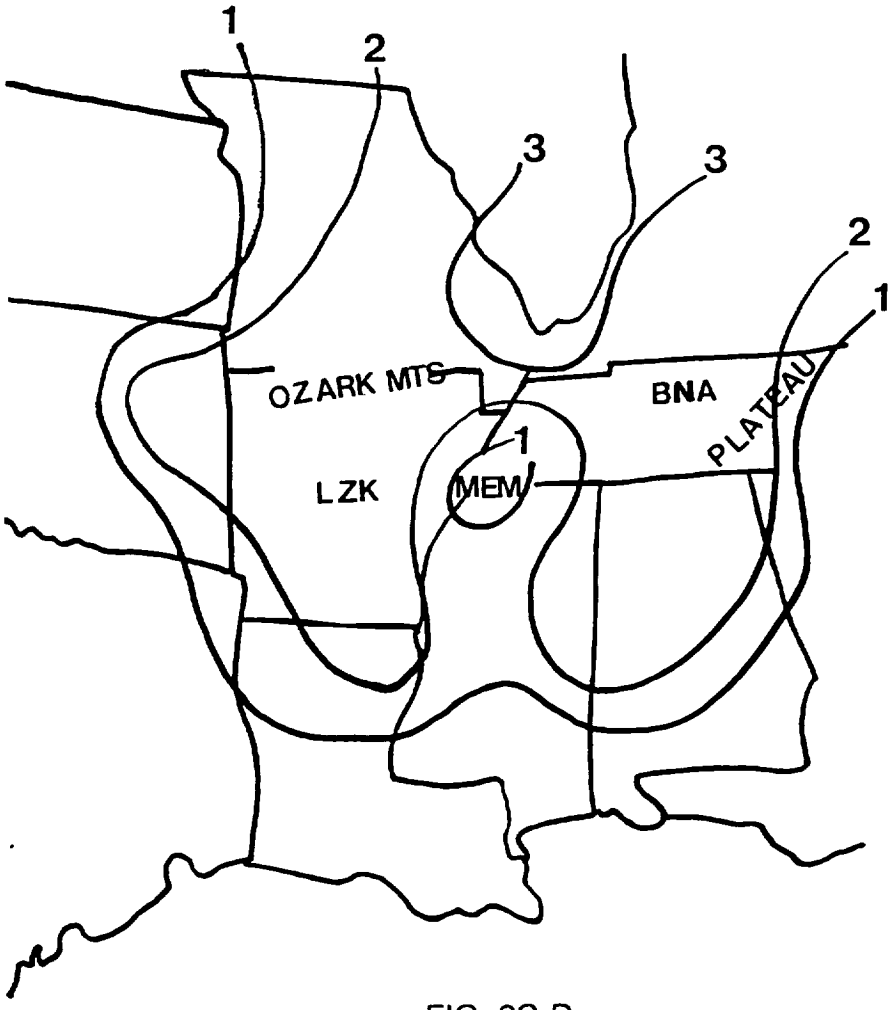
D
1
2
3
3
2
1
OZARK MTS
BNA
PLATEAU
1
LZK
MEM

FIG. 2C-D

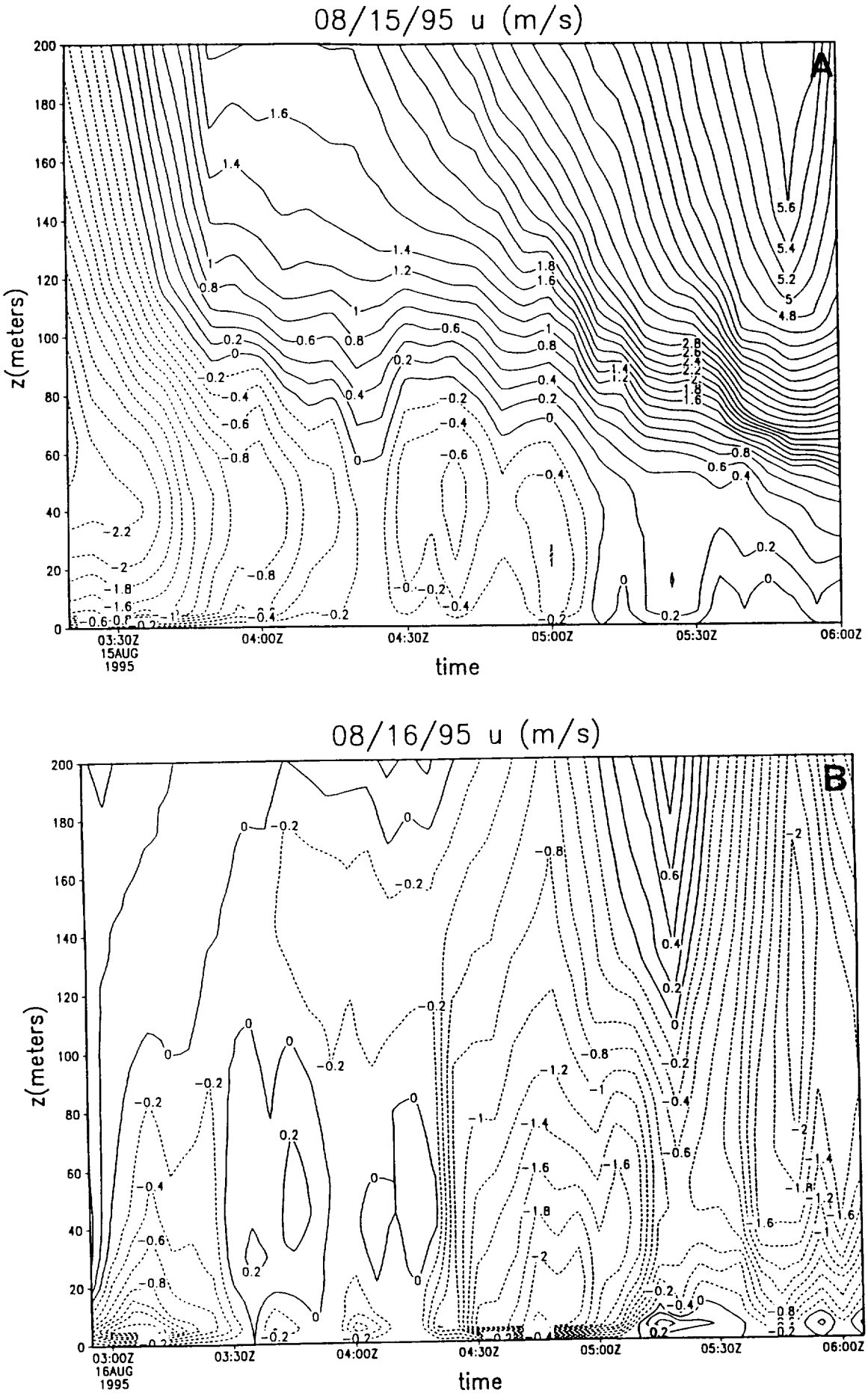
08/15/95 u (m/s)
A
z(meters)
time
03:30Z
15AUG
1995
04:00Z
04:30Z
05:00Z
05:30Z
06:00Z
08/16/95 u (m/s)
B
z(meters)
time
03:00Z
16AUG
1995
03:30Z
04:00Z
04:30Z
05:00Z
05:30Z
06:00Z

FIG. 3A-B

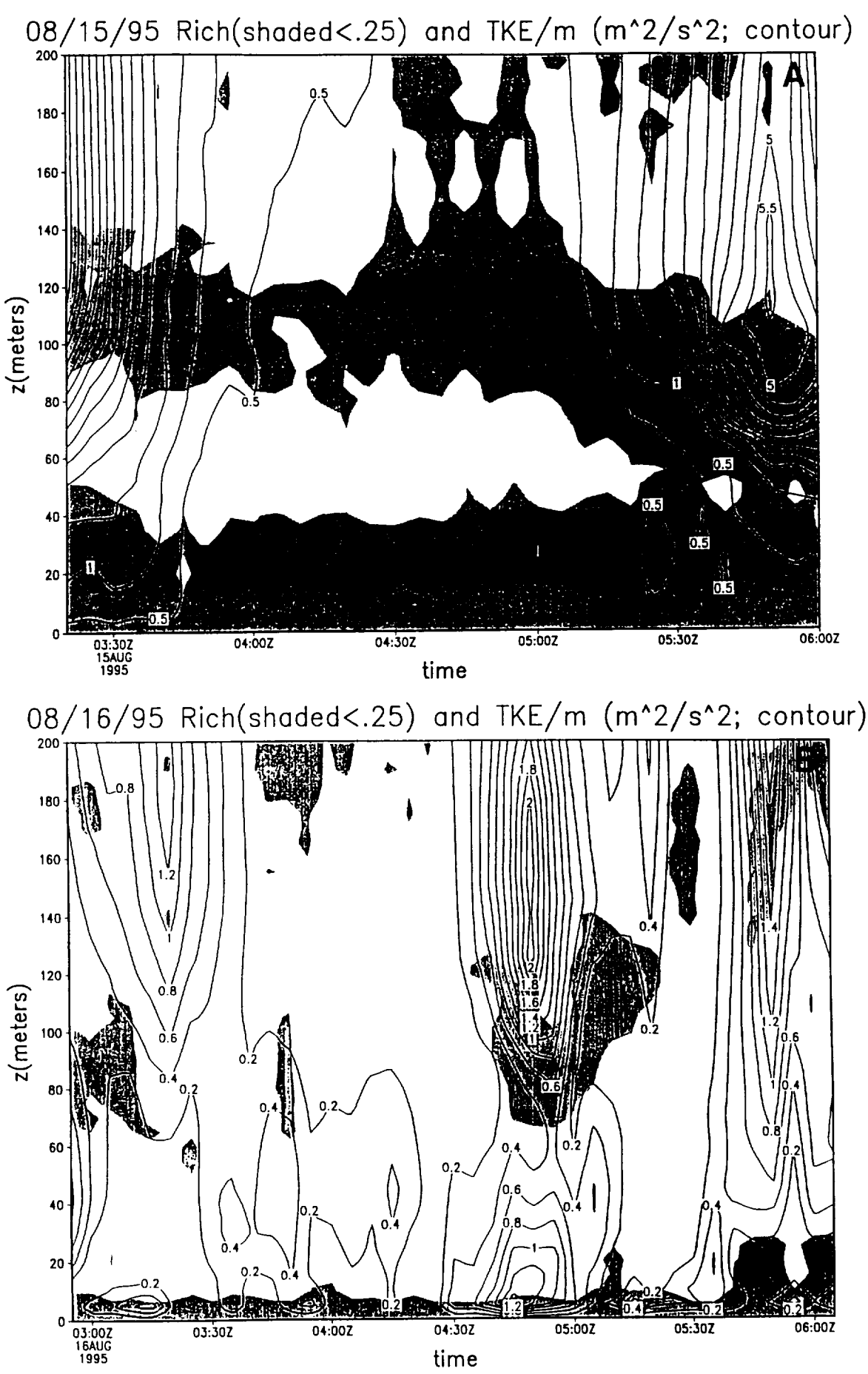
08/15/95 Rich(shaded<.25) and TKE/m (m^2/s^2; contour)
A
z(meters)
time
03:30Z 15AUG 1995
04:00Z
04:30Z
05:00Z
05:30Z
06:00Z
08/16/95 Rich(shaded<.25) and TKE/m (m^2/s^2; contour)
B
z(meters)
time
03:00Z 16AUG 1995
03:30Z
04:00Z
04:30Z
05:00Z
05:30Z
06:00Z

FIG. 4A-B

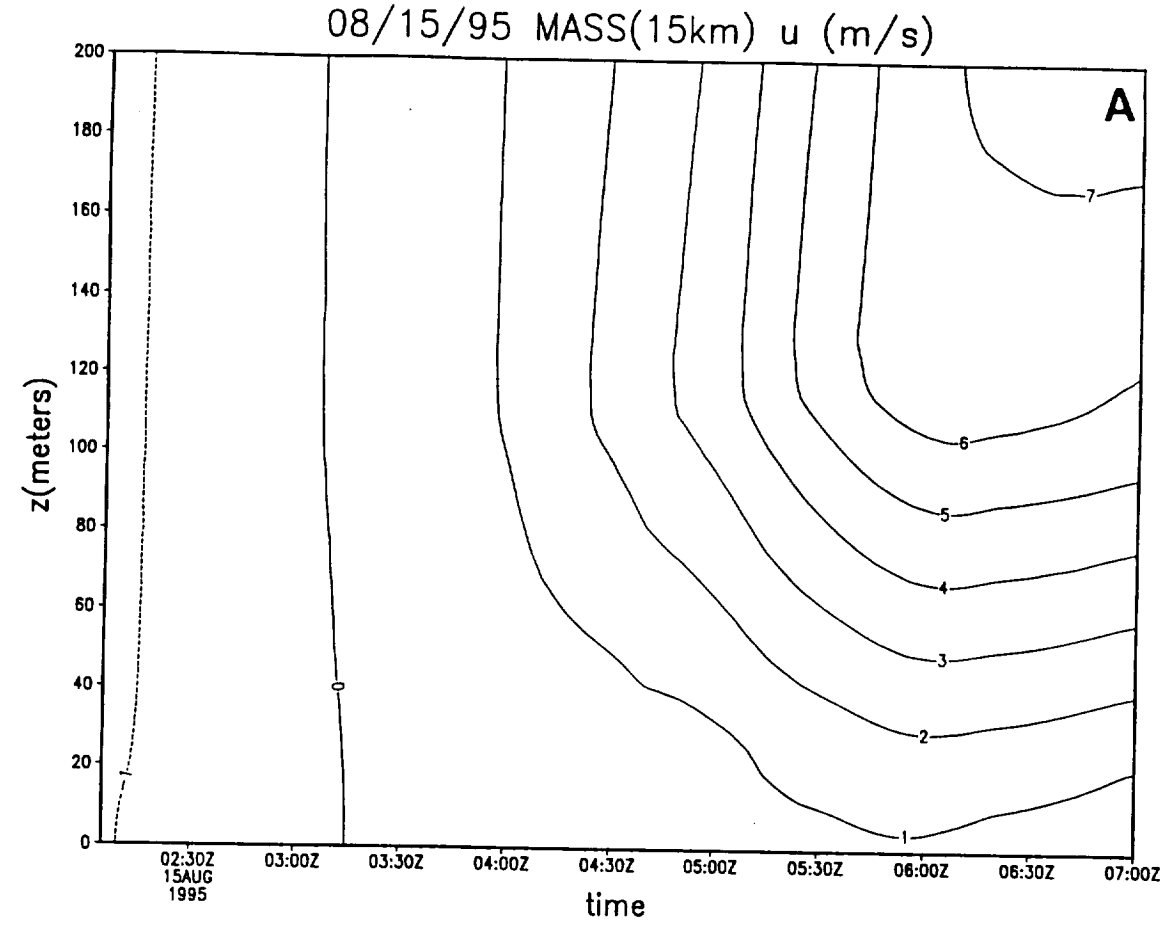
08/15/95 MASS(15km) u (m/s)
A
z(meters)
time
02:30Z 15AUG 1995
03:00Z
03:30Z
04:00Z
04:30Z
05:00Z
05:30Z
06:00Z
06:30Z
07:00Z

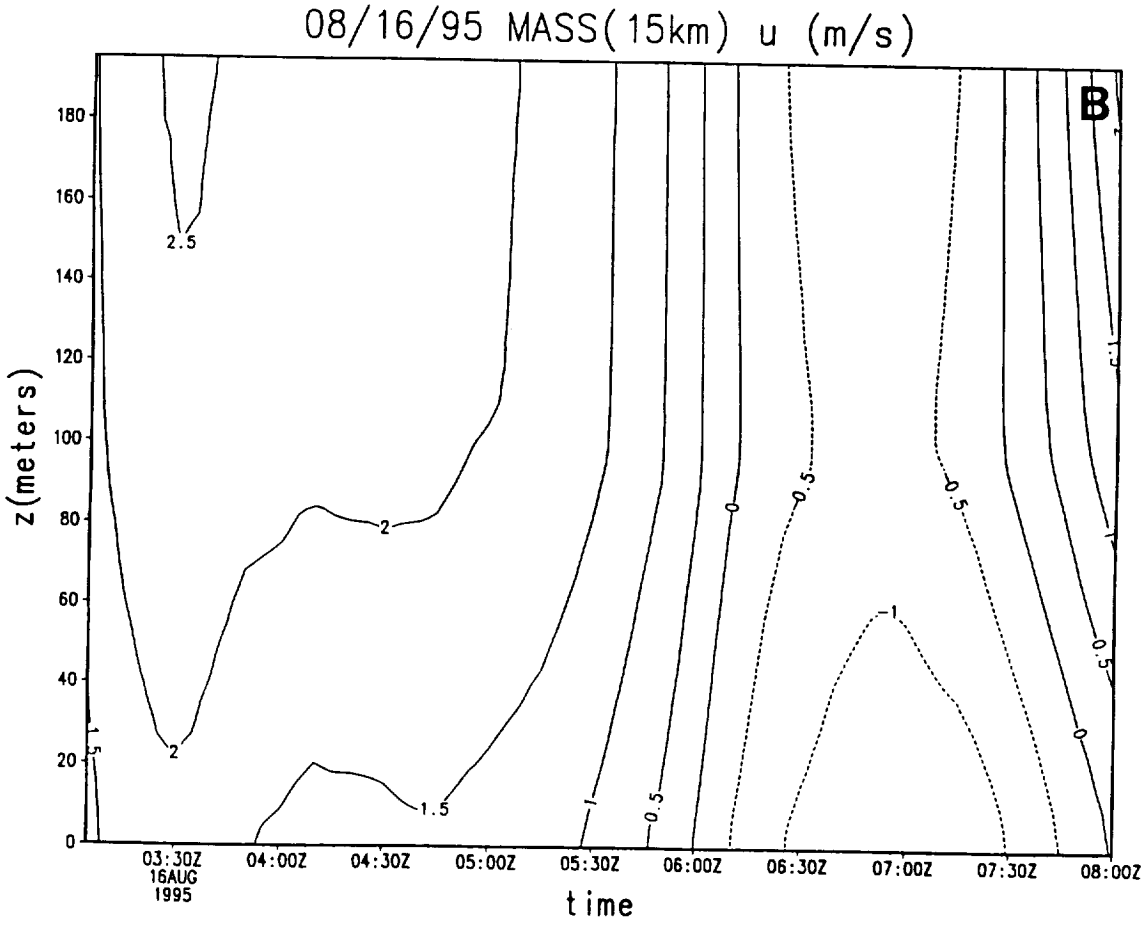
08/16/95 MASS(15km) u (m/s)
B
z(meters)
time
03:30Z 16AUG 1995
04:00Z
04:30Z
05:00Z
05:30Z
06:00Z
06:30Z
07:00Z
07:30Z
08:00Z

FIG. 5A-B

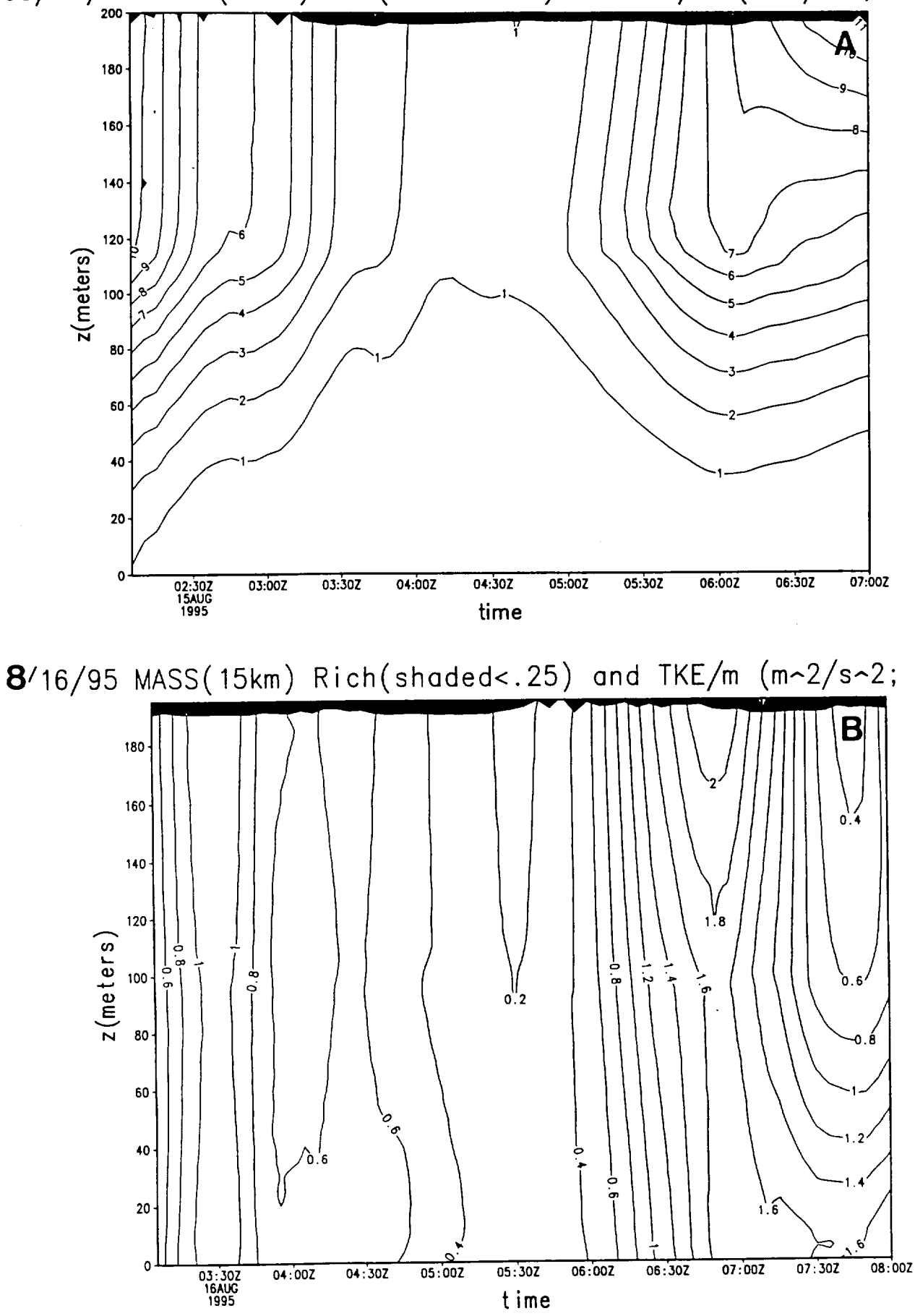
08/15/95 MASS(15km) Rich(shaded<.25) and TKE/m (m^2/s^2;
A
z(meters)
time
02:30Z 15AUG 1995
03:00Z
03:30Z
04:00Z
04:30Z
05:00Z
05:30Z
06:00Z
06:30Z
07:00Z
8/16/95 MASS(15km) Rich(shaded<.25) and TKE/m (m^2/s^2;
B
z(meters)
time
03:30Z 16AUG 1995
04:00Z
04:30Z
05:00Z
05:30Z
06:00Z
06:30Z
07:00Z
07:30Z
08:00Z

FIG. 6A-B

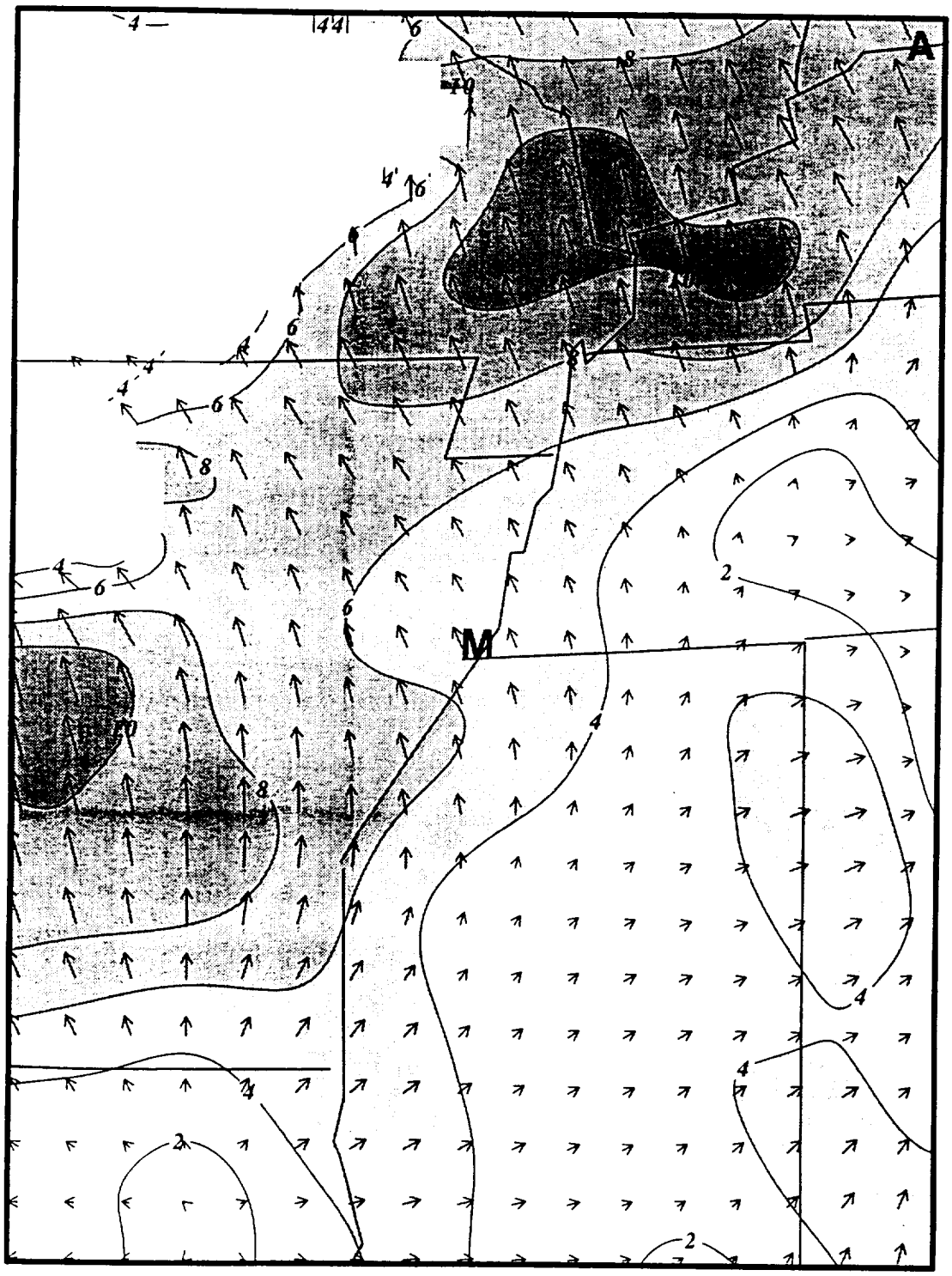

FIG. 7A

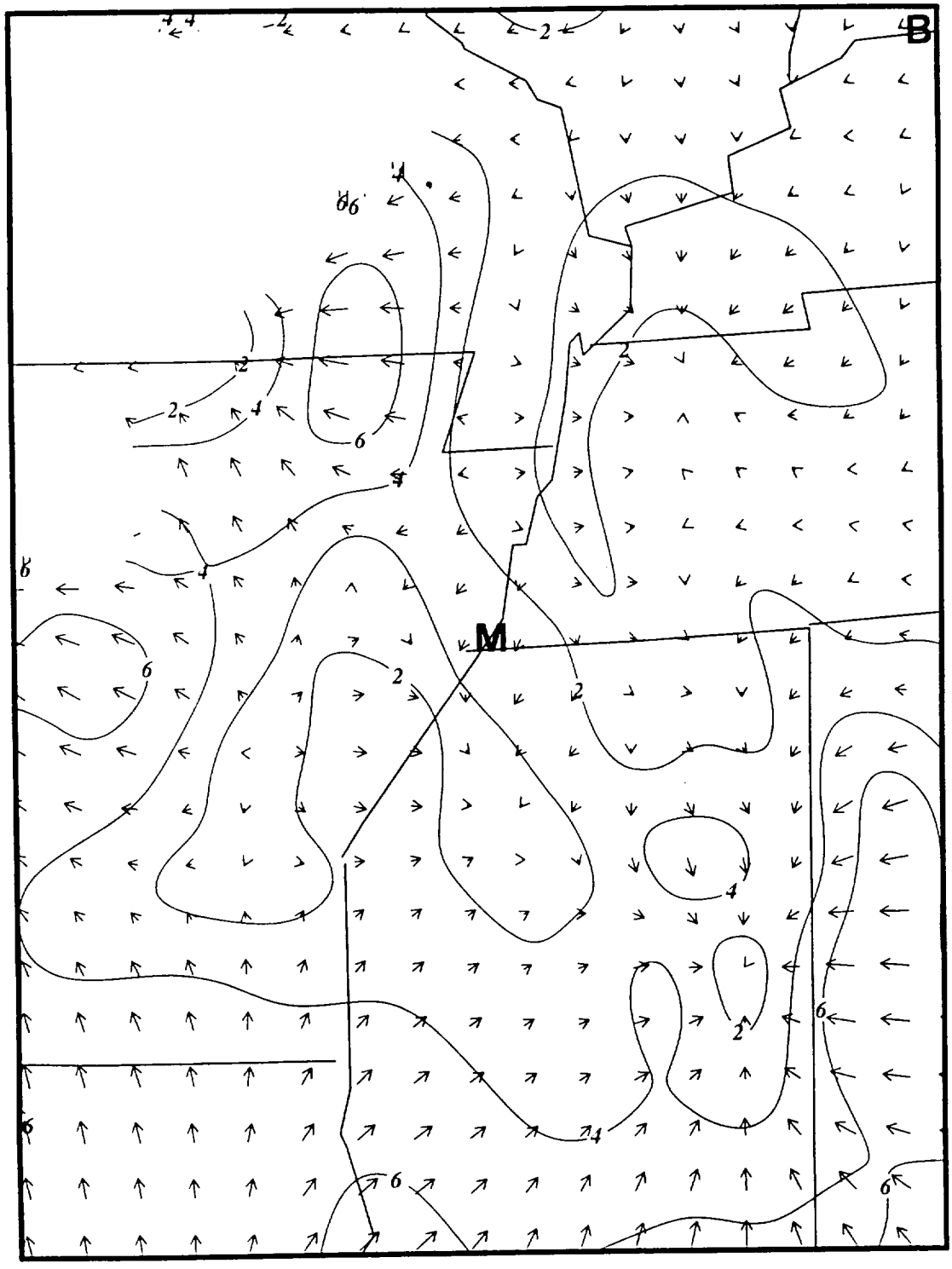

FIG. 7B

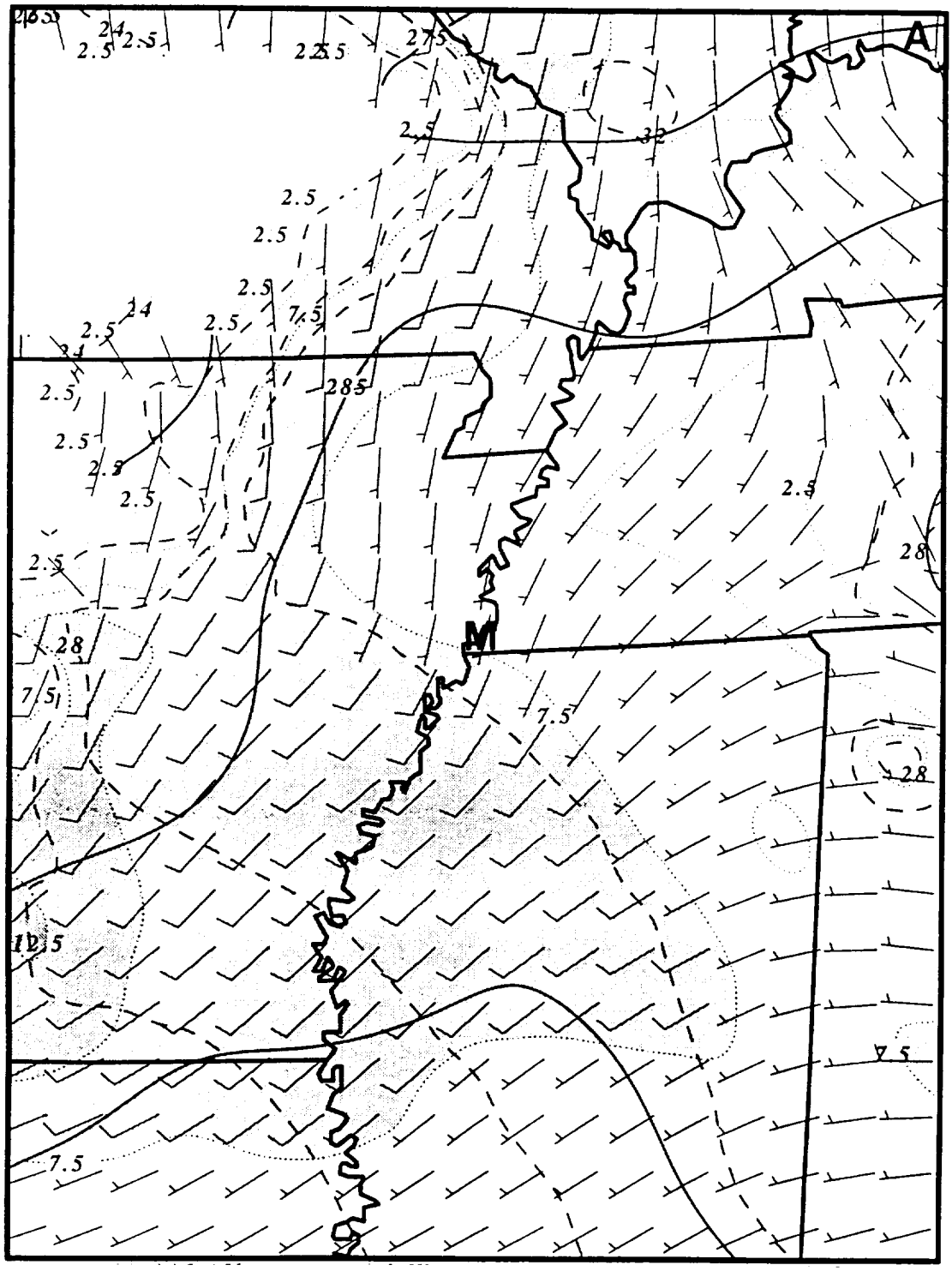

FIG. 8A

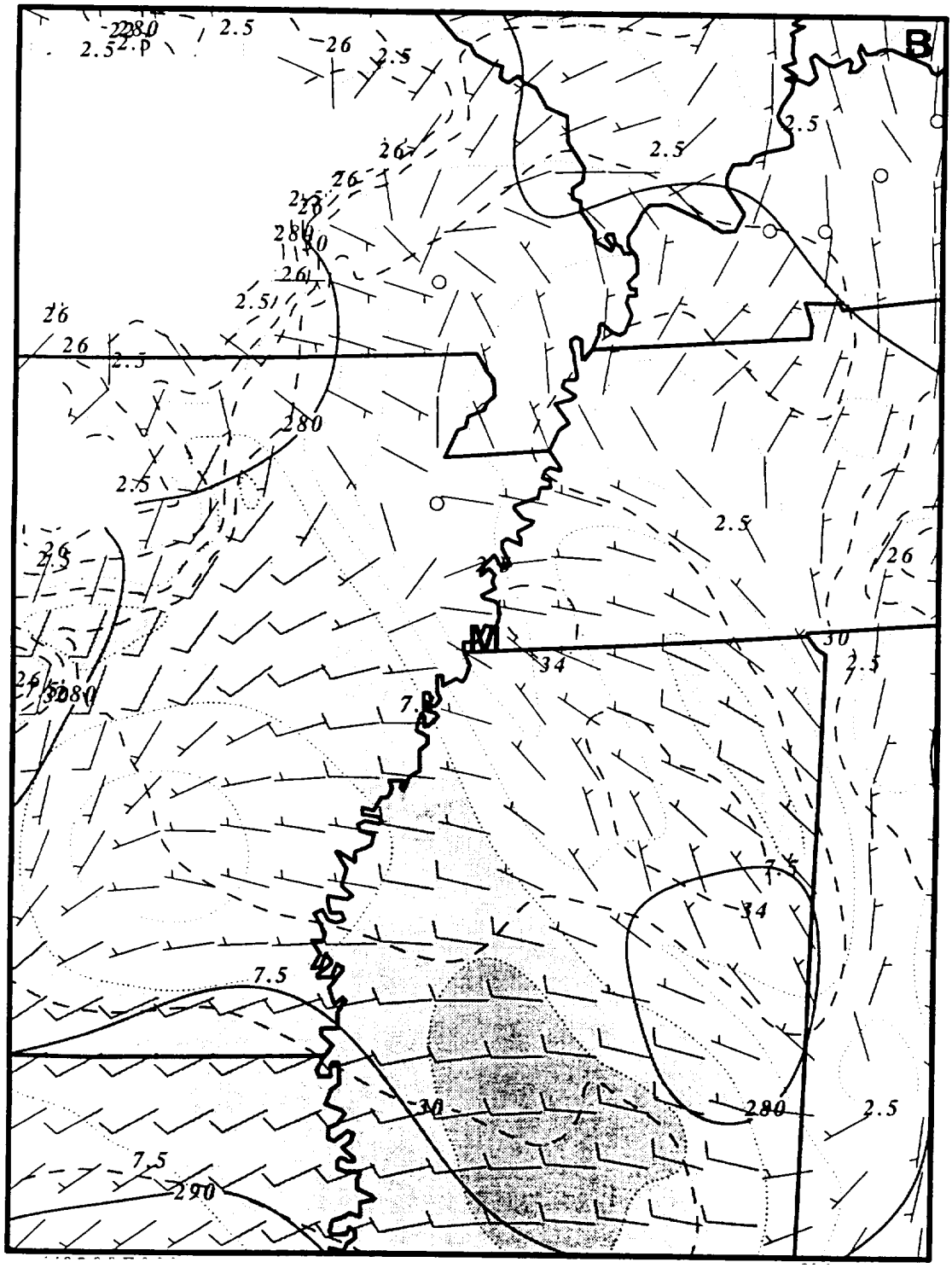

FIG. 8B

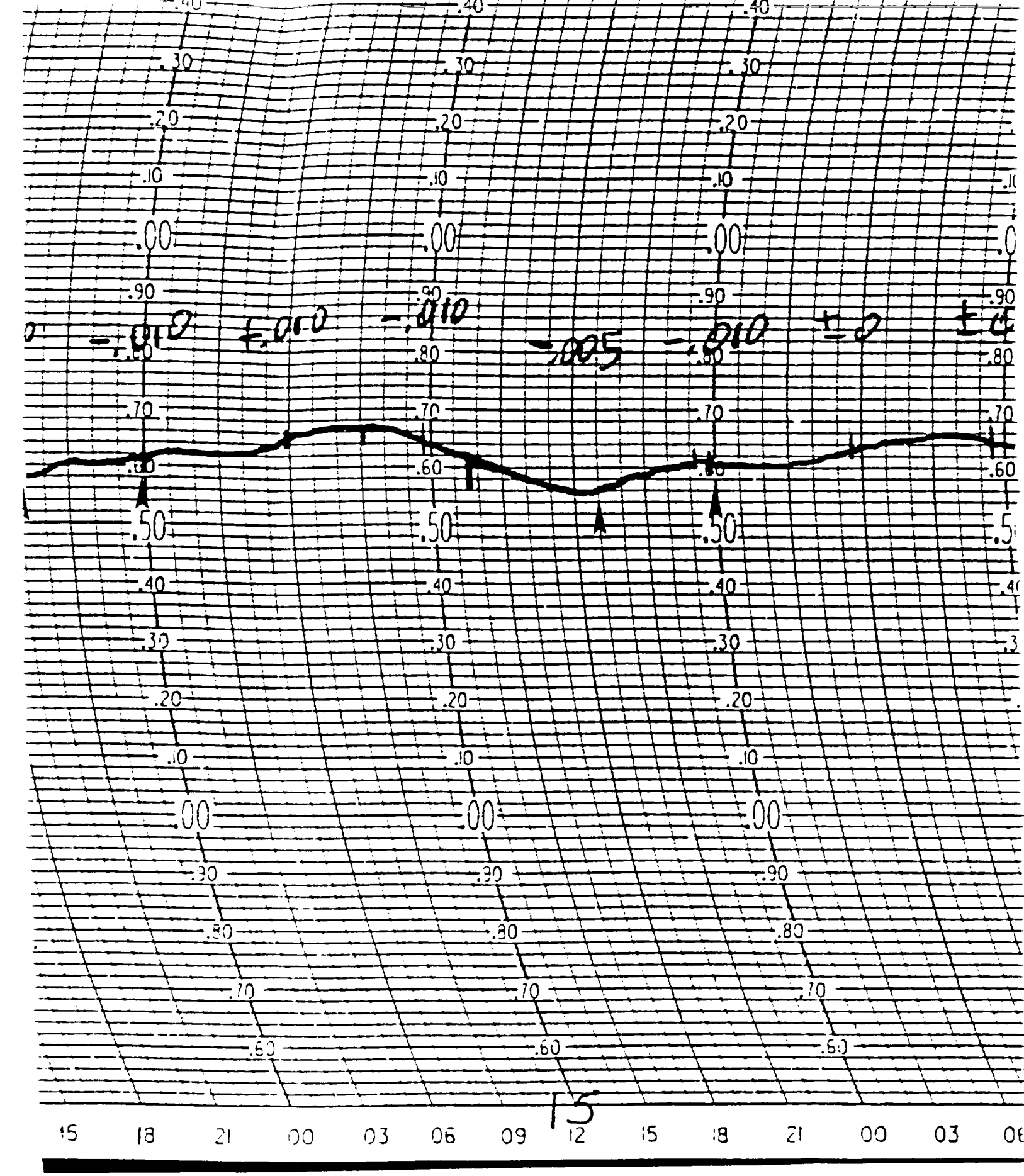
.40
.30
.20
.10
.00
.90
.80
.70
.60
.50
.40
.30
.20
.10
.00
.90
.80
.70
.60
.50
.40
.30
.20
.10
.00
.90
.80
.70
.60
15
15
18
21
00
03
06
09
12
15
18
21
00
03
06

FIG. 9

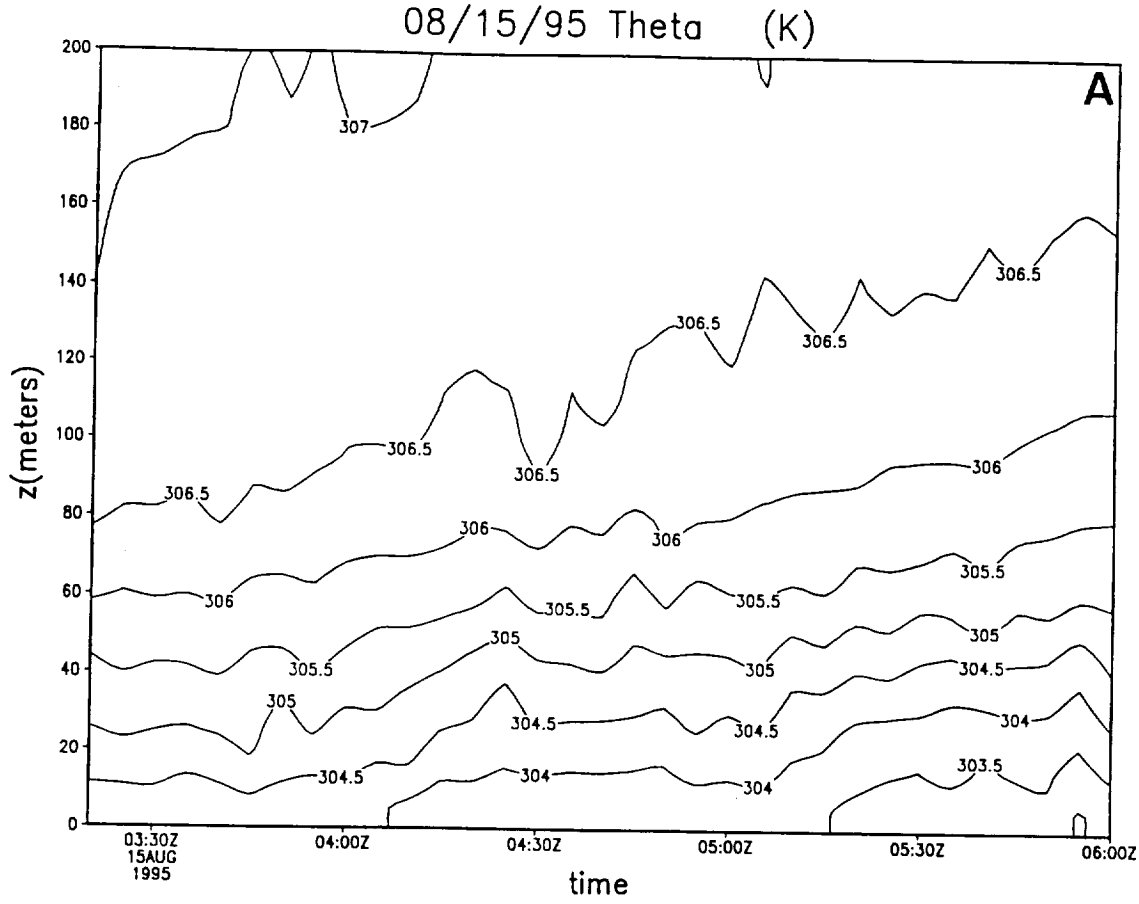
08/15/95 Theta (K)
A
z(meters)
time
03:30Z 15AUG 1995
04:00Z
04:30Z
05:00Z
05:30Z
06:00Z
307
306.5
306
305.5
305
304.5
304
303.5

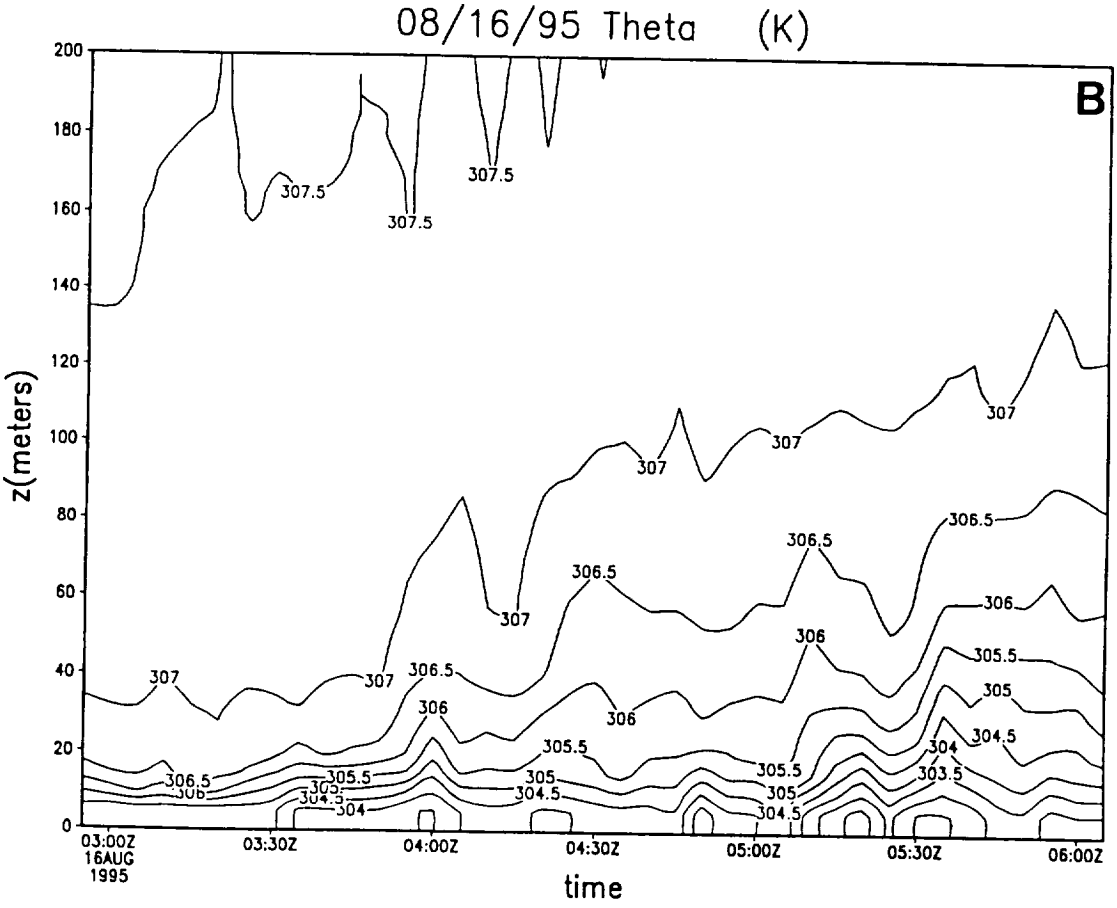
08/16/95 Theta (K)
B
z(meters)
time
03:00Z 16AUG 1995
03:30Z
04:00Z
04:30Z
05:00Z
05:30Z
06:00Z
307.5
307
306.5
306
305.5
305
304.5
304
303.5

FIG. 10A-B

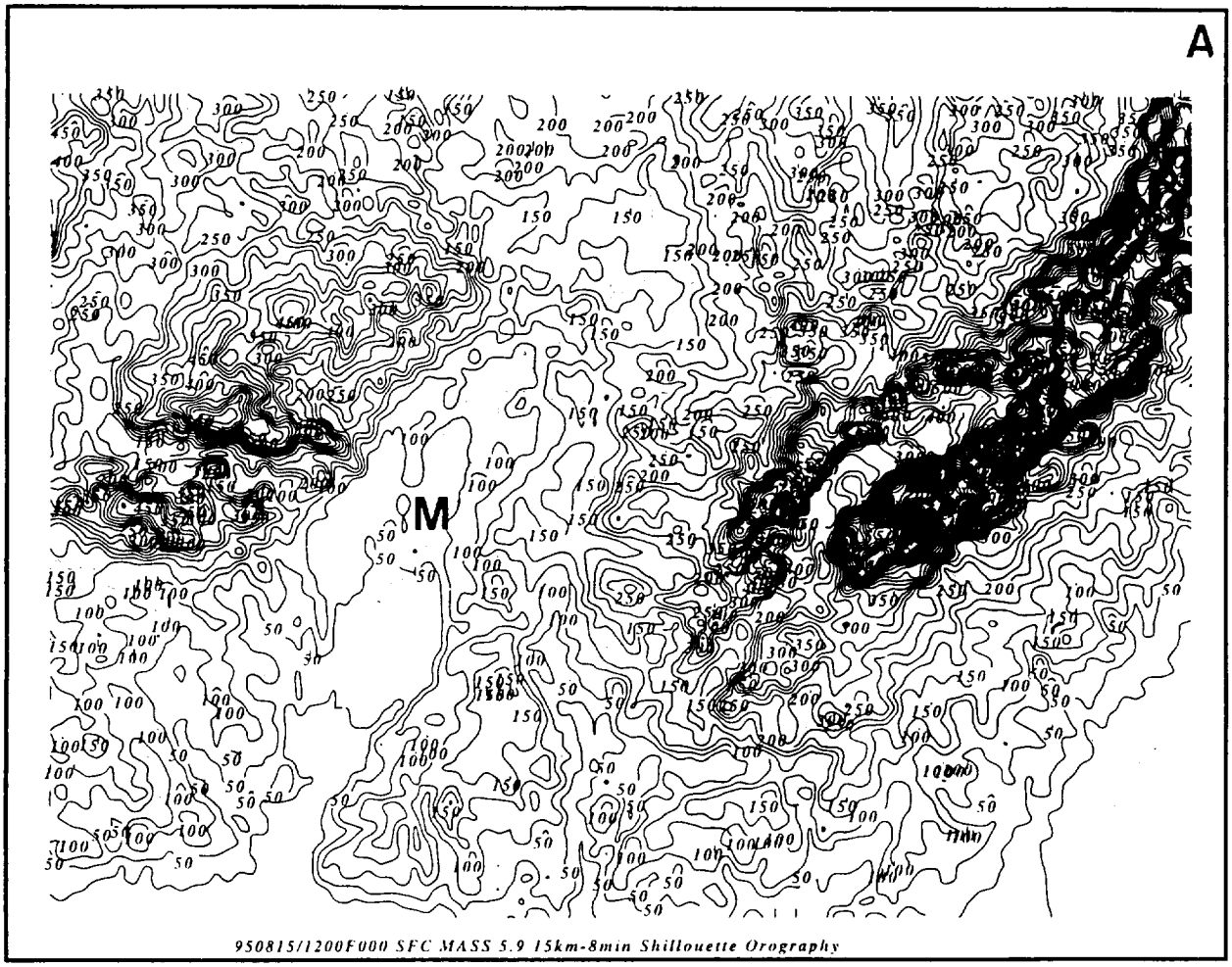
A
M
950815/1200F000 SFC MASS 5.9 15km-8min Shillouette Orography

FIG. 11A

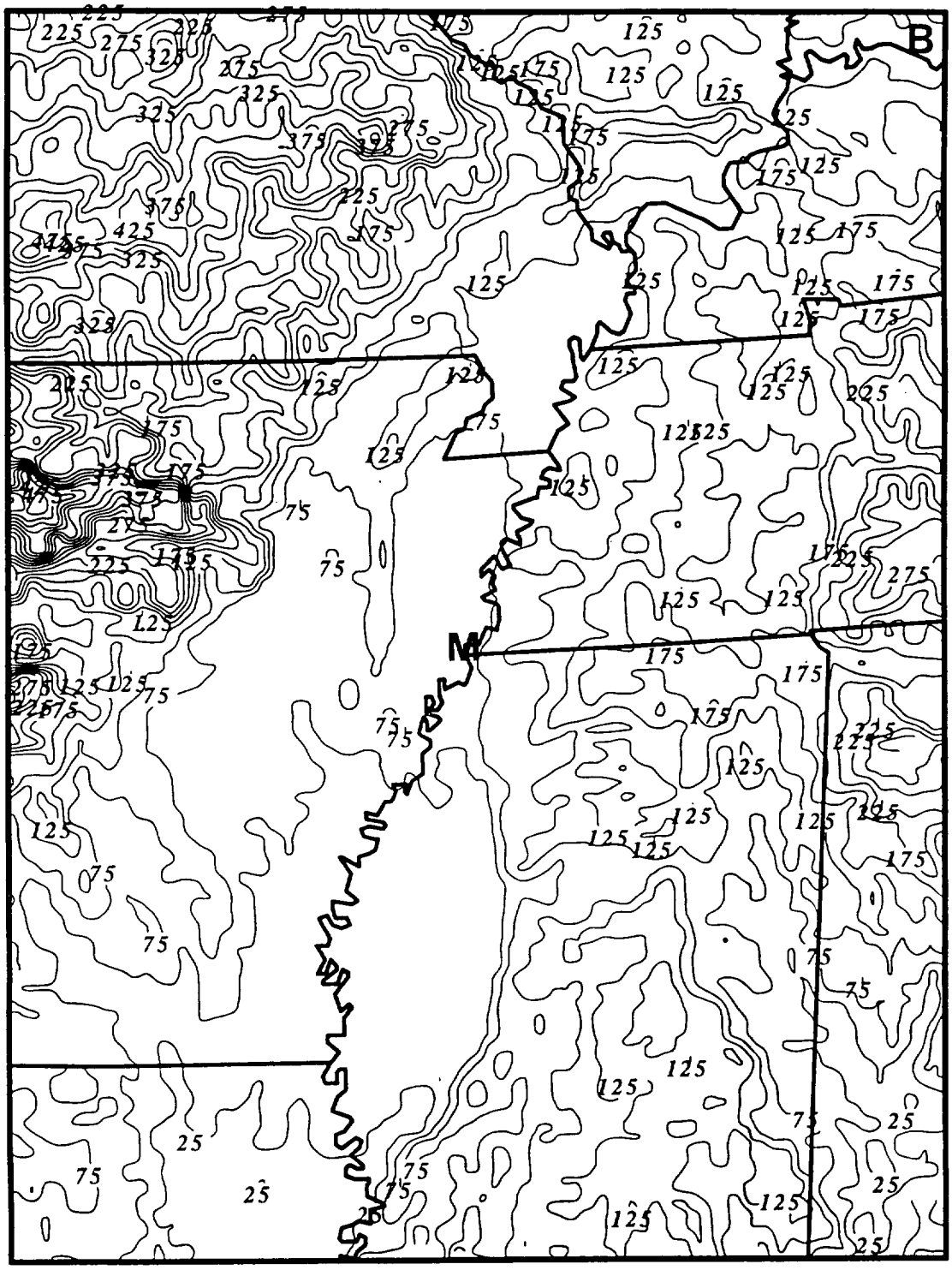

FIG. 11B

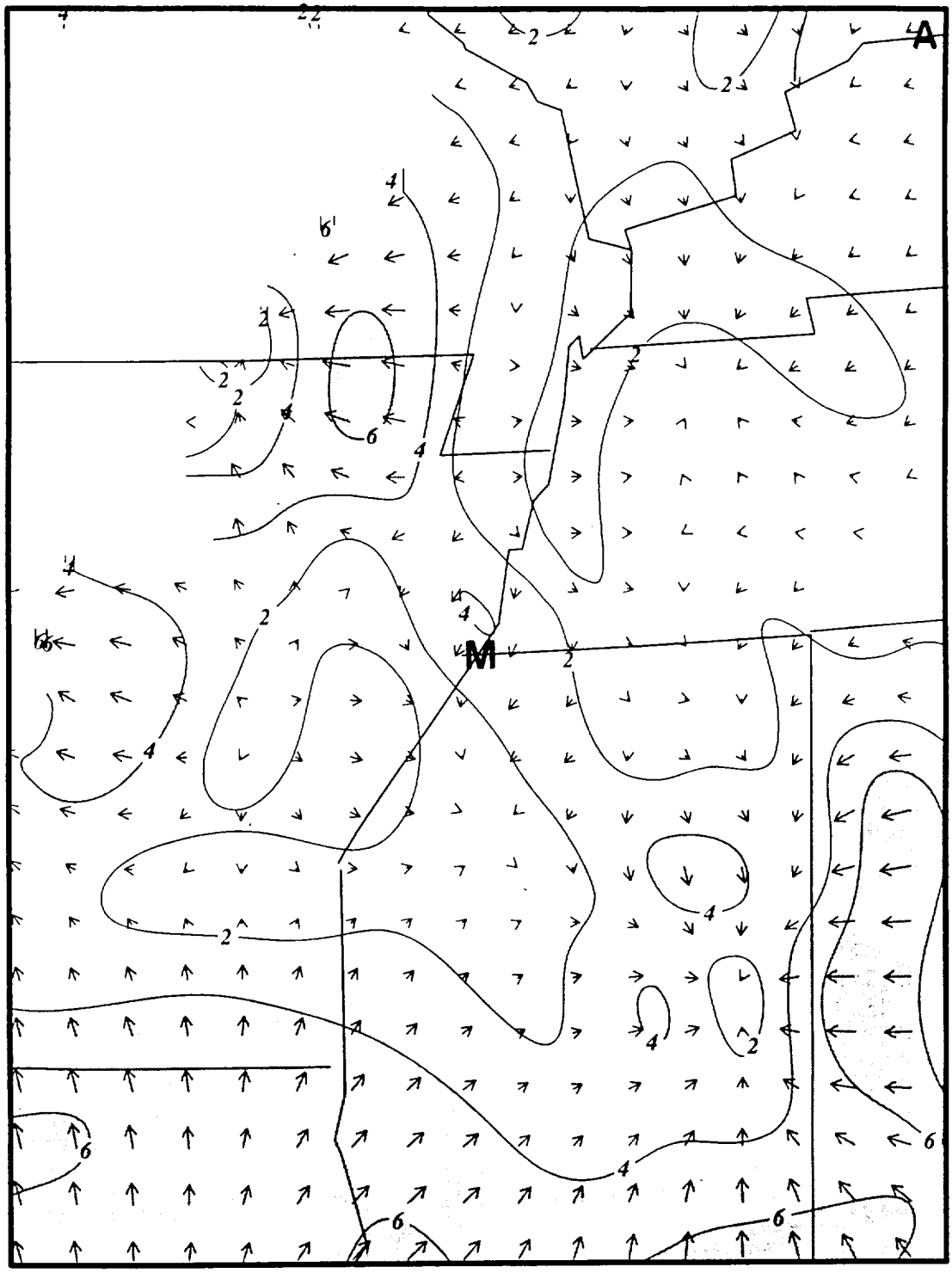

FIG. 12A

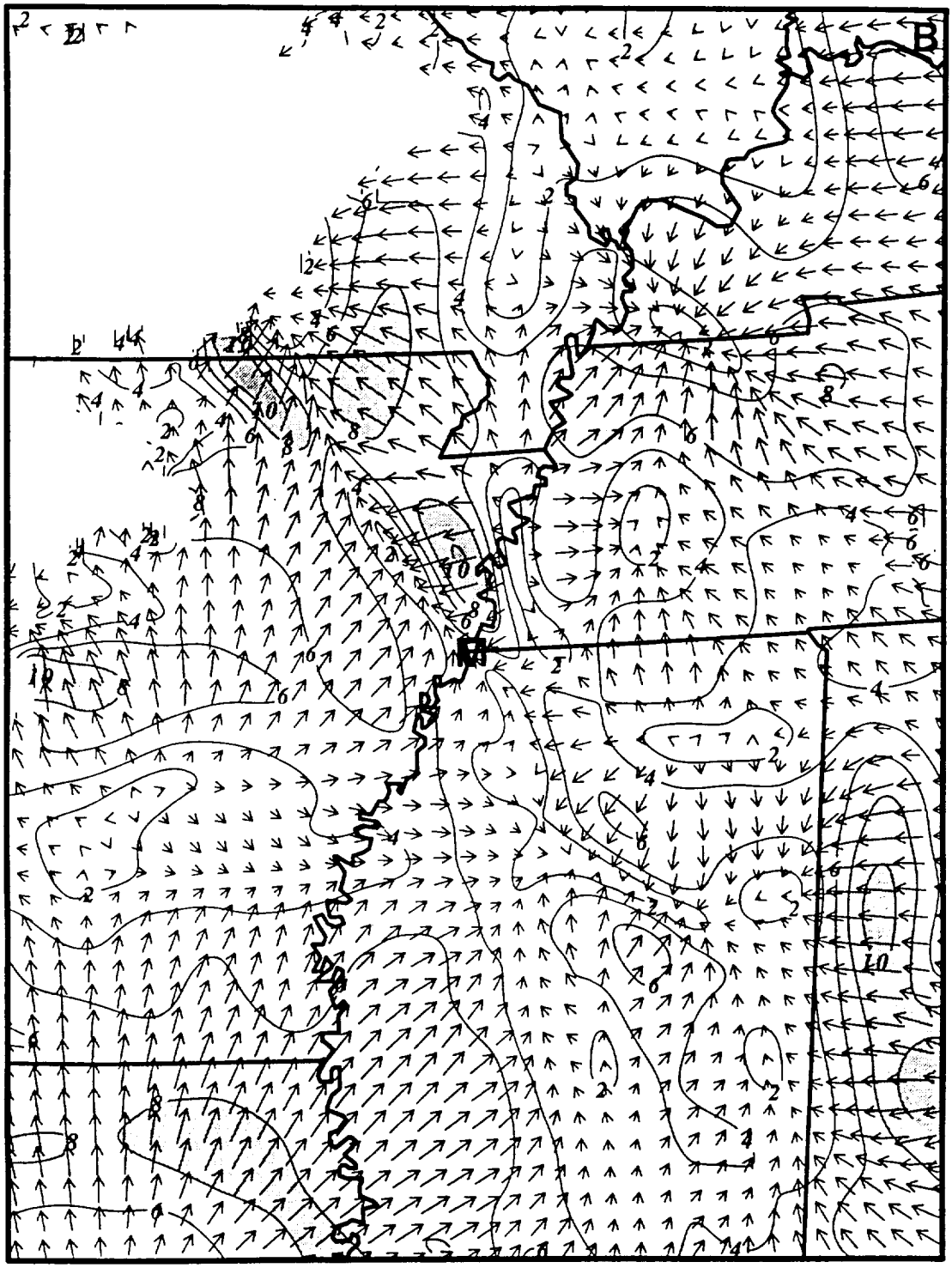

FIG. 12B

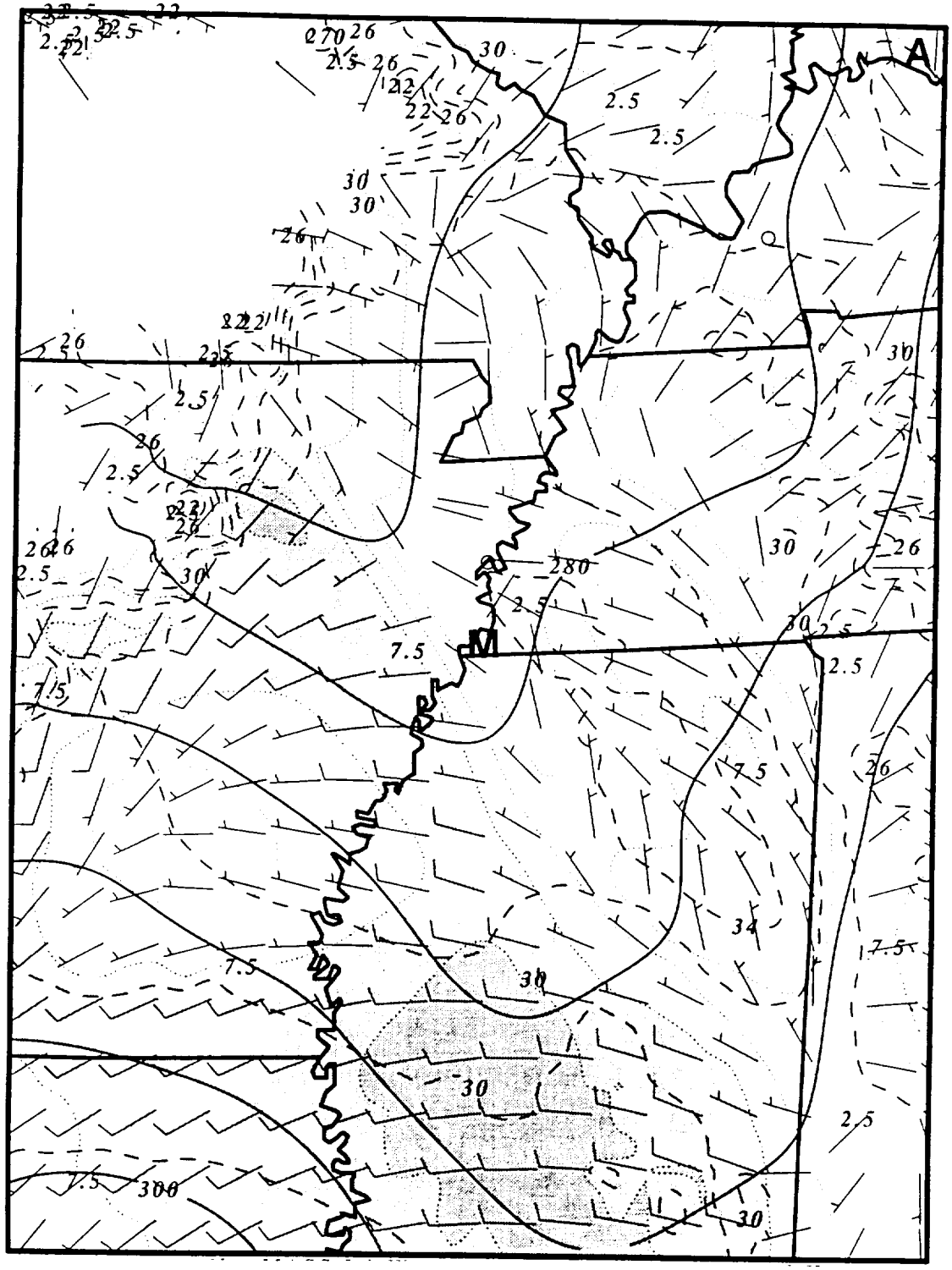

FIG. 13A

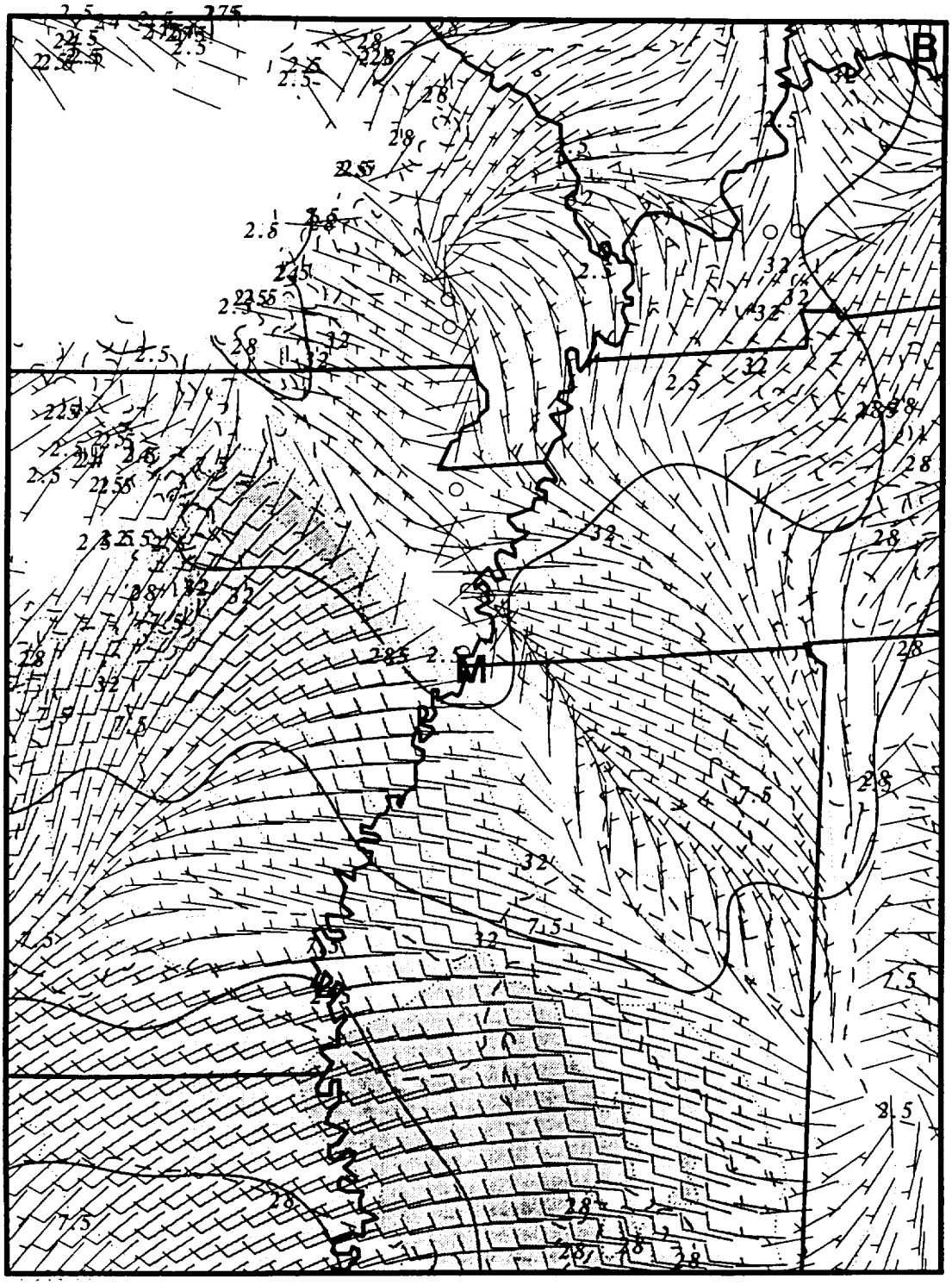

FIG. 13B

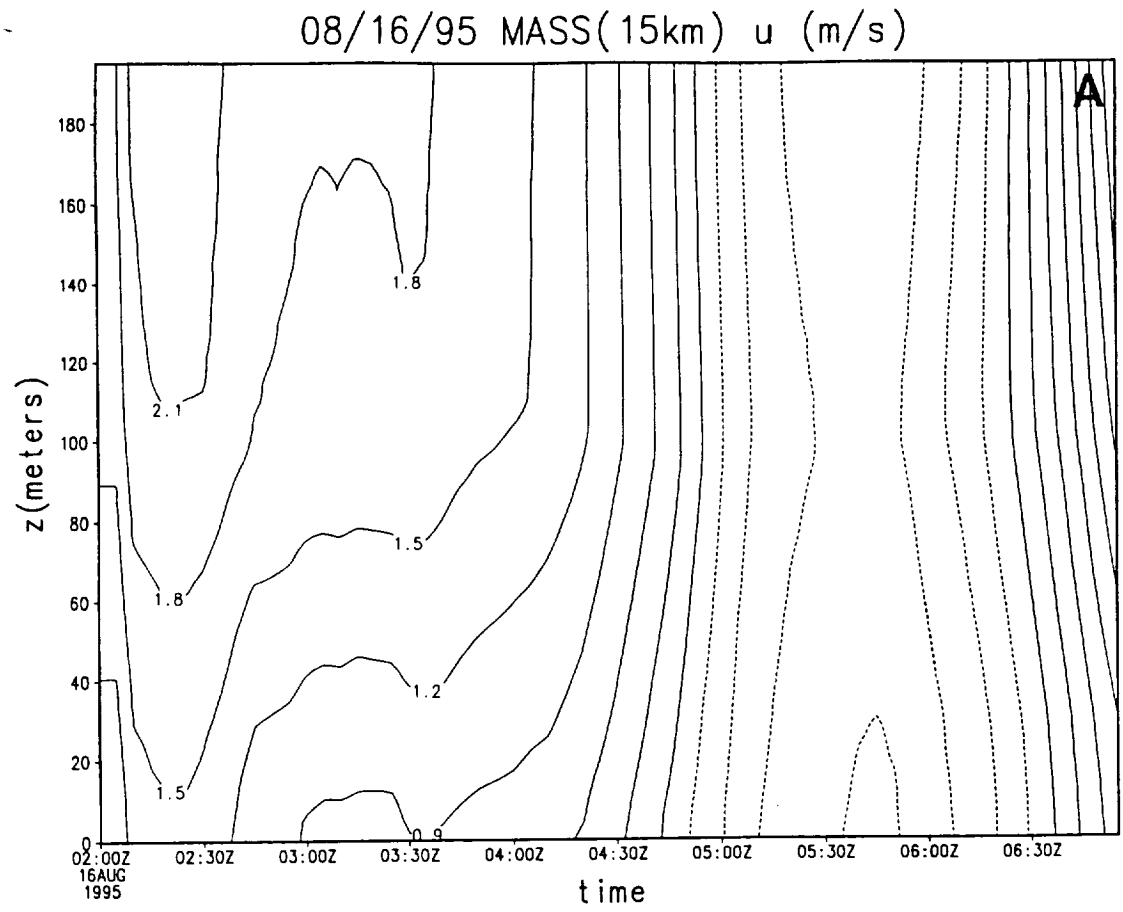
08/16/95 MASS(15km) u (m/s)
A
z(meters)
time
02:00Z 16AUG 1995
02:30Z
03:00Z
03:30Z
04:00Z
04:30Z
05:00Z
05:30Z
06:00Z
06:30Z
2.1
1.8
1.5
1.2
0.9

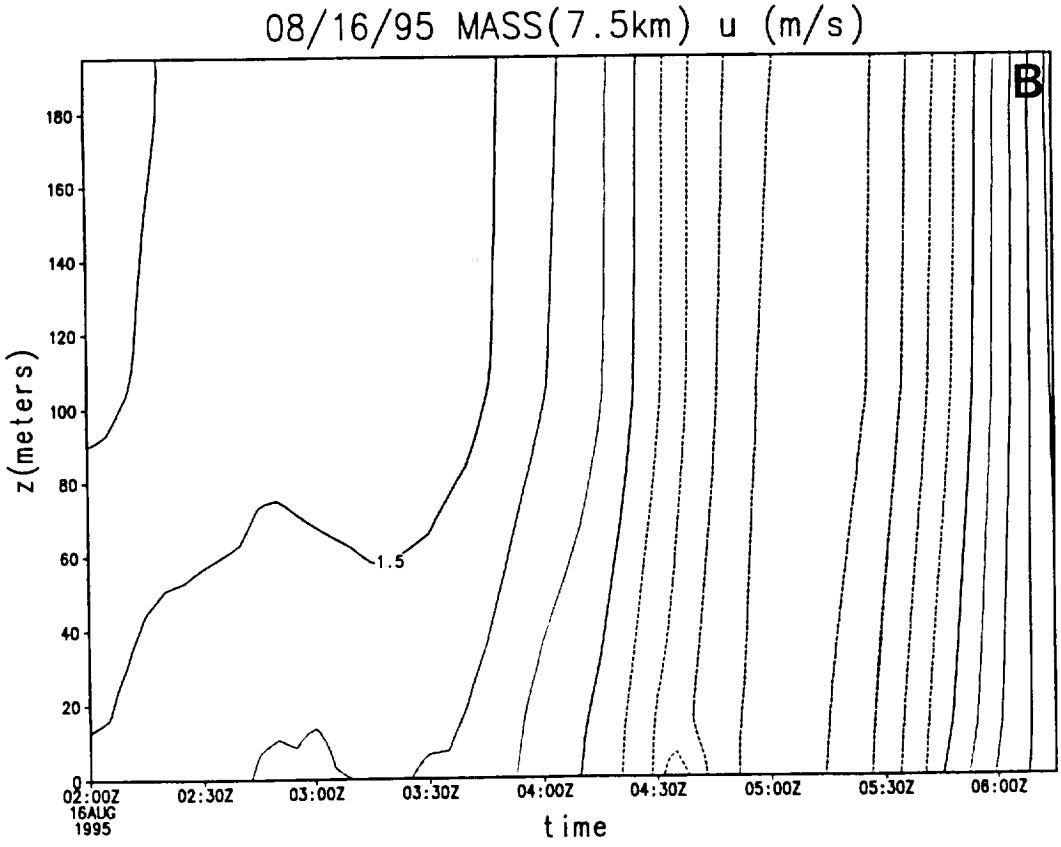
08/16/95 MASS(7.5km) u (m/s)
B
z(meters)
time
02:00Z 16AUG 1995
02:30Z
03:00Z
03:30Z
04:00Z
04:30Z
05:00Z
05:30Z
06:00Z
1.5

FIG. 14A-B

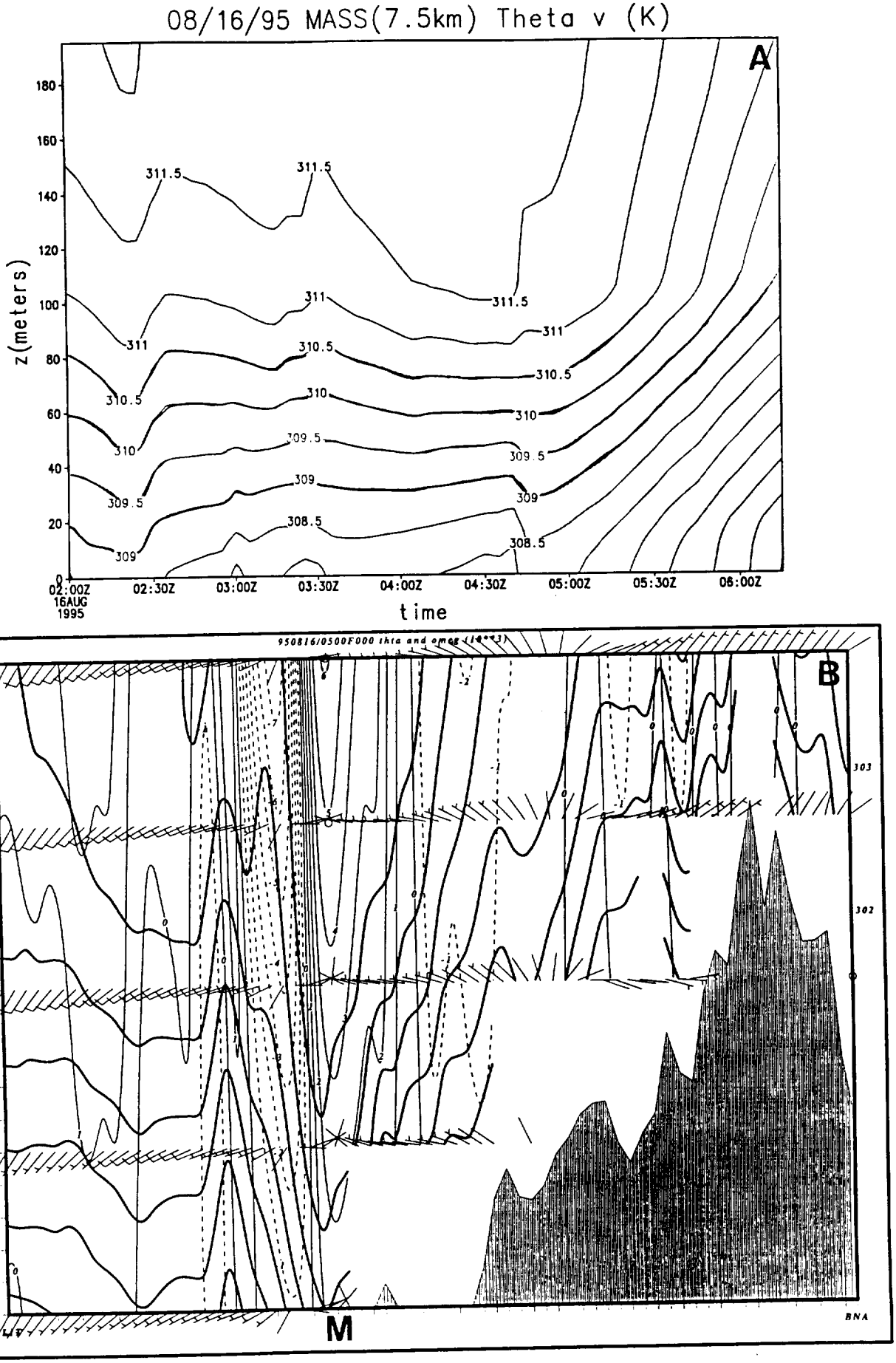
08/16/95 MASS(7.5km) Theta v (K)
A
z(meters)
time
02:00Z 16AUG 1995
02:30Z
03:00Z
03:30Z
04:00Z
04:30Z
05:00Z
05:30Z
06:00Z
311.5
311
310.5
310
309.5
309
308.5
B
M
BNA

FIG. 15A-B

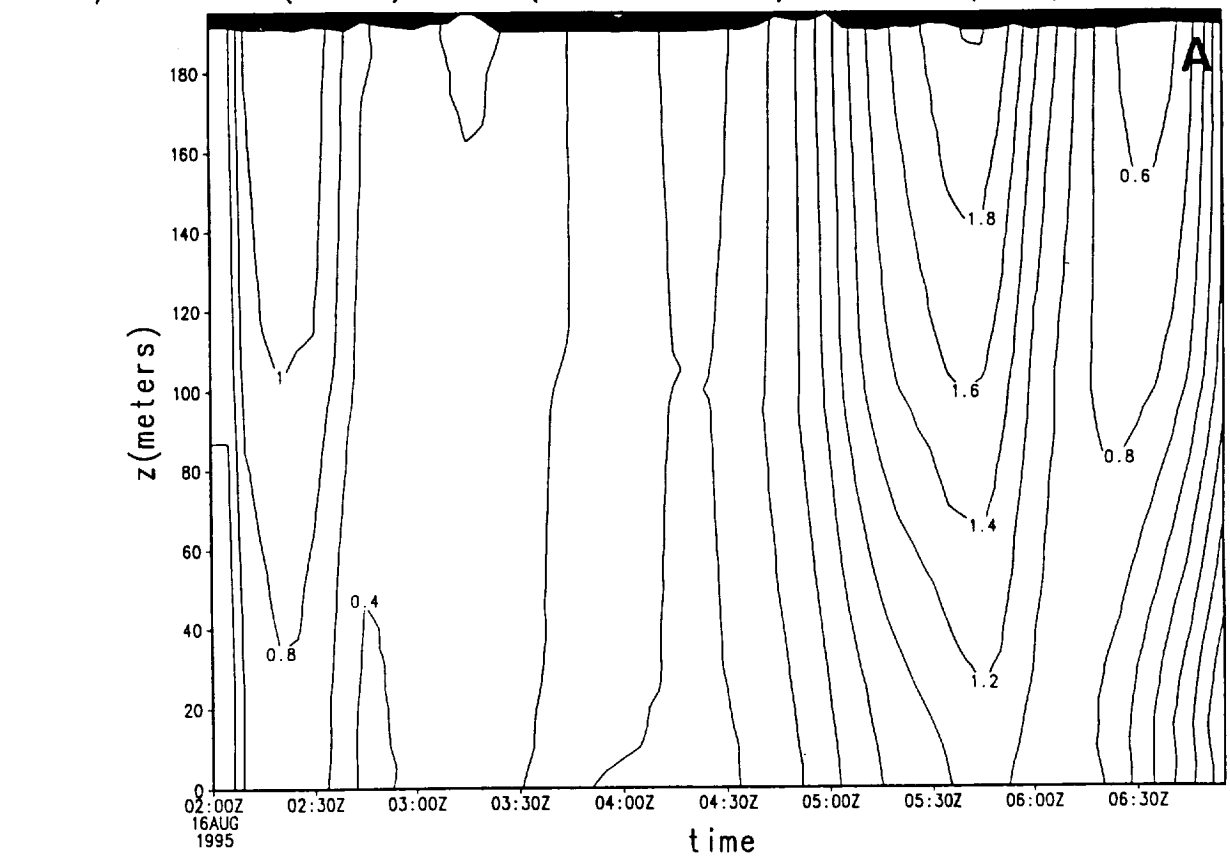
8/16/95 MASS(15km) Rich(shaded<.25) and TKE/m (m^2/s^2;
A
z(meters)
time
02:00Z 16AUG 1995
02:30Z
03:00Z
03:30Z
04:00Z
04:30Z
05:00Z
05:30Z
06:00Z
06:30Z
0.6
1.8
1.6
0.8
1.4
1.2
1
0.4
0.8

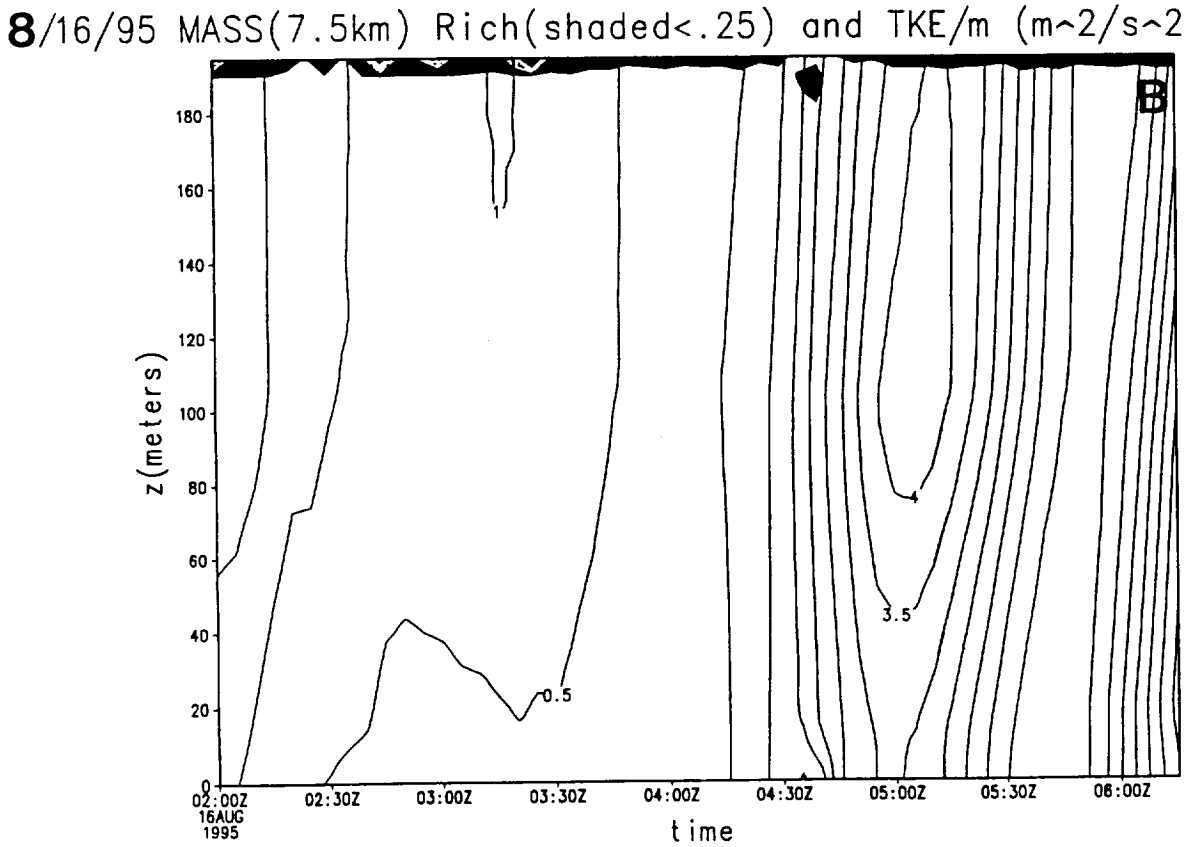
8/16/95 MASS(7.5km) Rich(shaded<.25) and TKE/m (m^2/s^2;
B
z(meters)
time
02:00Z 16AUG 1995
02:30Z
03:00Z
03:30Z
04:00Z
04:30Z
05:00Z
05:30Z
06:00Z
1
4
3.5
0.5

FIG. 16A-B

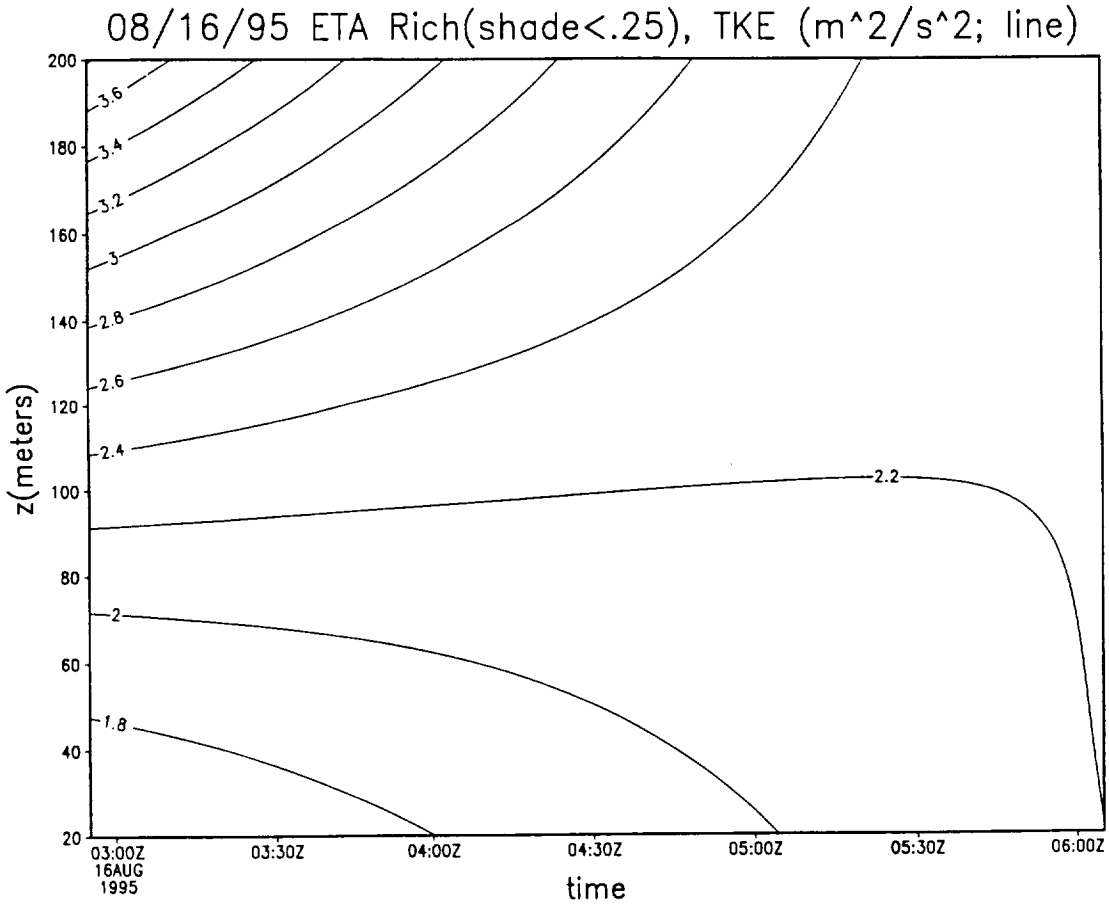
08/16/95 ETA Rich(shade<.25), TKE (m^2/s^2; line)
z(meters)
200
180
160
140
120
100
80
60
40
20
3.6
3.4
3.2
3
2.8
2.6
2.4
2.2
2
1.8
03:00Z
16AUG
1995
03:30Z
04:00Z
04:30Z
05:00Z
05:30Z
06:00Z
time

FIG. 17

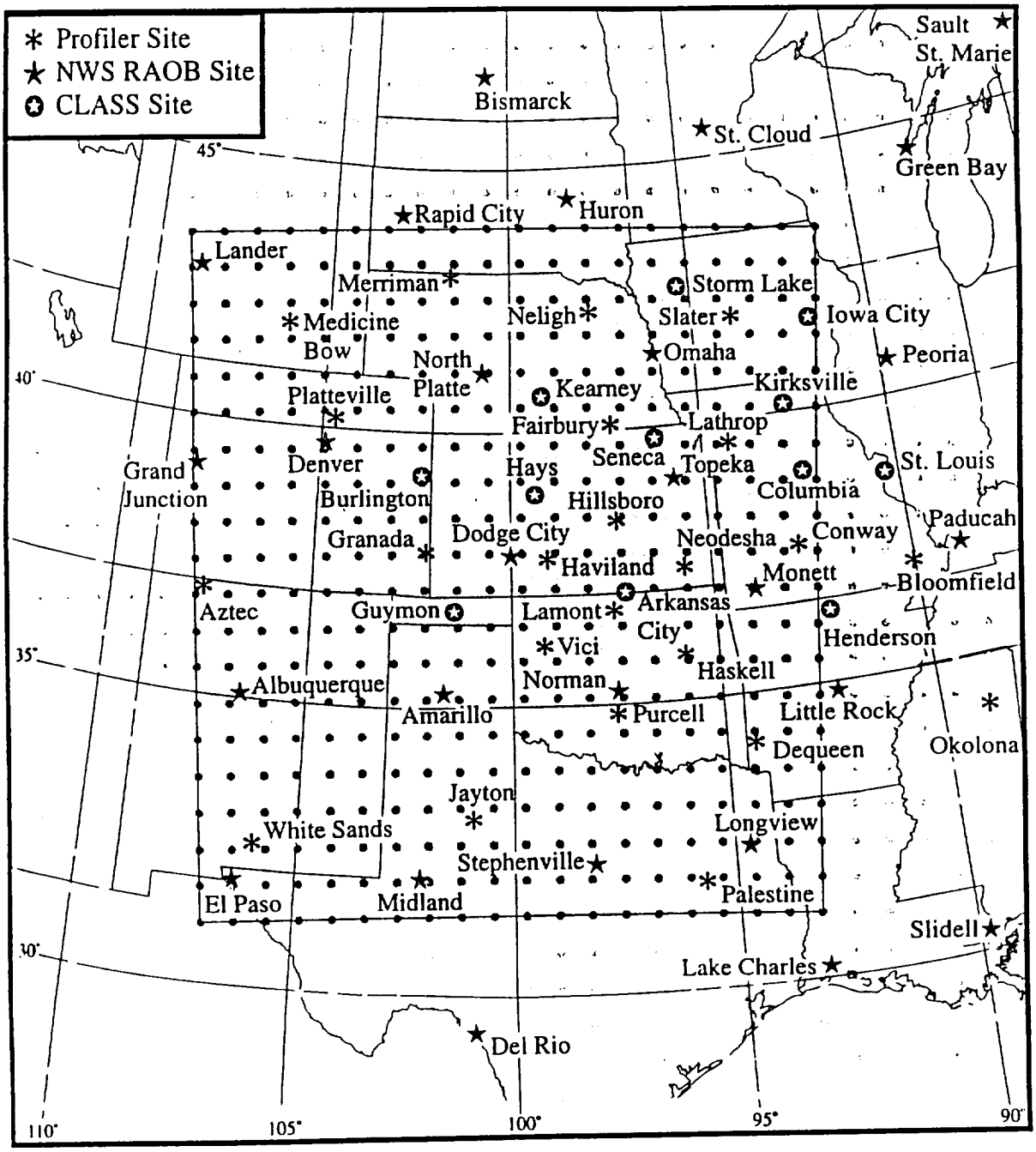
* Profiler Site
★ NWS RAOB Site
✪ CLASS Site
Sault St. Marie
Bismarck
St. Cloud
Green Bay
45°
Rapid City
Huron
Lander
Merriman
Storm Lake
Medicine Bow
Neligh
Slater
Iowa City
Omaha
Peoria
North Platte
Kearney
Kirksville
Platteville
Fairbury
Lathrop
Grand Junction
Denver
Hays
Seneca
Topeka
St. Louis
Burlington
Hillsboro
Columbia
Paducah
Granada
Dodge City
Neodesha
Conway
Haviland
Monett
Bloomfield
Aztec
Guymon
Lamont
Arkansas City
Henderson
Vici
Albuquerque
Norman
Haskell
Amarillo
Purcell
Little Rock
Okolona
Dequeen
Jayton
White Sands
Longview
Stephenville
El Paso
Midland
Palestine
Slidell
30°
Lake Charles
Del Rio
110°
105°
100°
95°
90°

FIG. 18

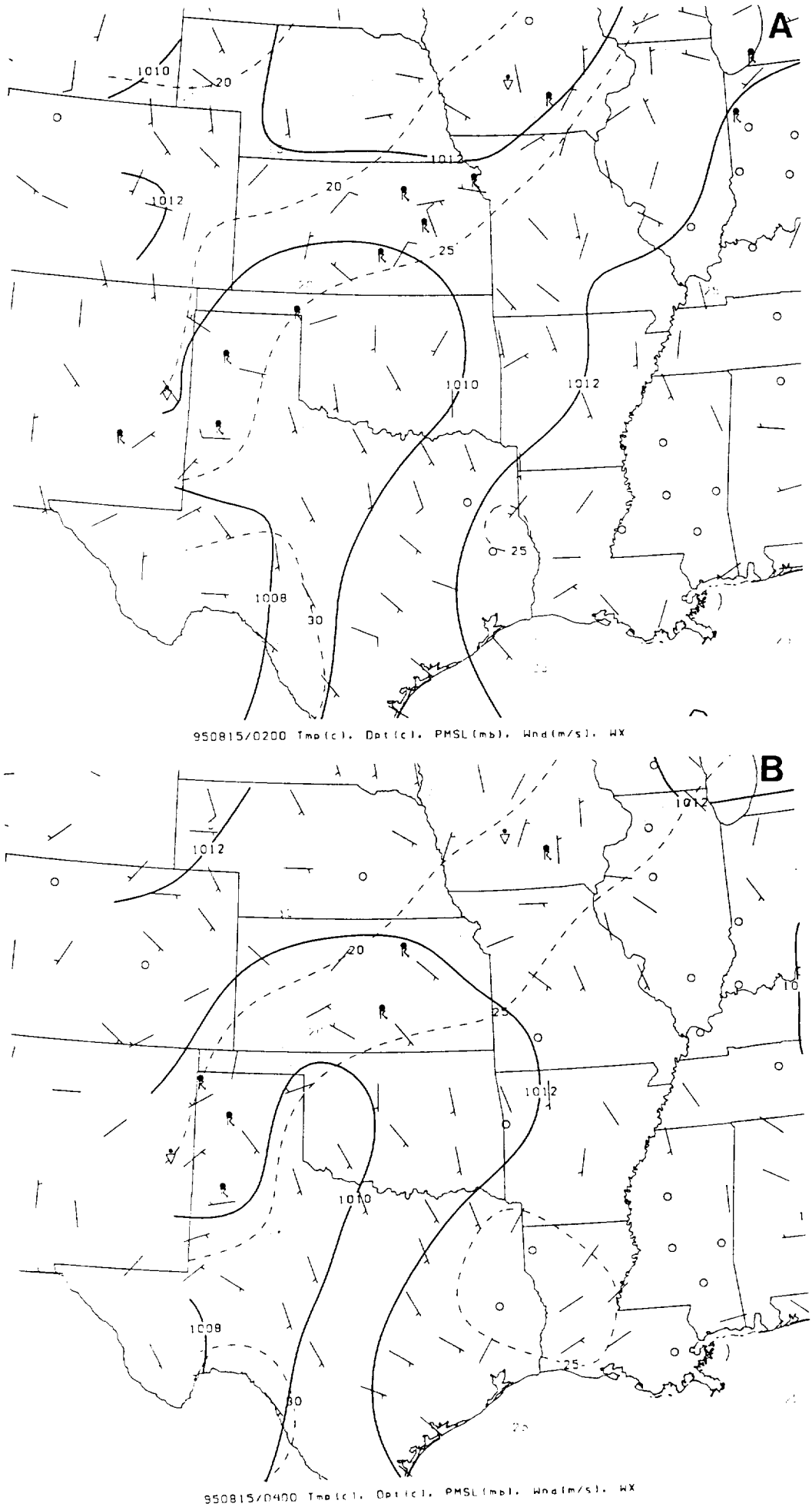
A
1010
20
1012
1012
20
25
1010
1012
25
1008
30
950815/0200 Tmp(c), Dpt(c), PMSL(mb), Wnd(m/s), WX
B
1012
1012
20
25
1012
1010
1008
25
30
950815/0400 Tmp(c), Dpt(c), PMSL(mb), Wnd(m/s), WX

FIG. 19A-B

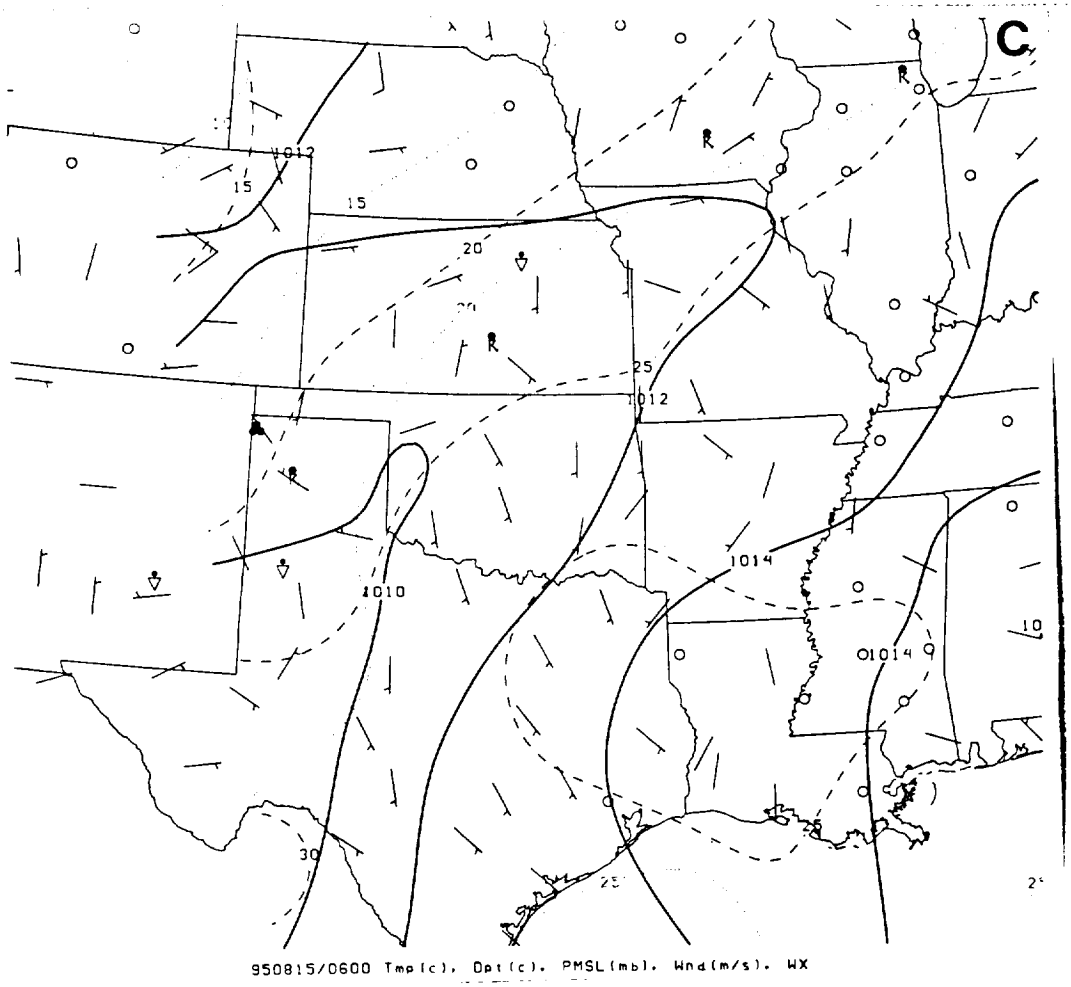
C
1012
15
15
20
R
R
25
1012
1010
1014
10
01014
30
25
950815/0600 Tmp(c), Dpt(c), PMSL(mb), Wnd(m/s), WX

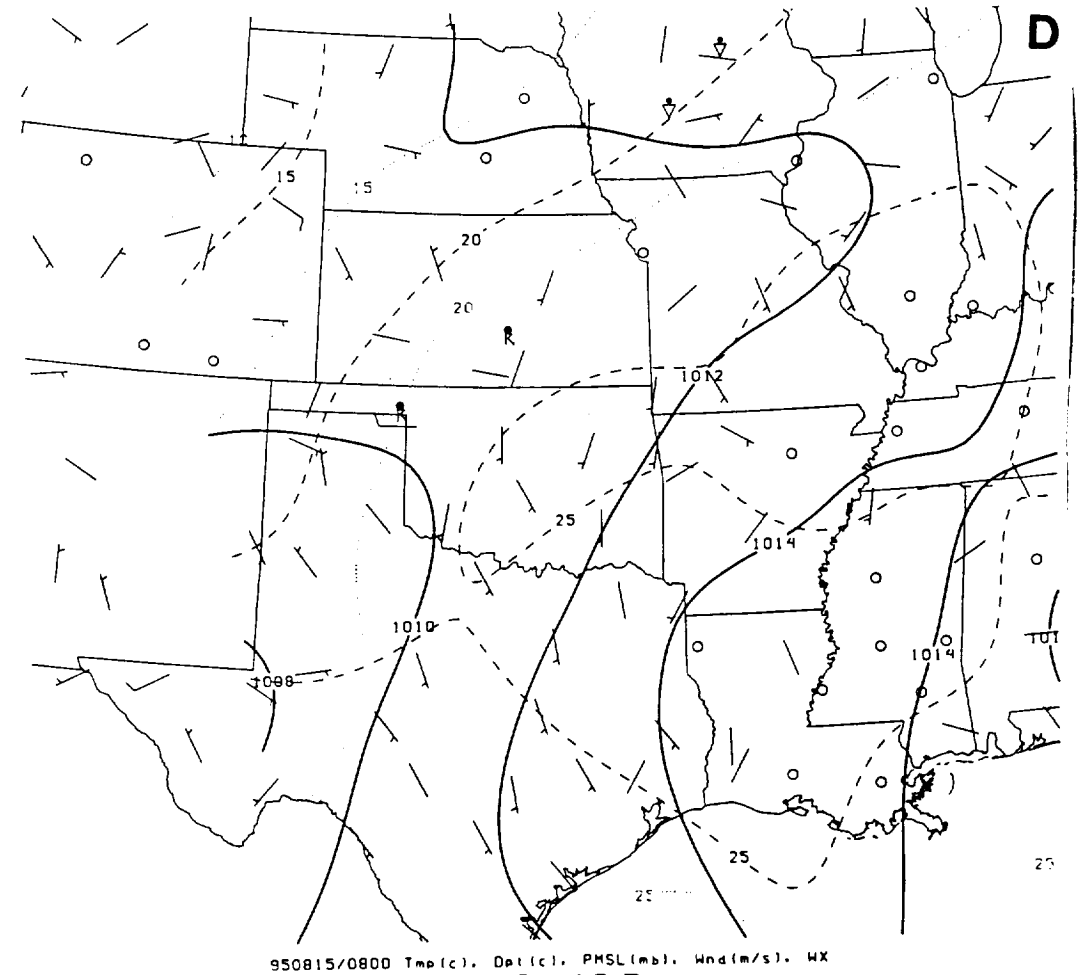
D
15
15
20
20
R
1012
25
1014
1010
1008
1014
25
950815/0800 Tmp(c), Dpt(c), PMSL(mb), Wnd(m/s), WX

FIG. 19C-D

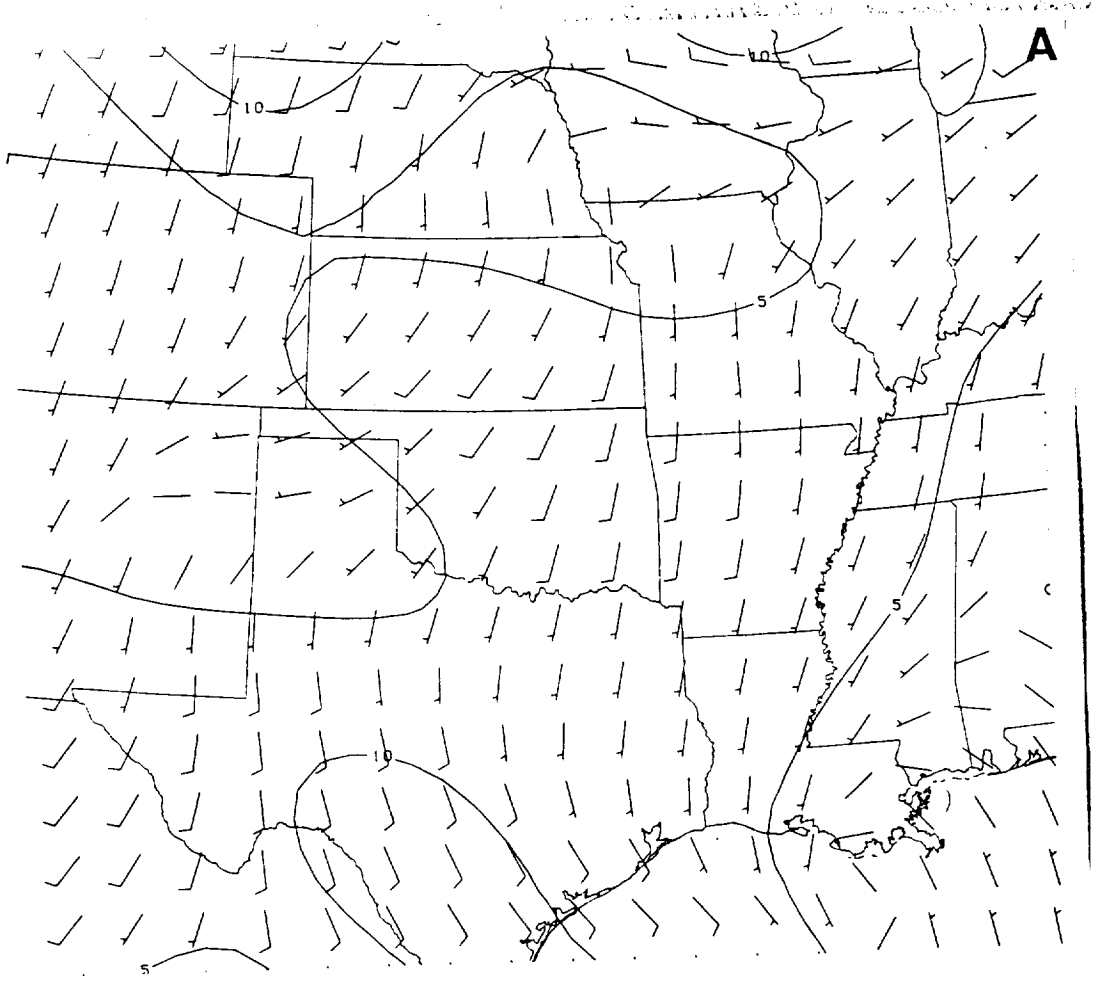

950815/0200 850 MB Interpolated RAOB Winds

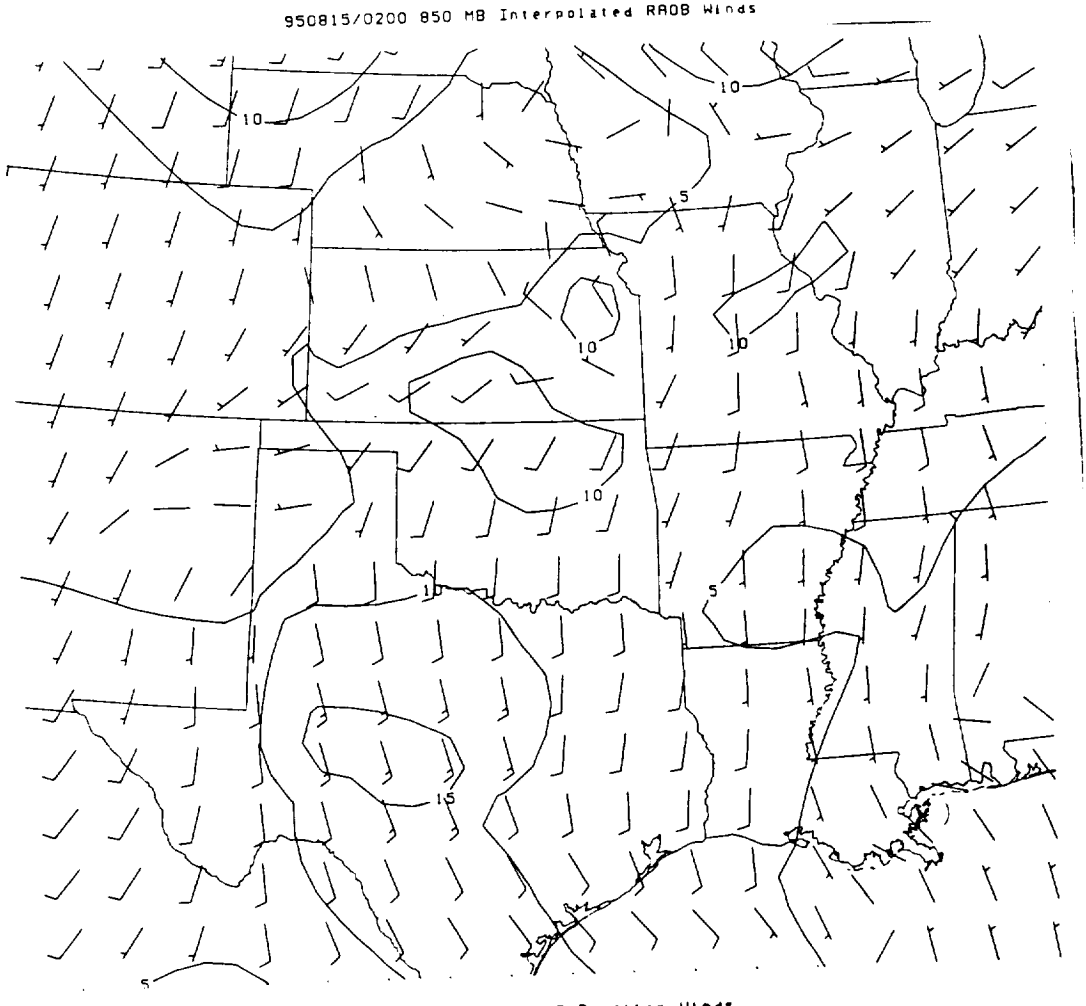

950815/0200 850 MB Profiler Winds

FIG. 20A

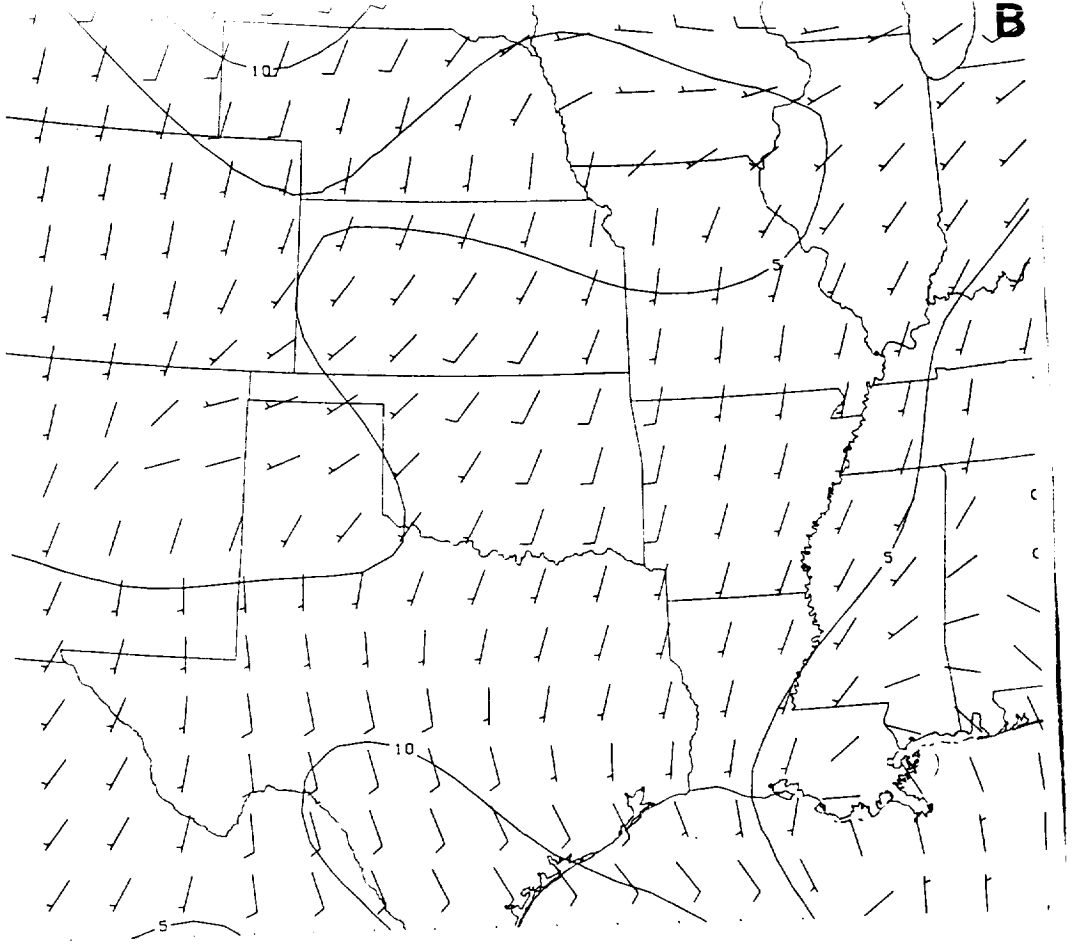
B
10
5
10
5
950815/0400 850 MB Interpolated RAOB Winds

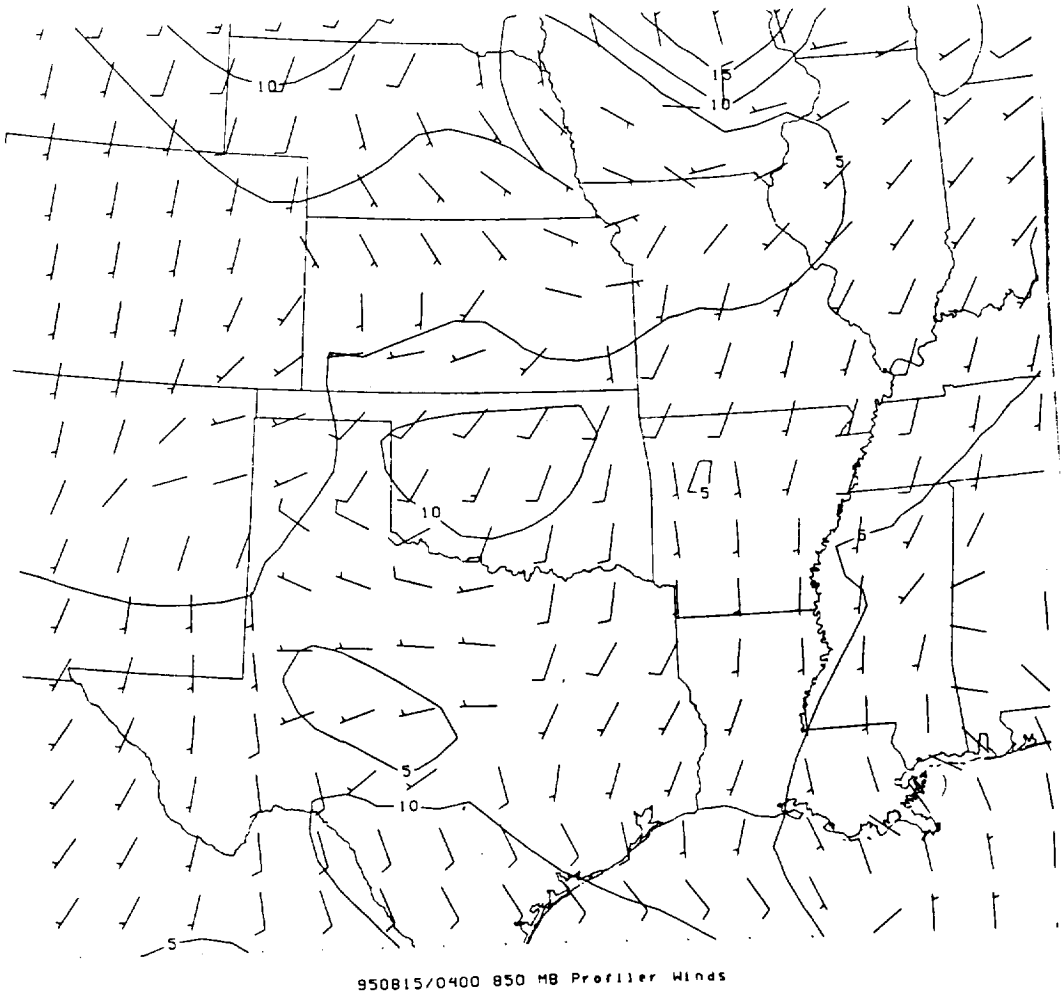
10
15
10
5
10
5
5
10
5
950815/0400 850 MB Profiler Winds

FIG. 20B

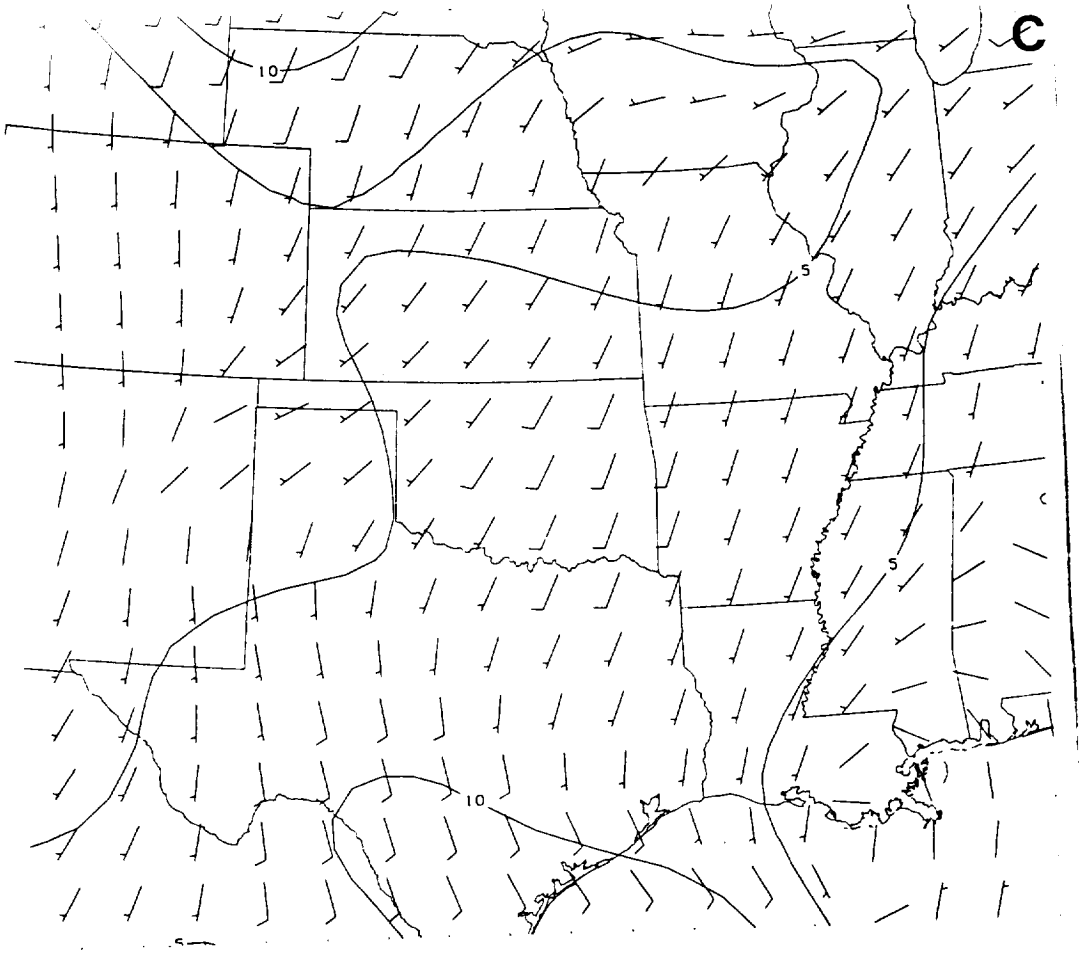

950815/0600 850 MB Interpolated RAOB Winds

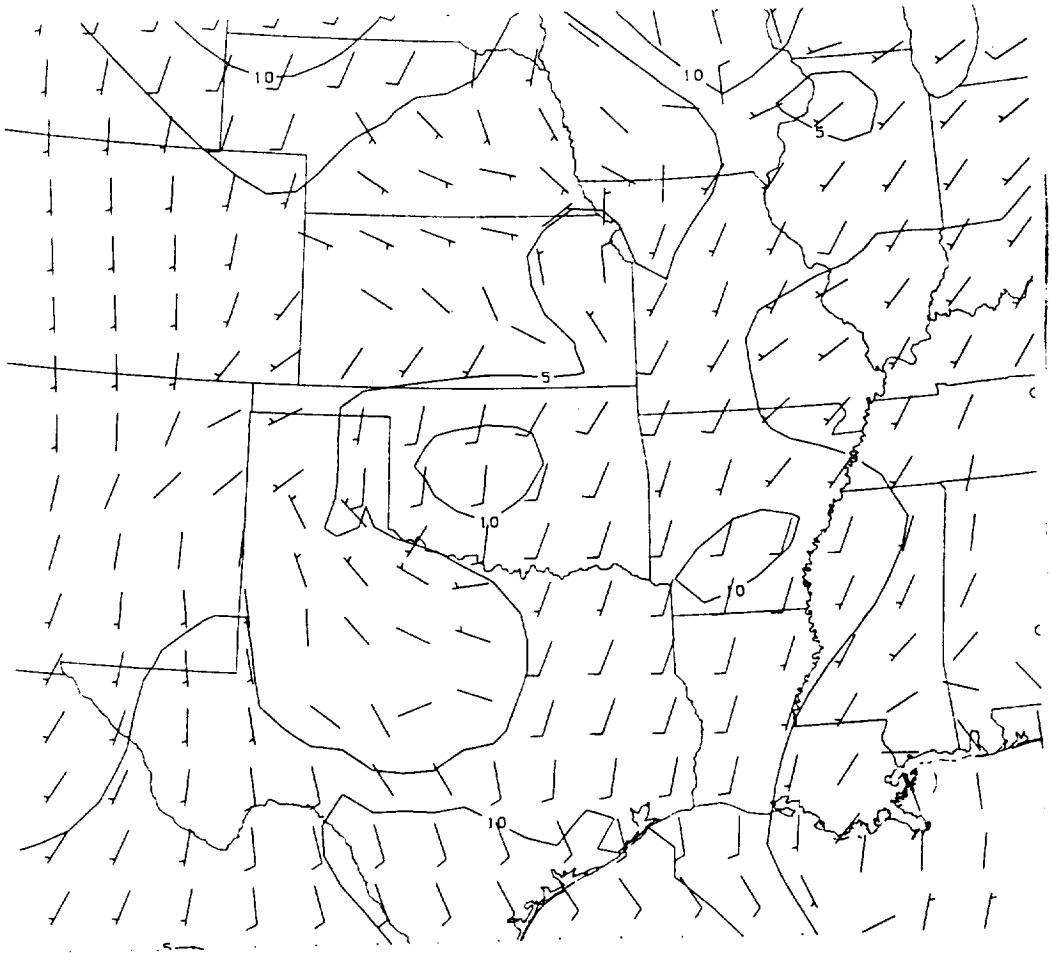

950815/0600 850 MB Profiler Winds

FIG. 20C

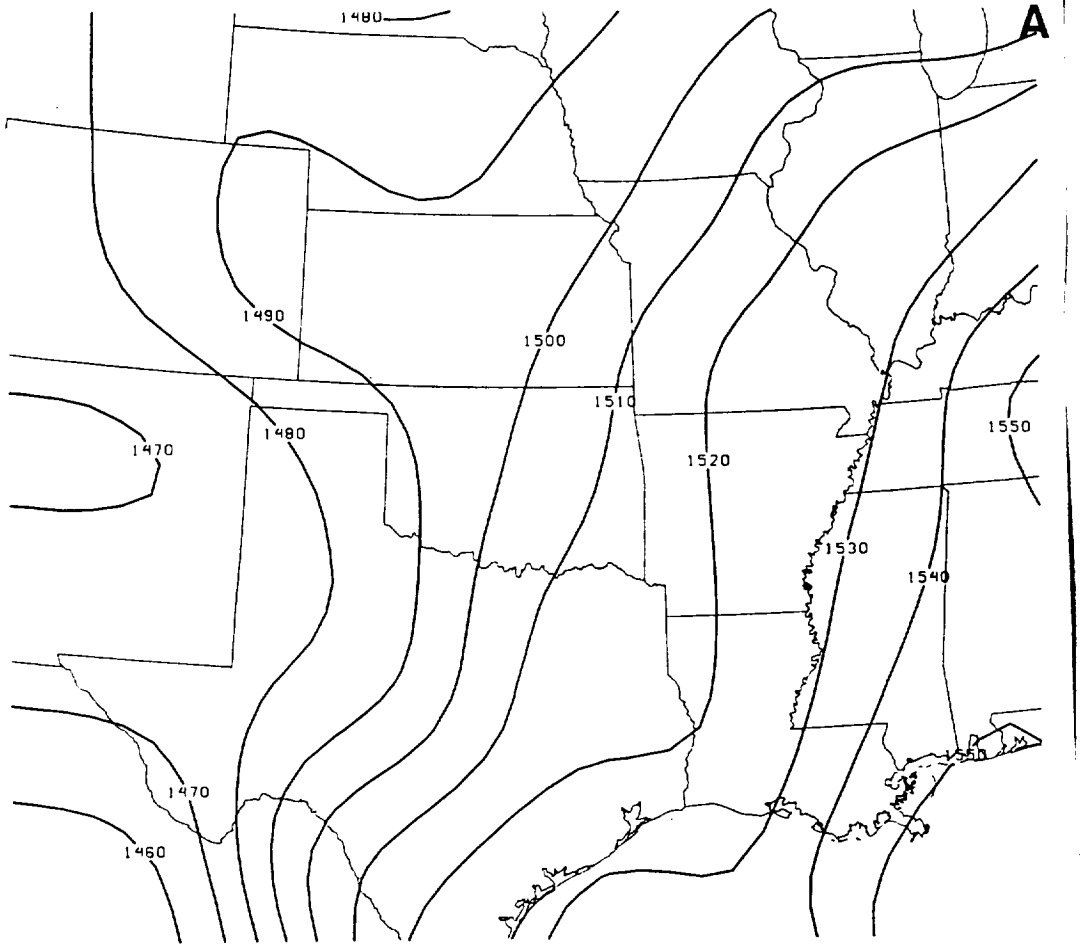

950815/0200 850 MB Interpolated RAOB Heights

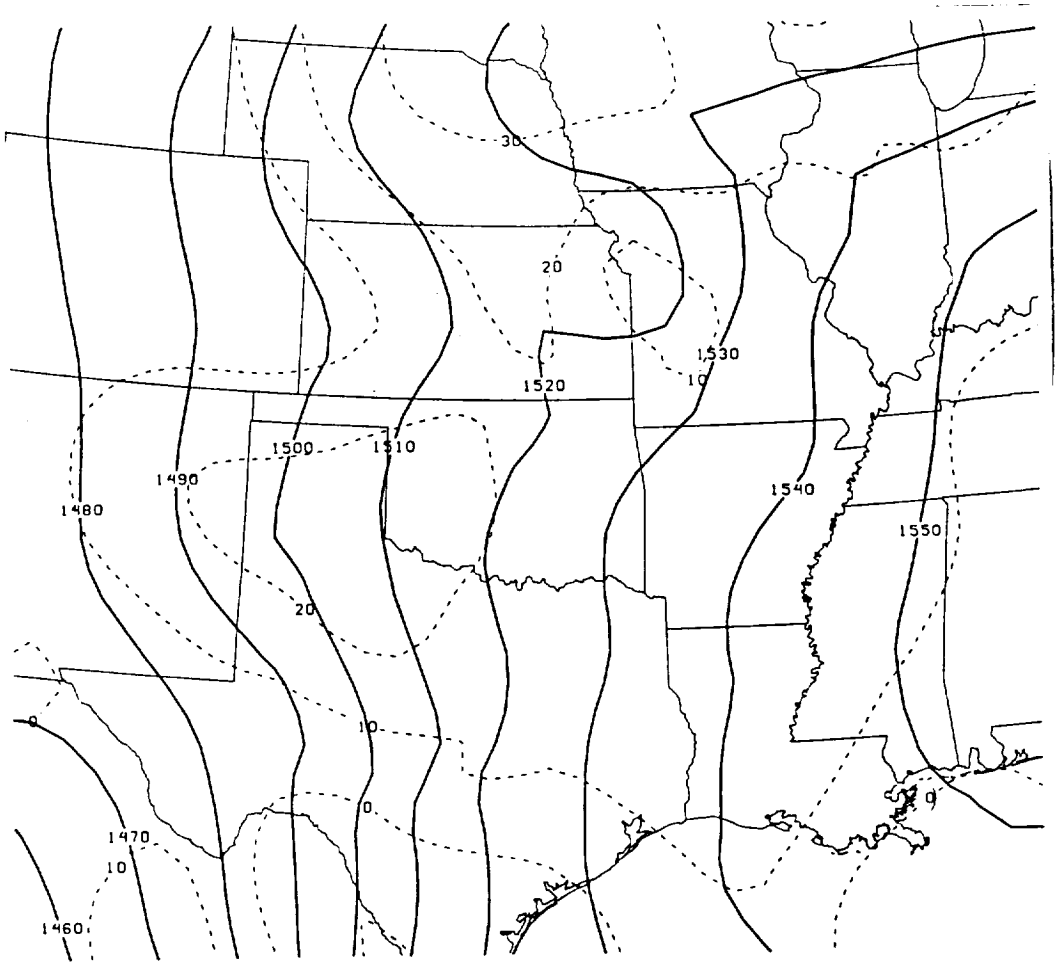

950815/0200 850 MB Derived Height & (Derived-RAOB)

FIG. 21A

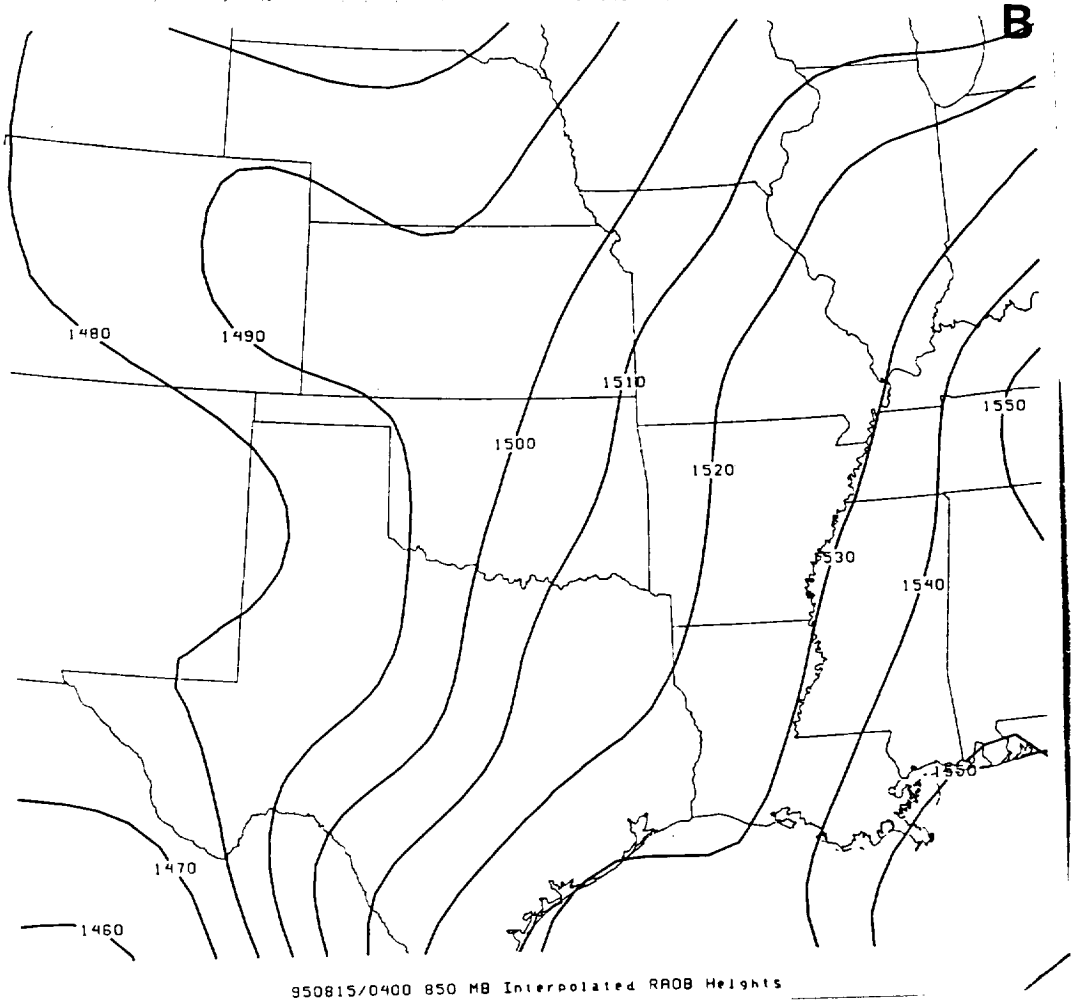

950815/0400 850 MB Interpolated RAOB Heights

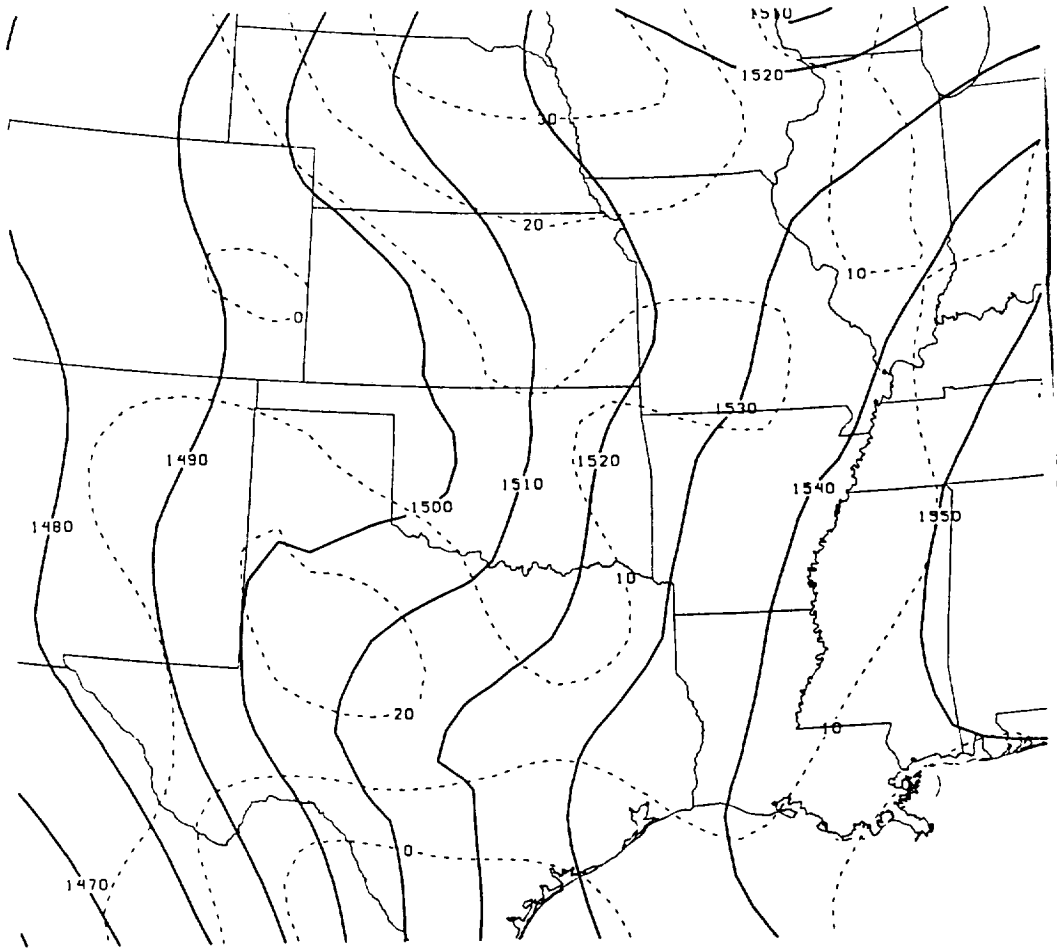

950815/0400 850 MB Derived Height & (Derived-RAOB)

FIG. 21B

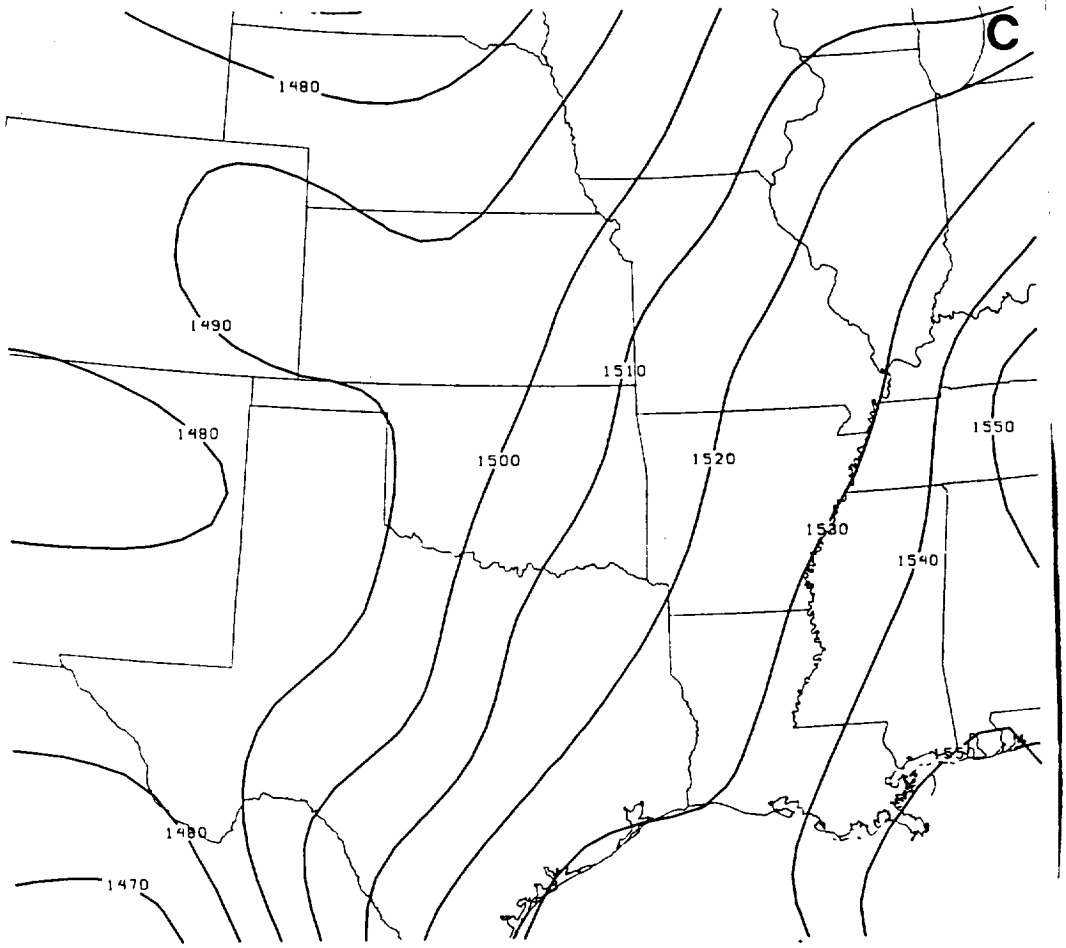

950815/0600 850 MB Interpolated RAOB Heights

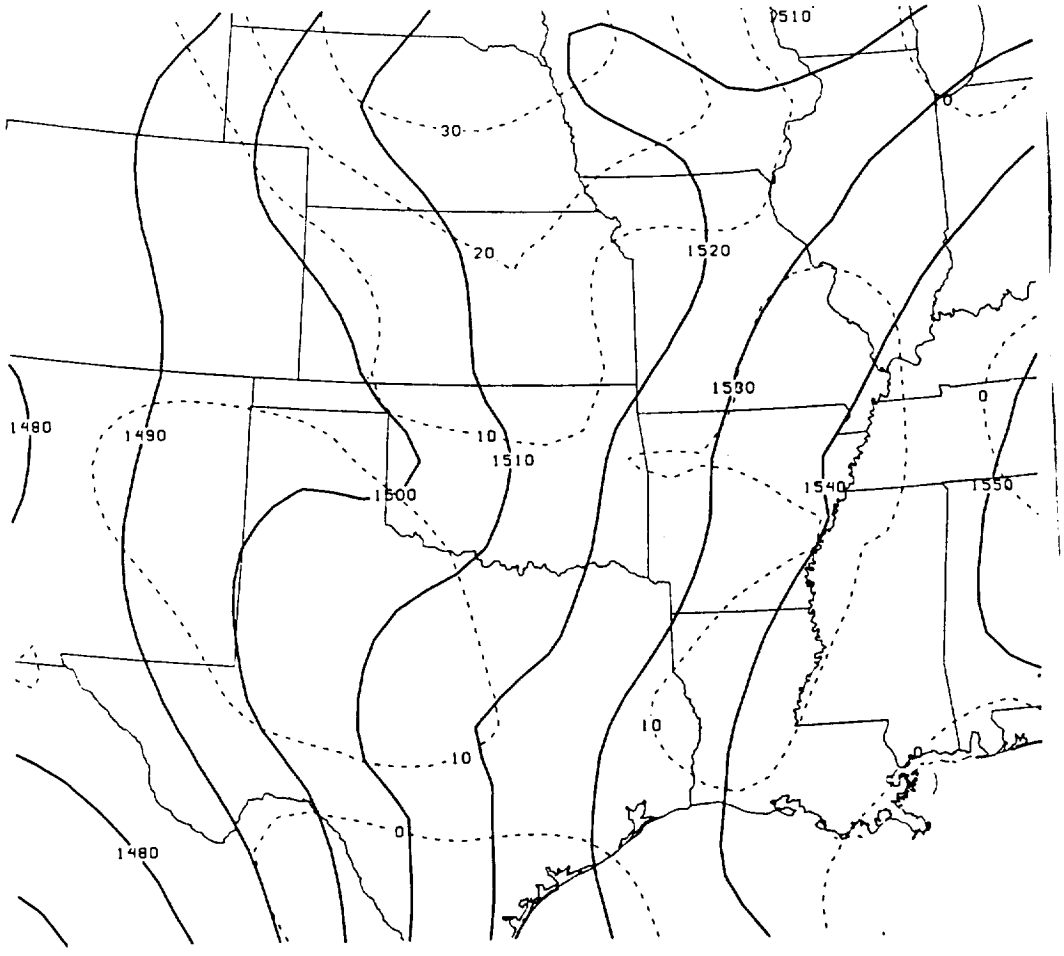

950815/0600 850 MB Derived Height & (Derived-RAOB)

FIG. 21C

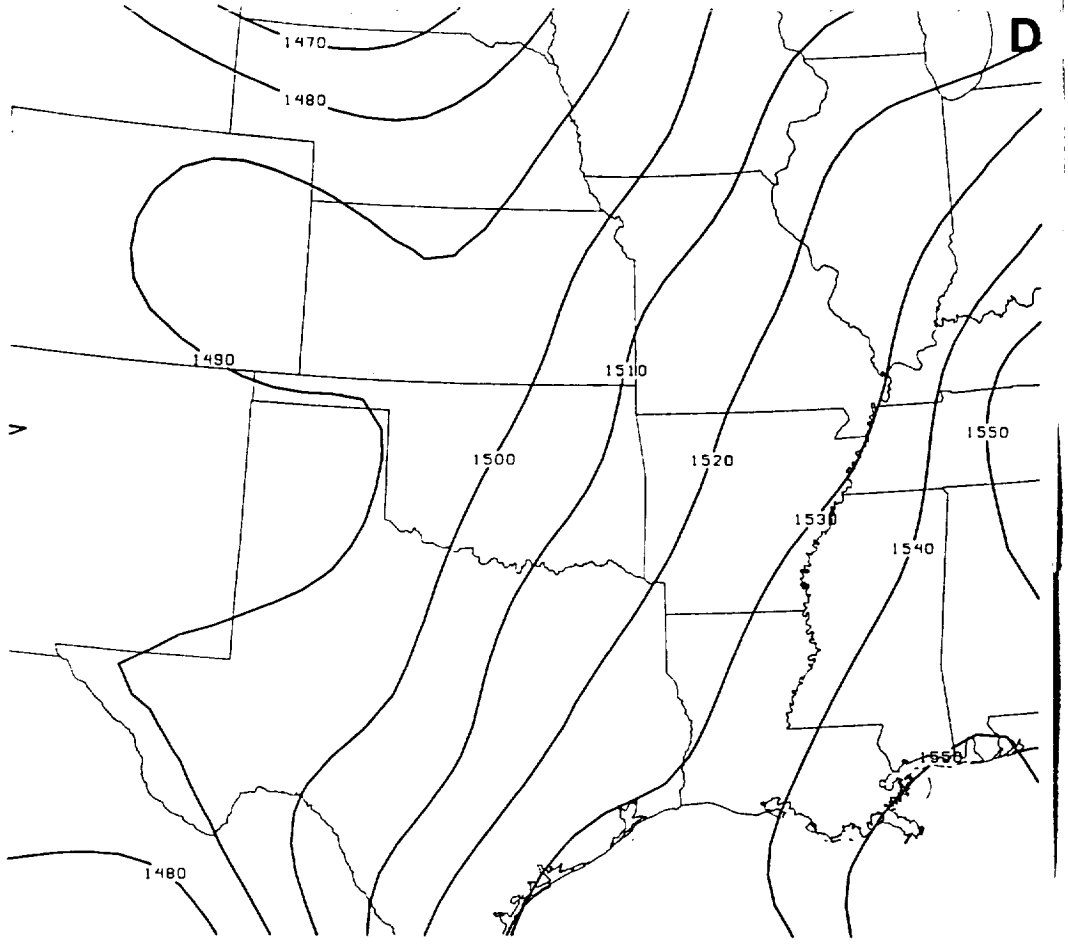

950815/0800 850 MB Interpolated RAOB Heights

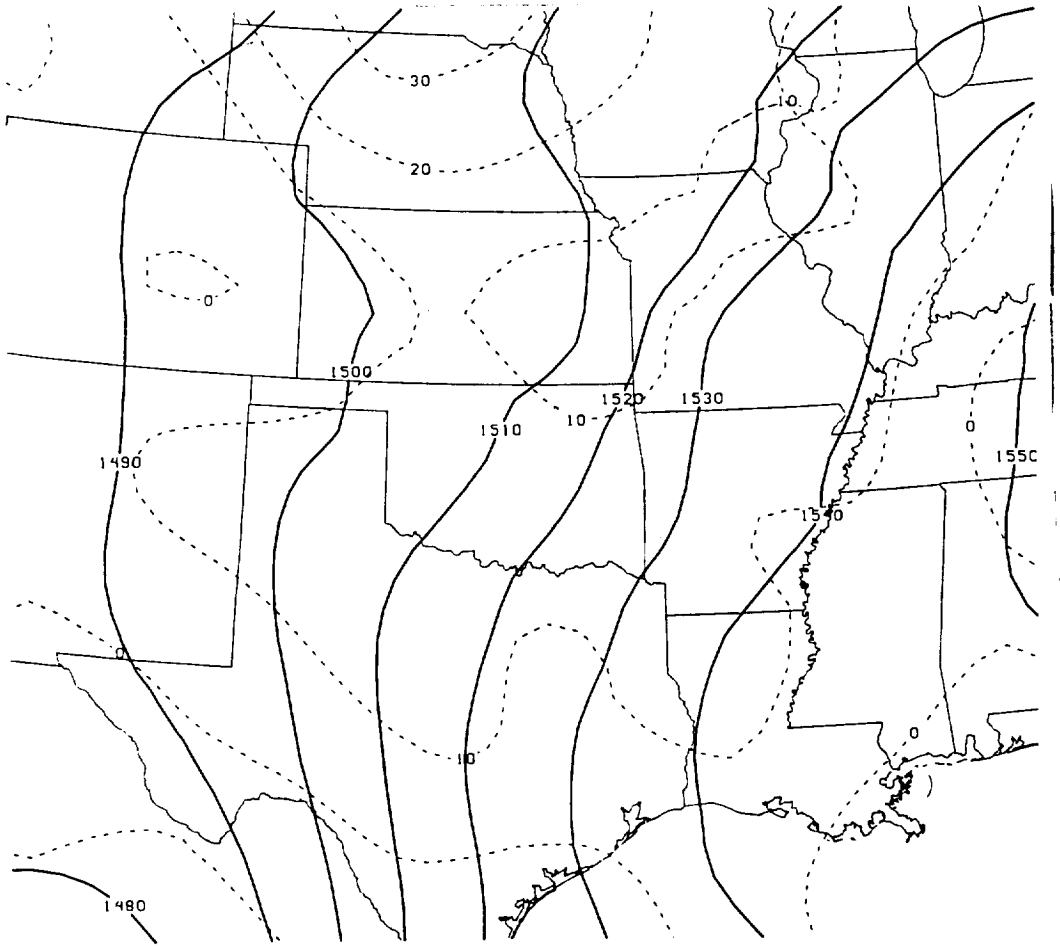

950815/0800 850 MB Derived Height & (Derived-RAOB)

FIG. 21D

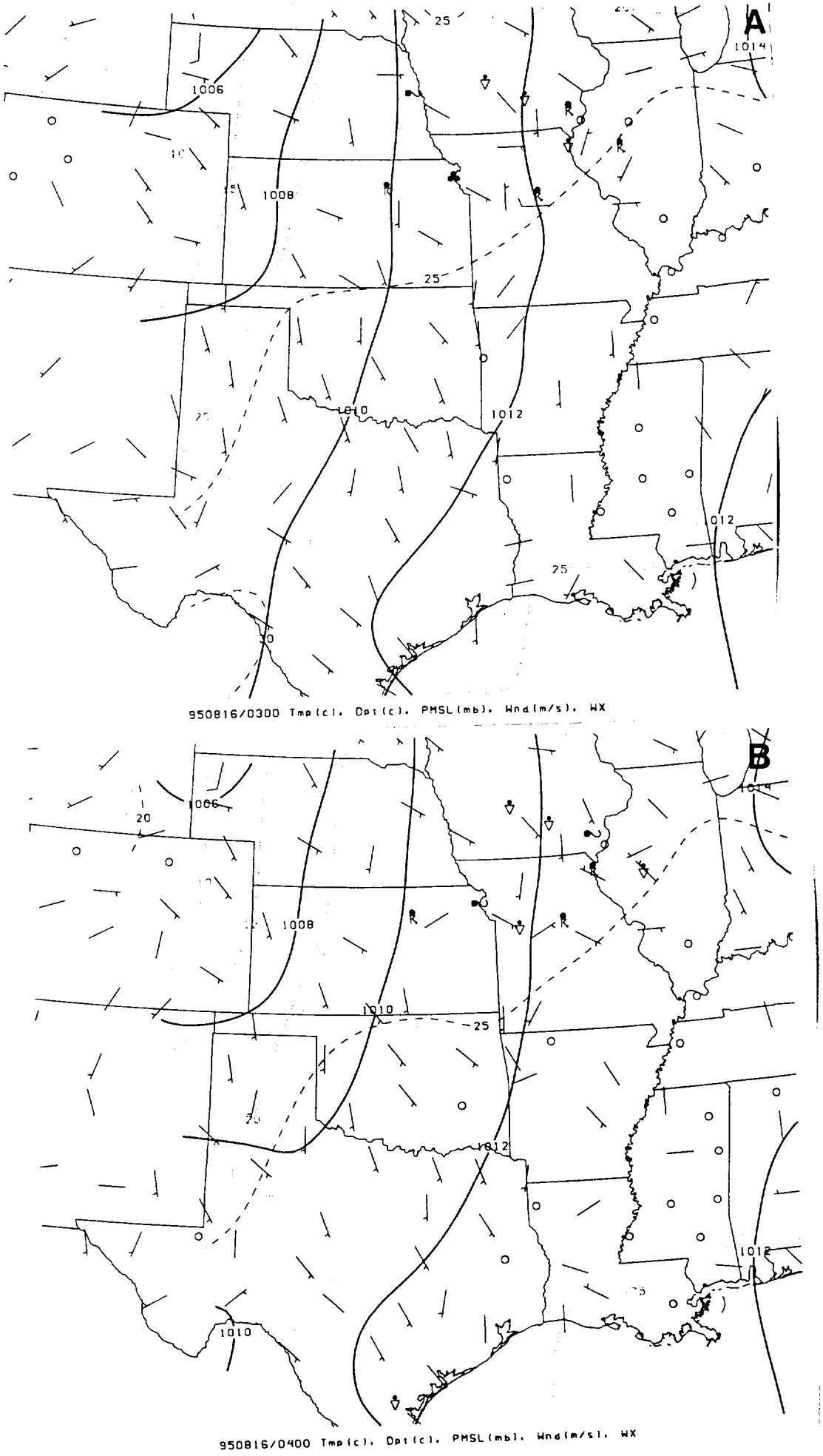
A
1014
1006
1008
25
1010
1012
950816/0300 Tmp(c), Dpt(c), PMSL(mb), Wnd(m/s), WX
B
1014
1006
20
1008
1010
25
1012
950816/0400 Tmp(c), Dpt(c), PMSL(mb), Wnd(m/s), WX

FIG. 22 A-B

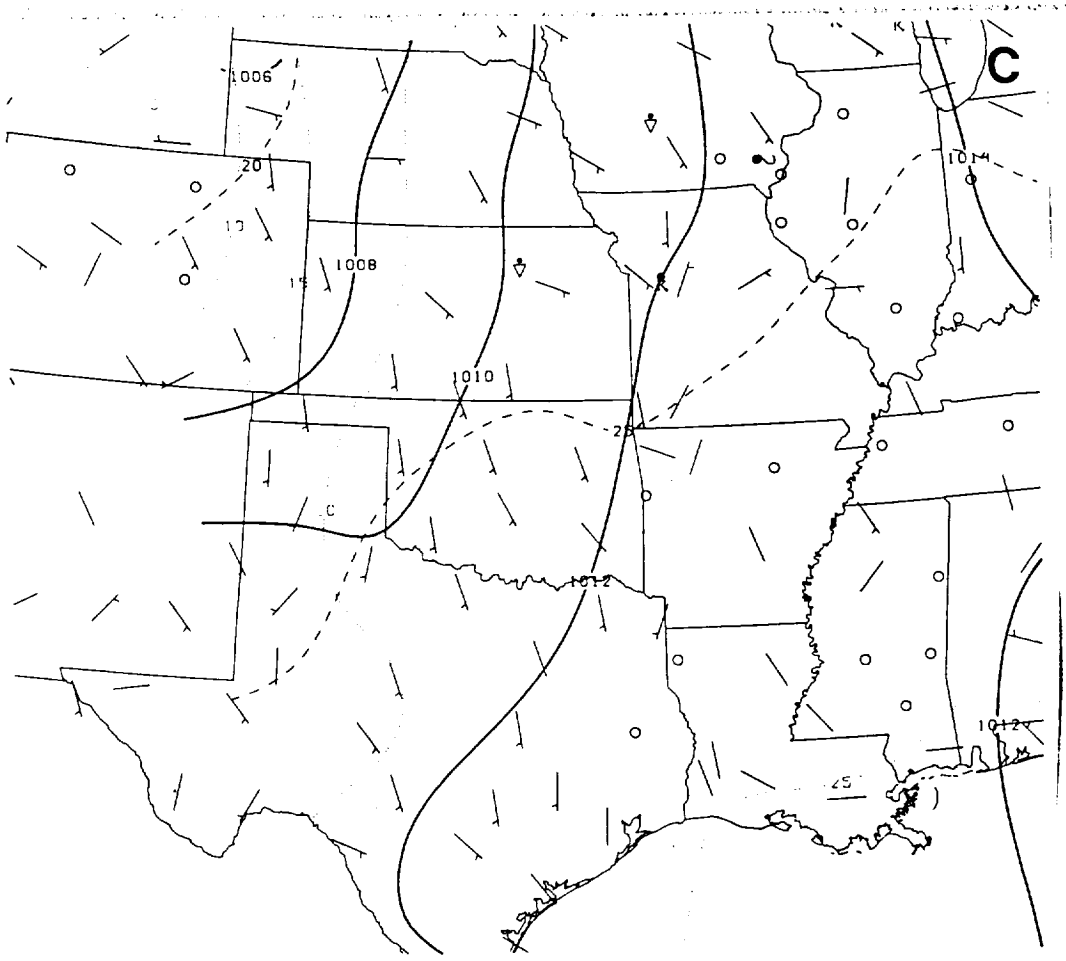
C
1006
1008
1010
1012
1014
20
25
950816/0500 Tmp(c), Dpt(c), PMSL(mb), Wnd(m/s), WX

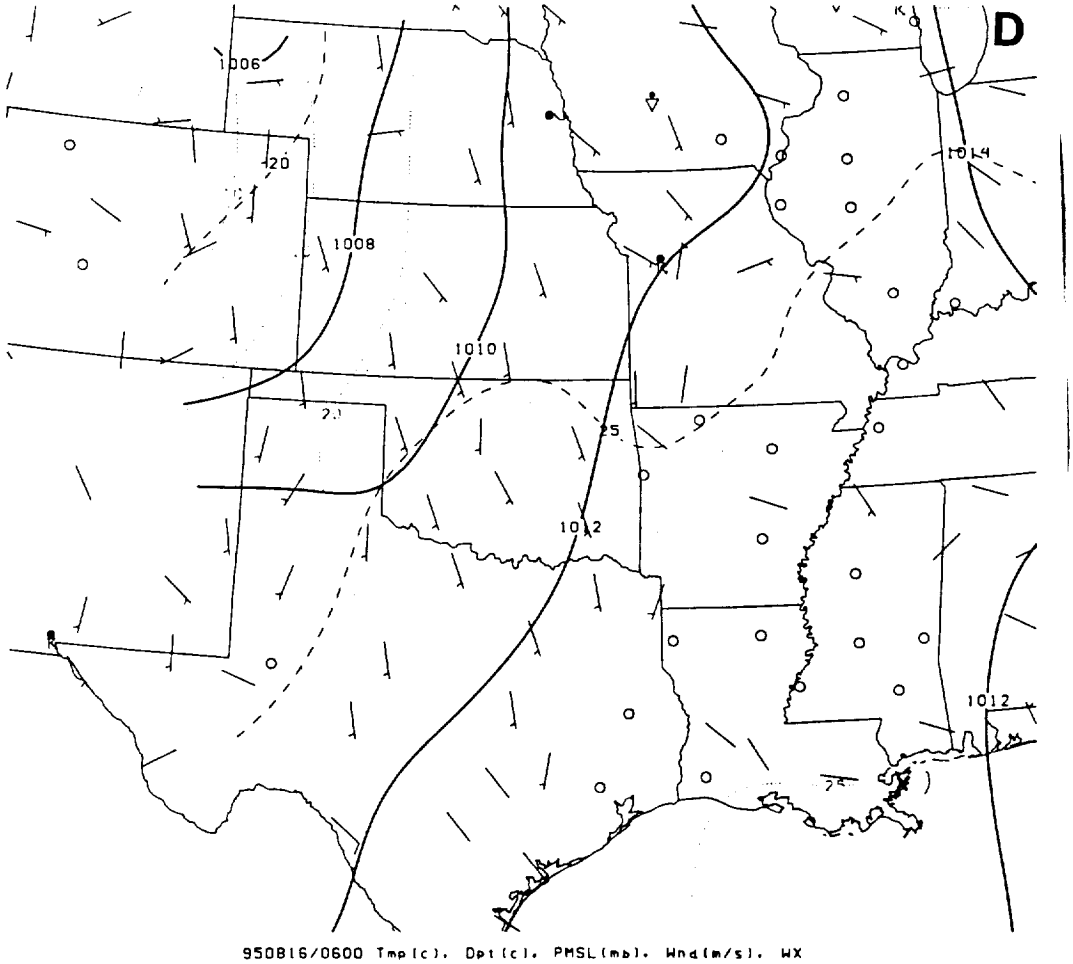
D
1006
1008
1010
1012
1014
20
25
950816/0600 Tmp(c), Dpt(c), PMSL(mb), Wnd(m/s), WX

FIG. 22C-D

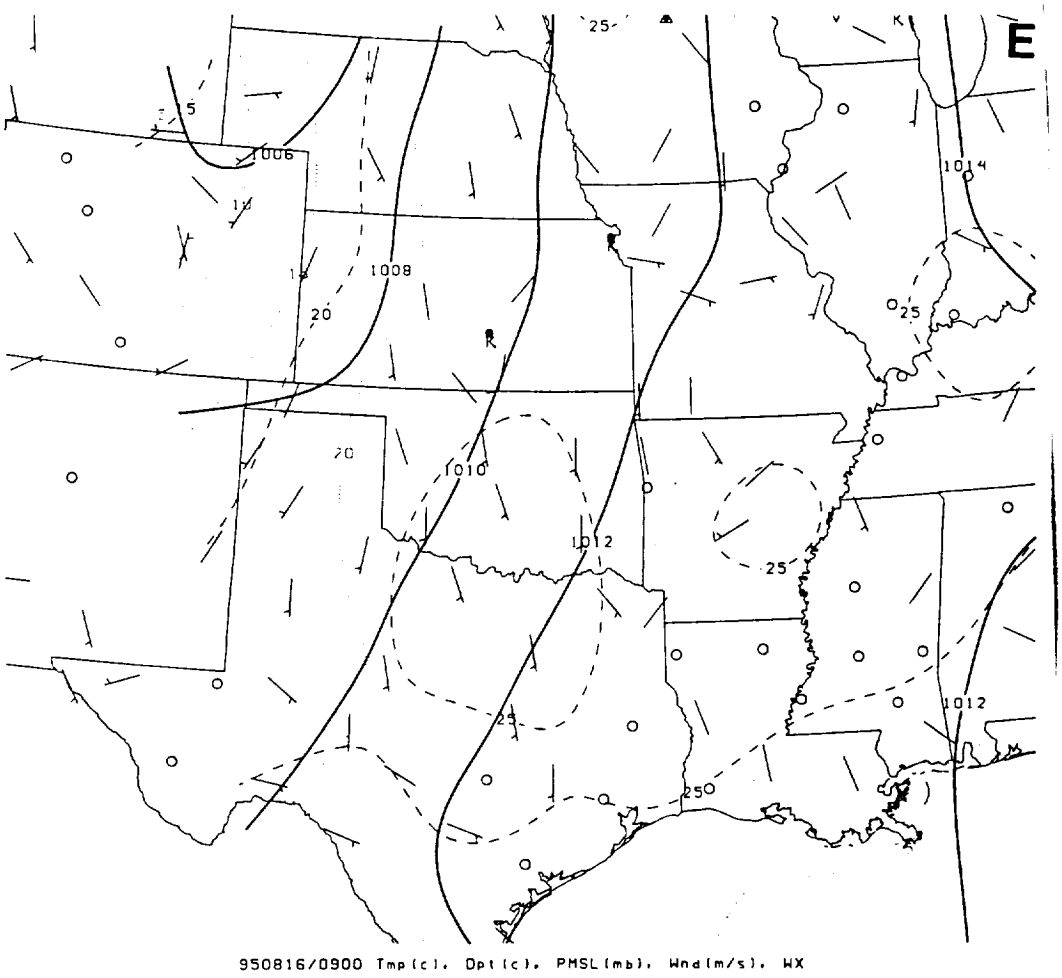
E
1006
1008
1010
1012
1014
950816/0900 Tmp(c), Dpt(c), PMSL(mb), Wnd(m/s), WX

FIG. 22E

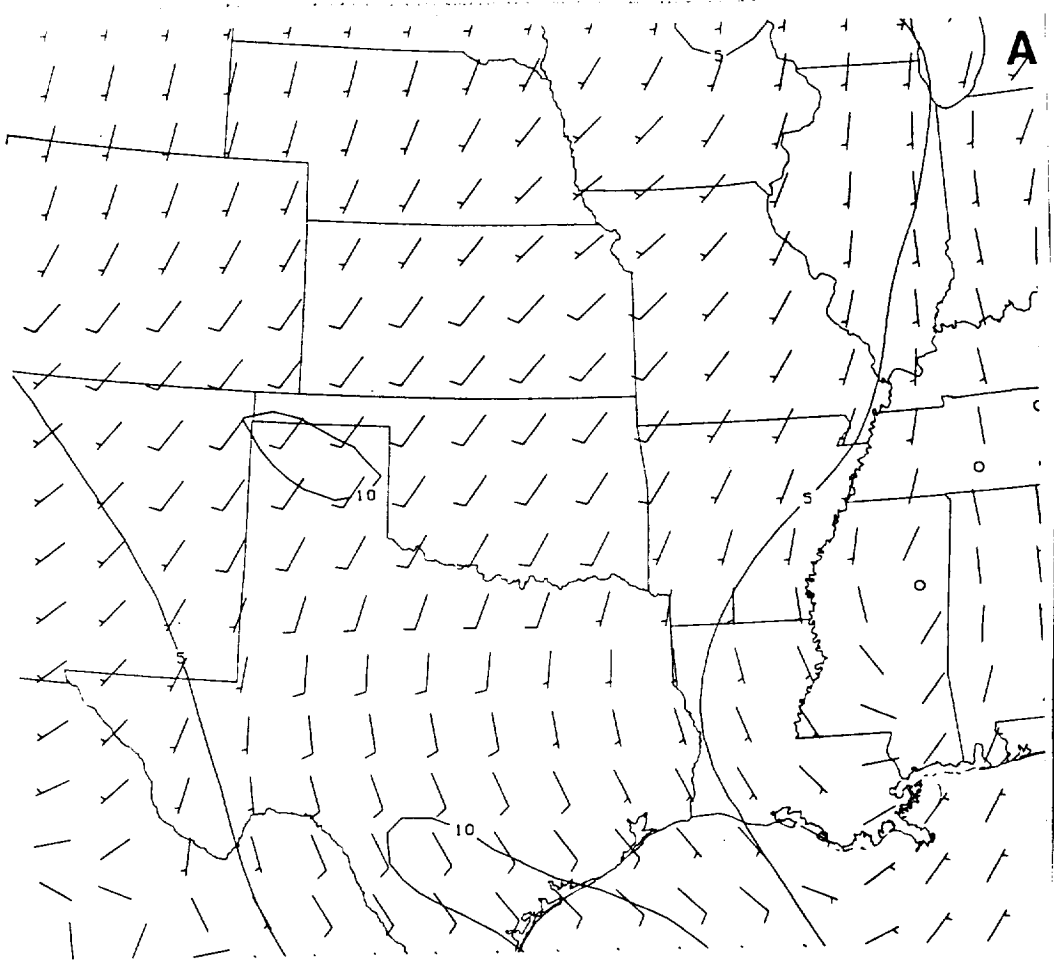

950816/0300 850 MB Interpolated RAOB Winds

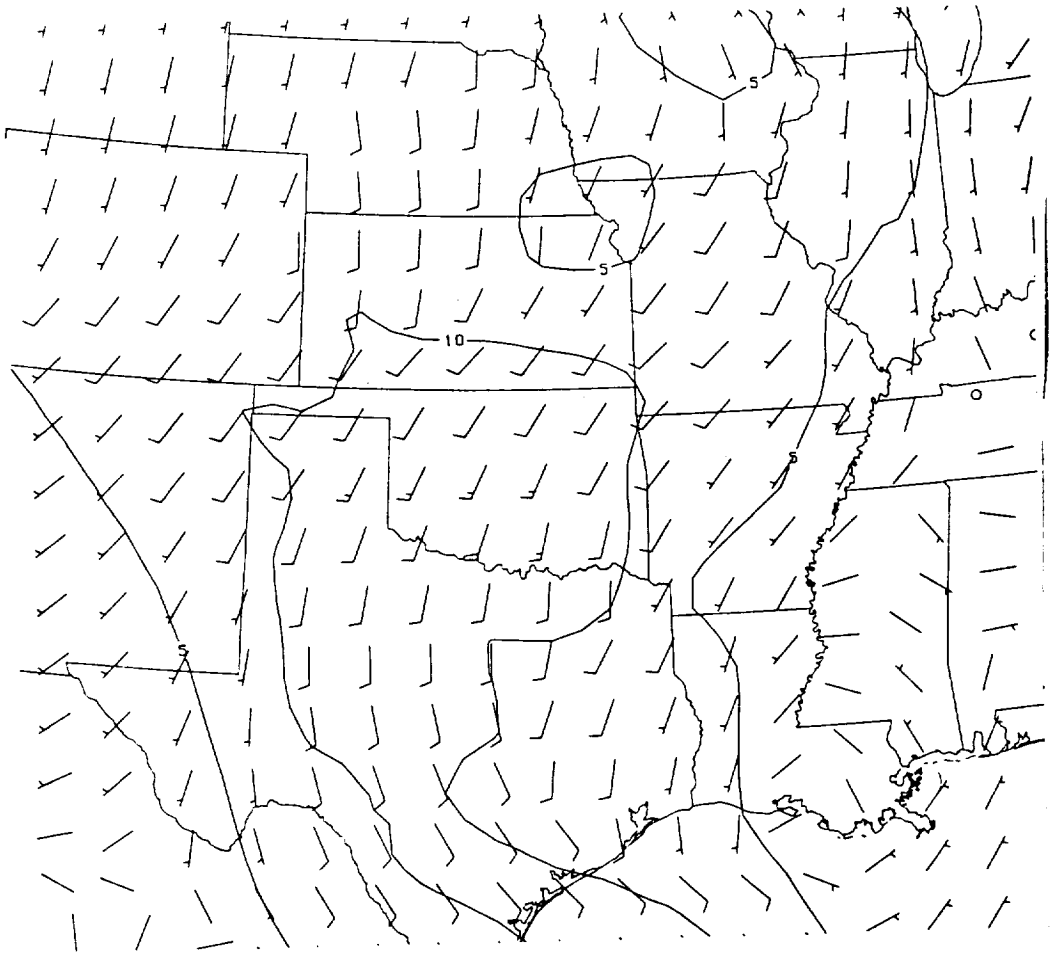

950816/0300 850 MB Profiler Winds

FIG. 23A

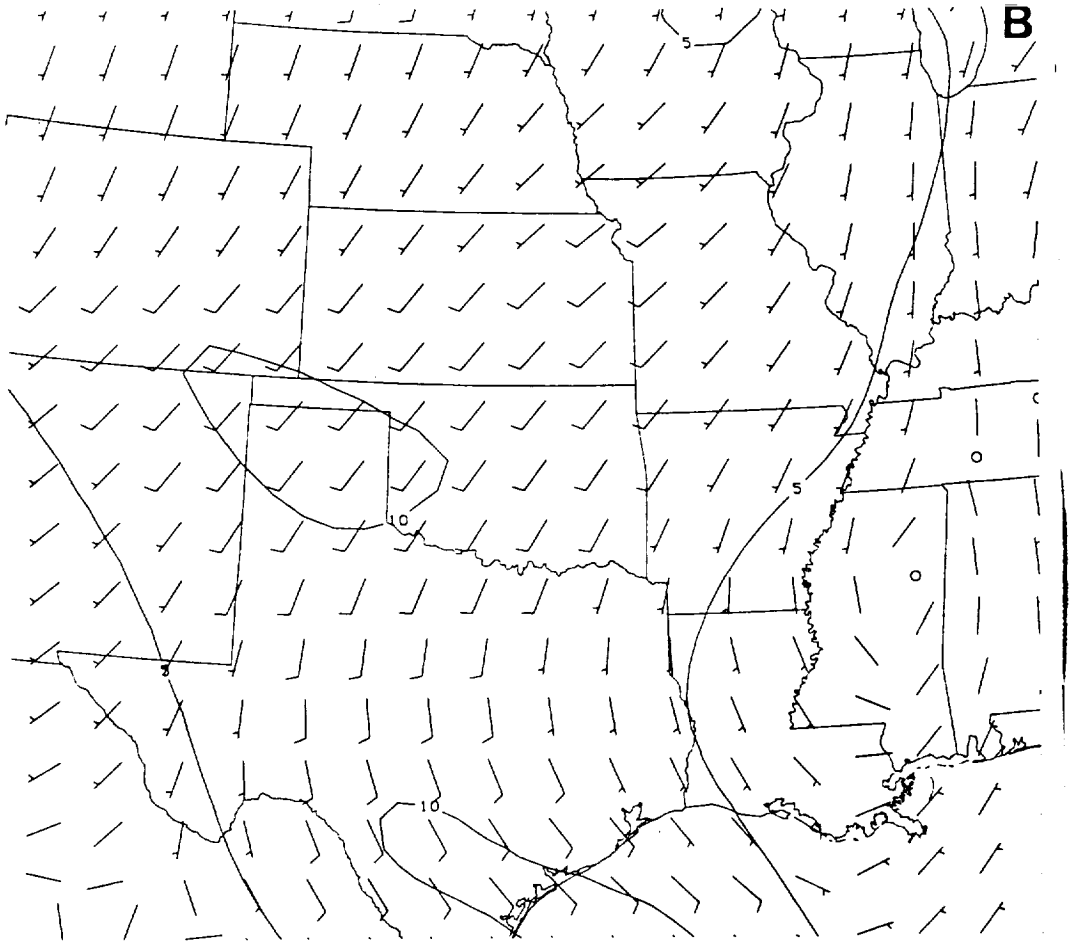

950816/0400 850 MB Interpolated RAOB Winds

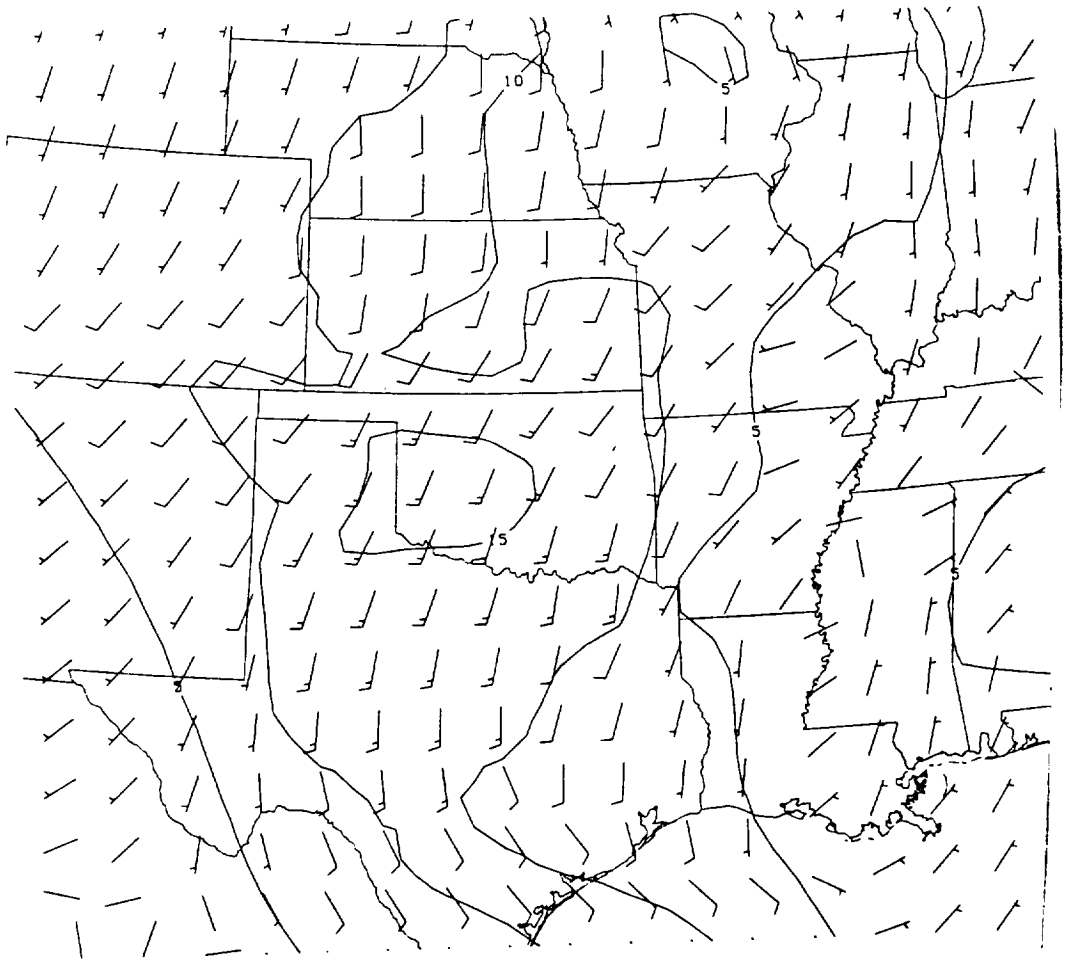

950816/0400 850 MB Profiler Winds

FIG. 23B

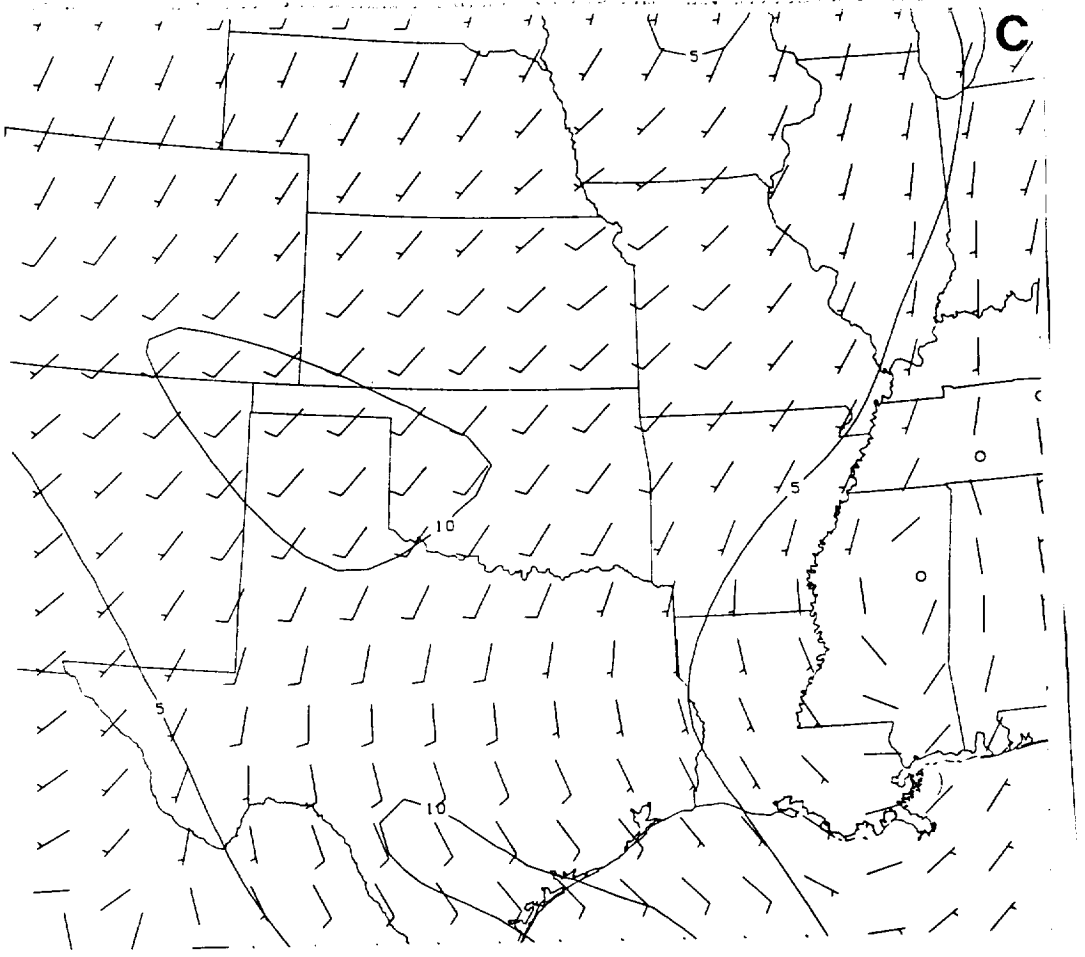

950816/0500 850 MB Interpolated RAOB Winds

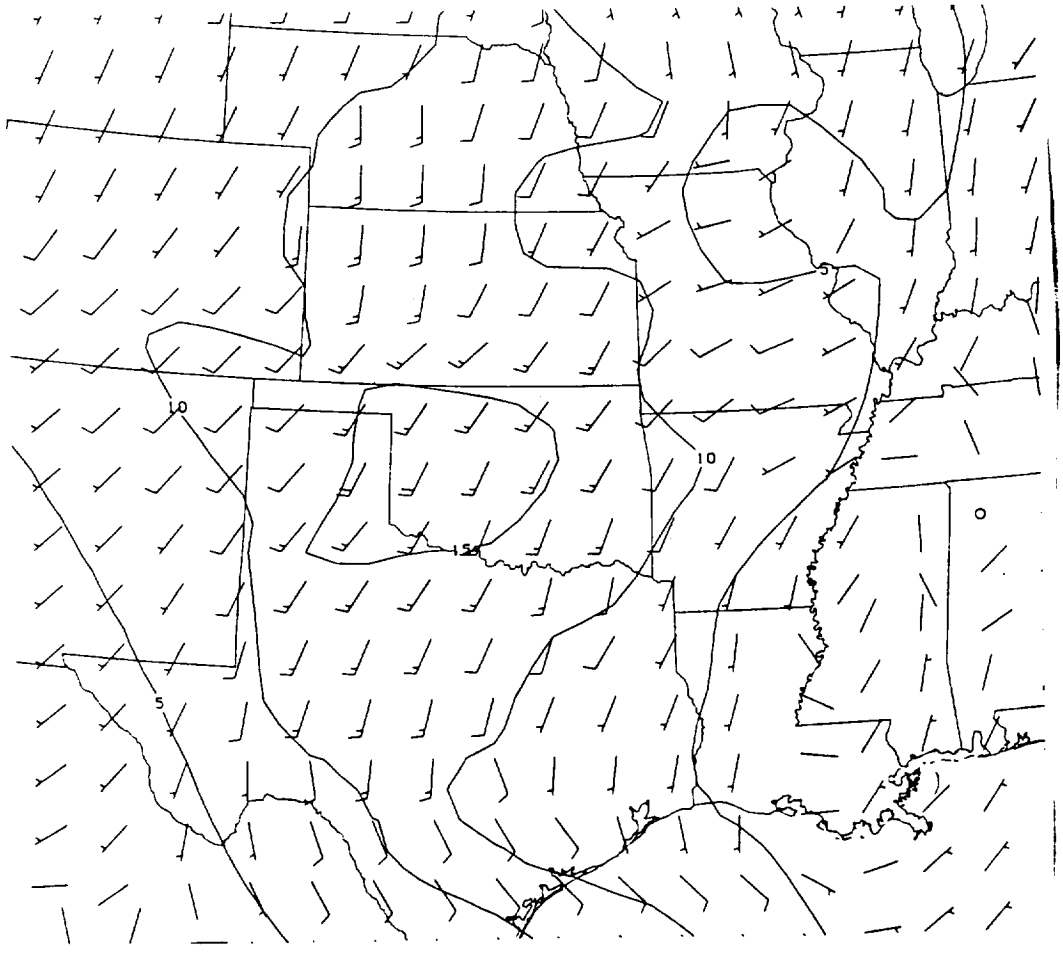

950816/0500 850 MB Profiler Winds

FIG. 23C

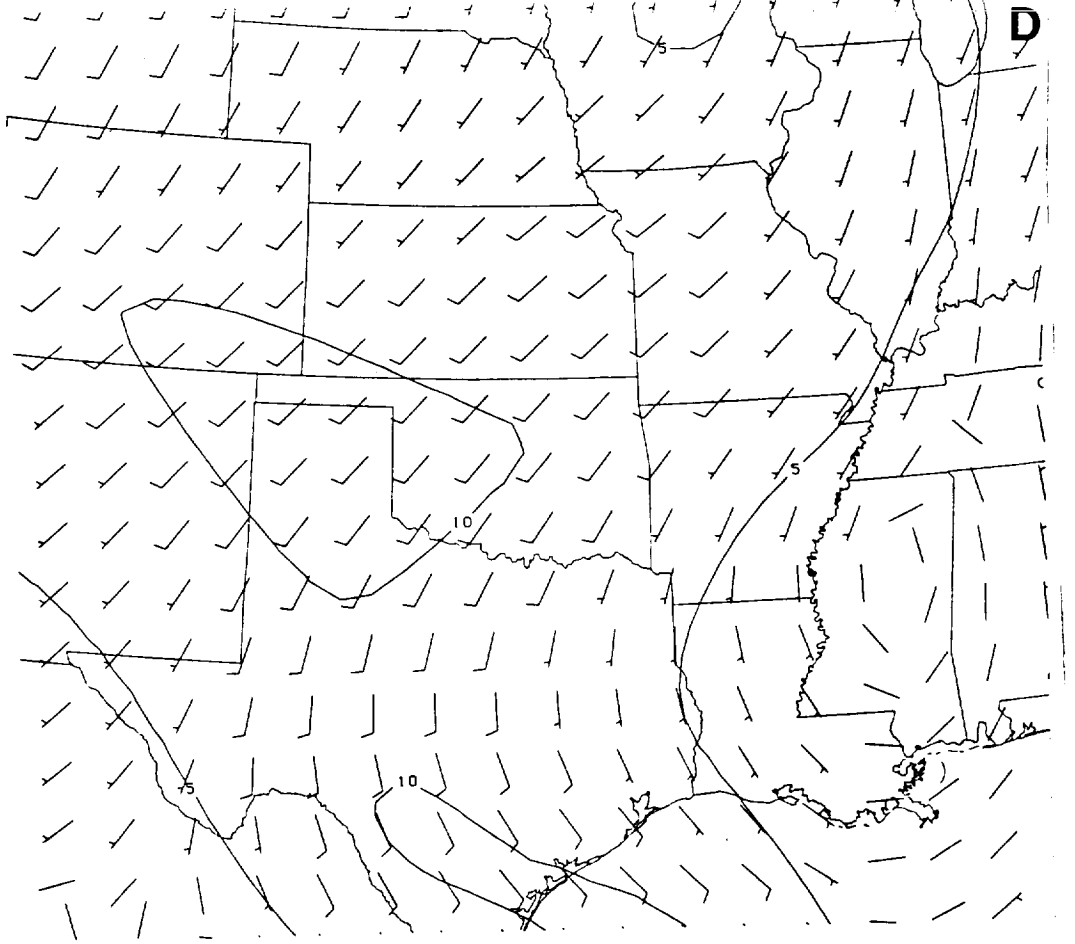

950816/0600 850 MB Interpolated RAOB Winds

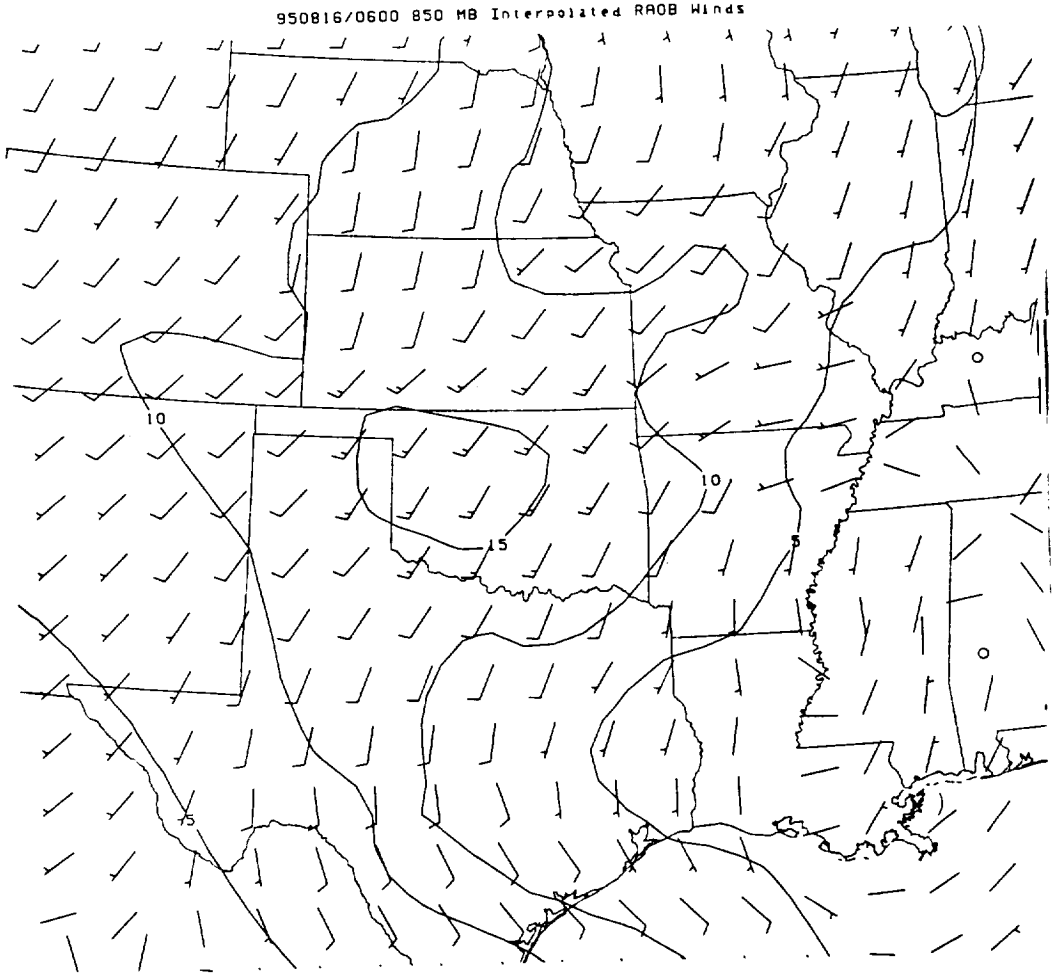

950816/0600 850 MB Profiler Winds

FIG. 23D

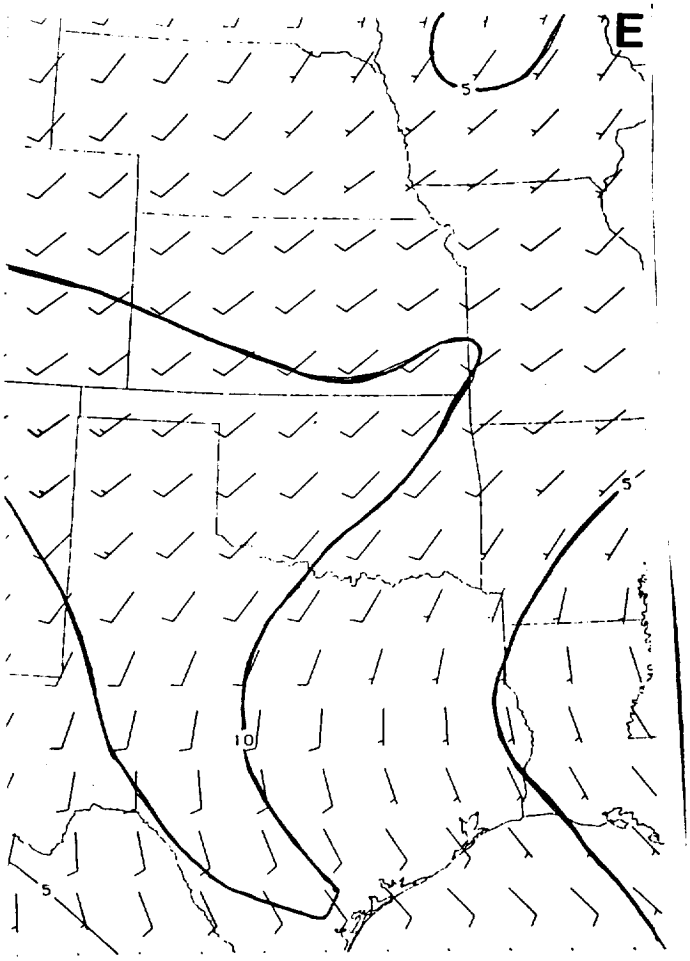

950816/0900 850 MB Interpolated RAOB Winds

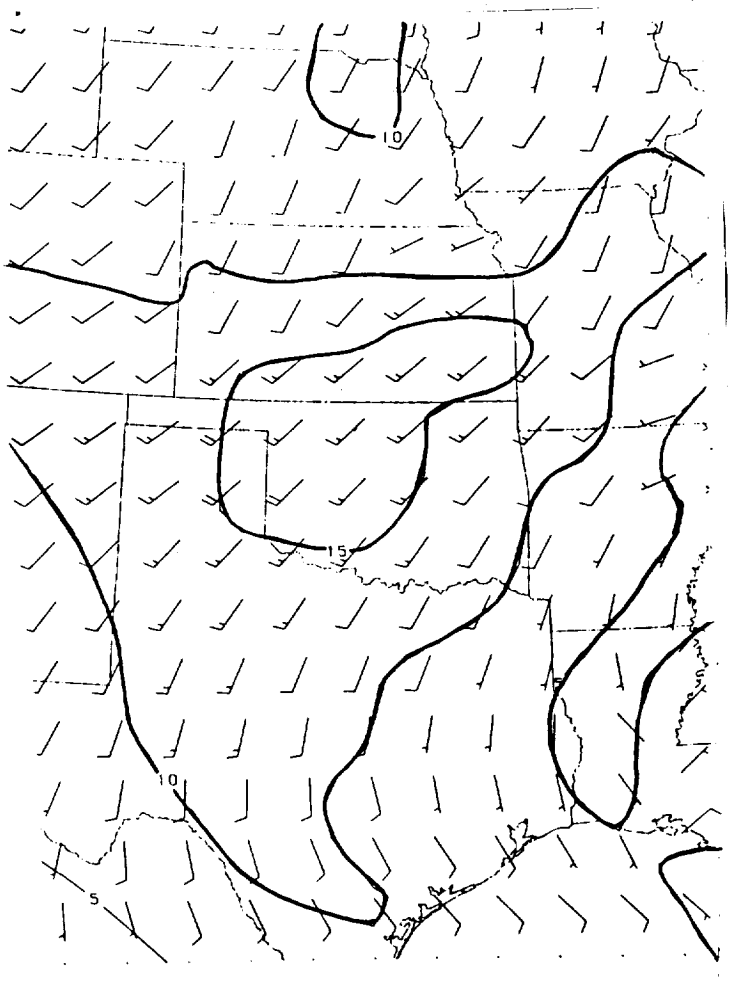

950816/0900 850 MB Profiler Winds

FIG. 23E

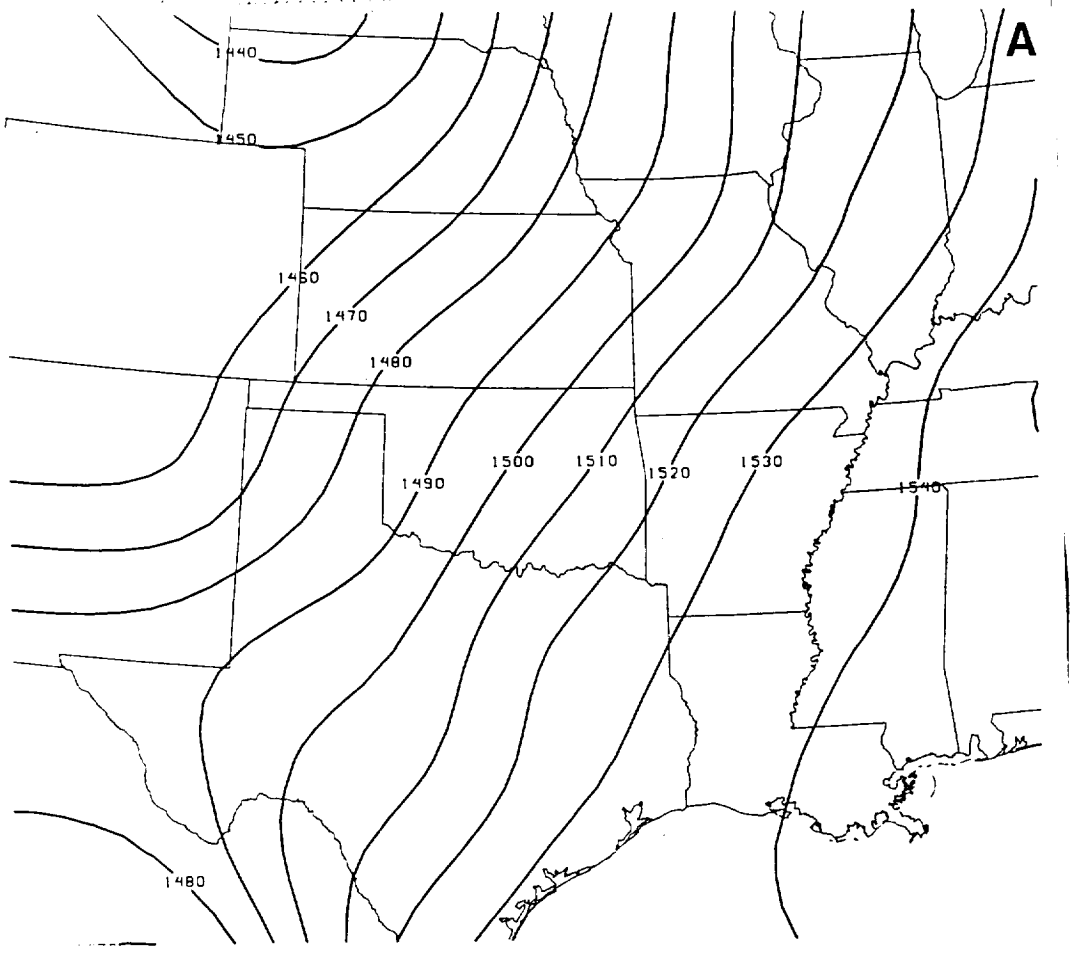

950816/0300 850 MB Interpolated RAOB Heights

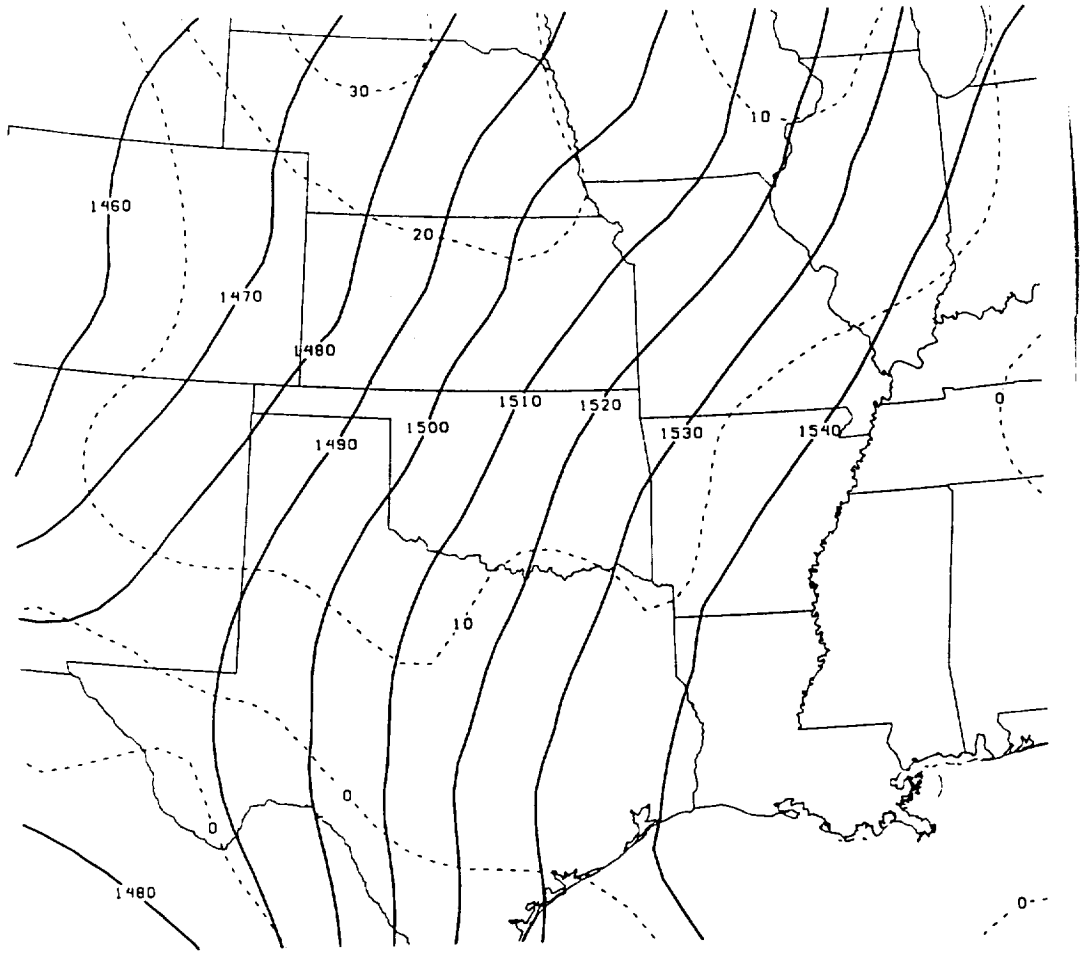

950816/0300 850 MB Derived Height & (Derived-RAOB)

FIG. 24A

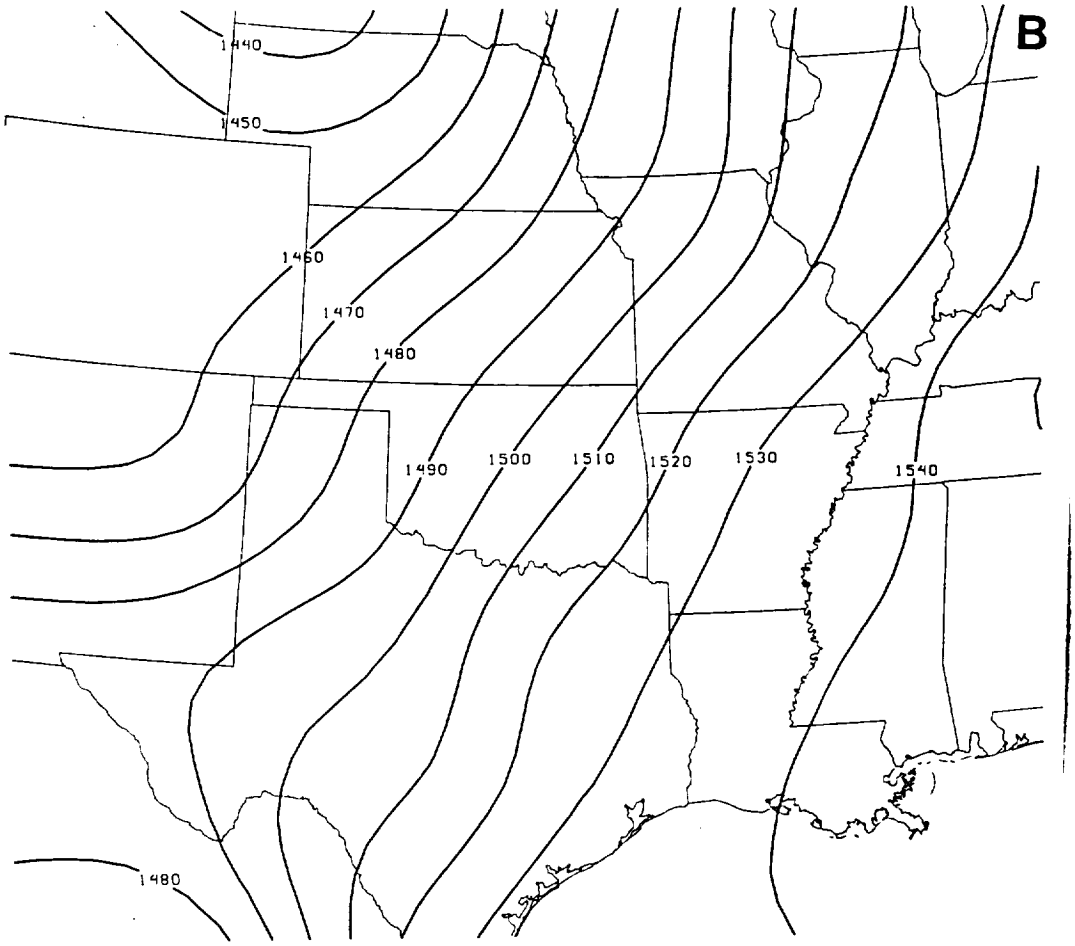

950816/0400 850 MB Interpolated RAOB Heights

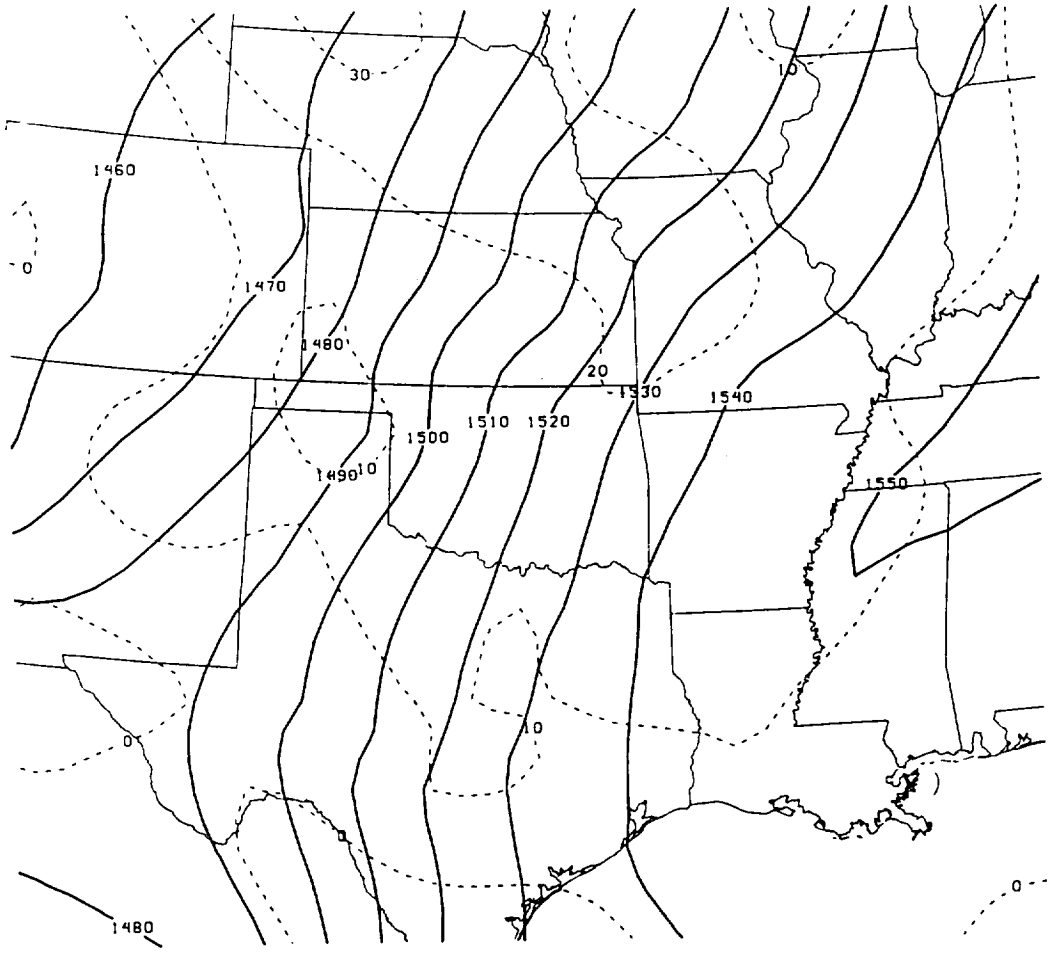

950816/0400 850 MB Derived Height & (Derived-RAOB)

FIG. 24B

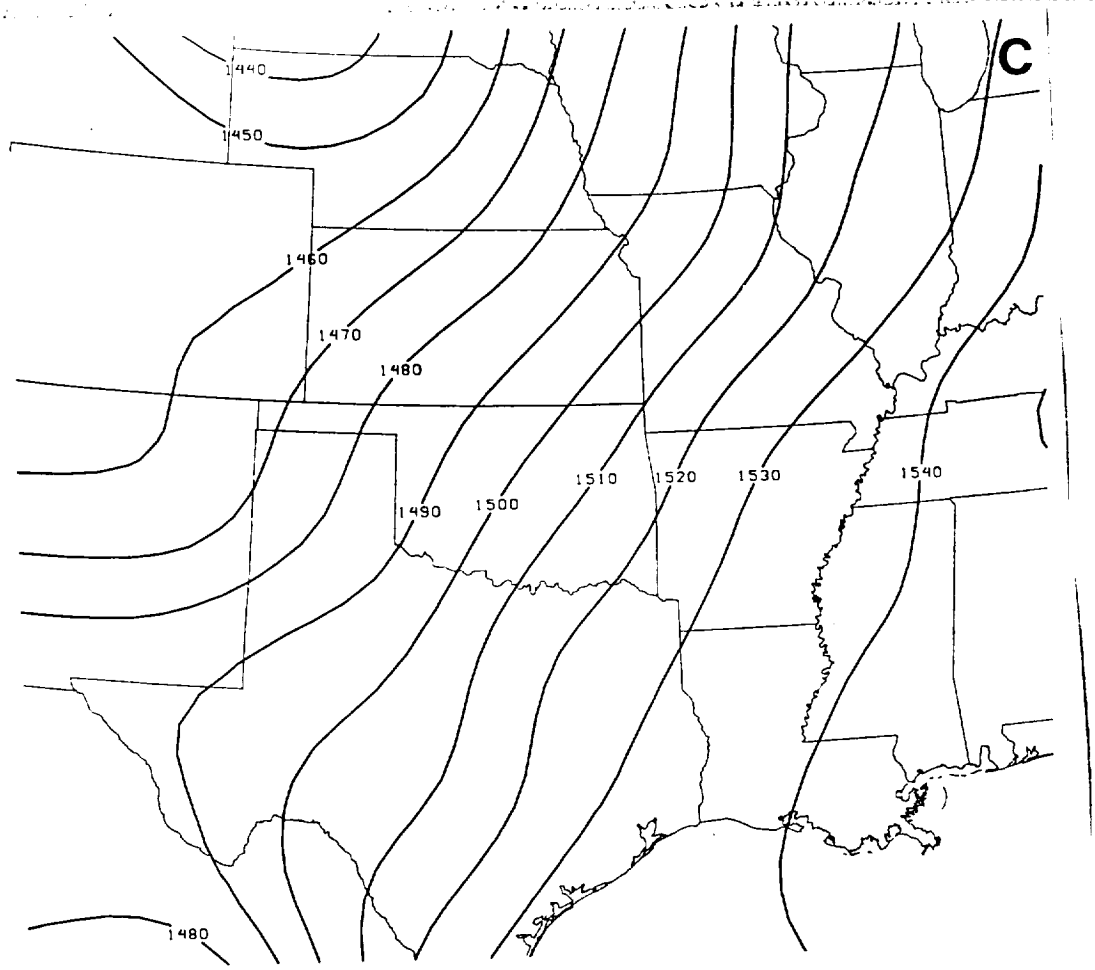

950816/0500 850 MB Interpolated RAOB Heights

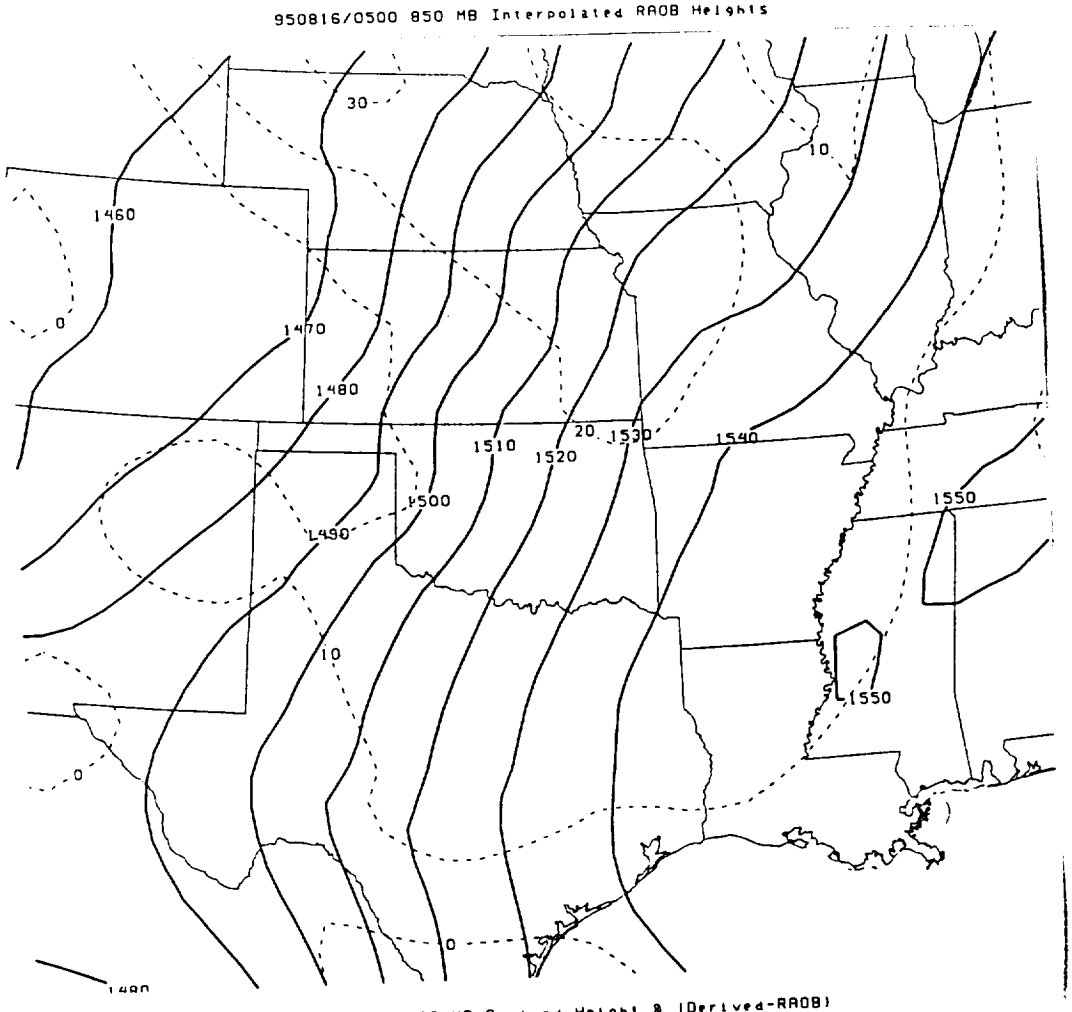

950816/0500 850 MB Derived Height & (Derived-RAOB)

FIG. 24C

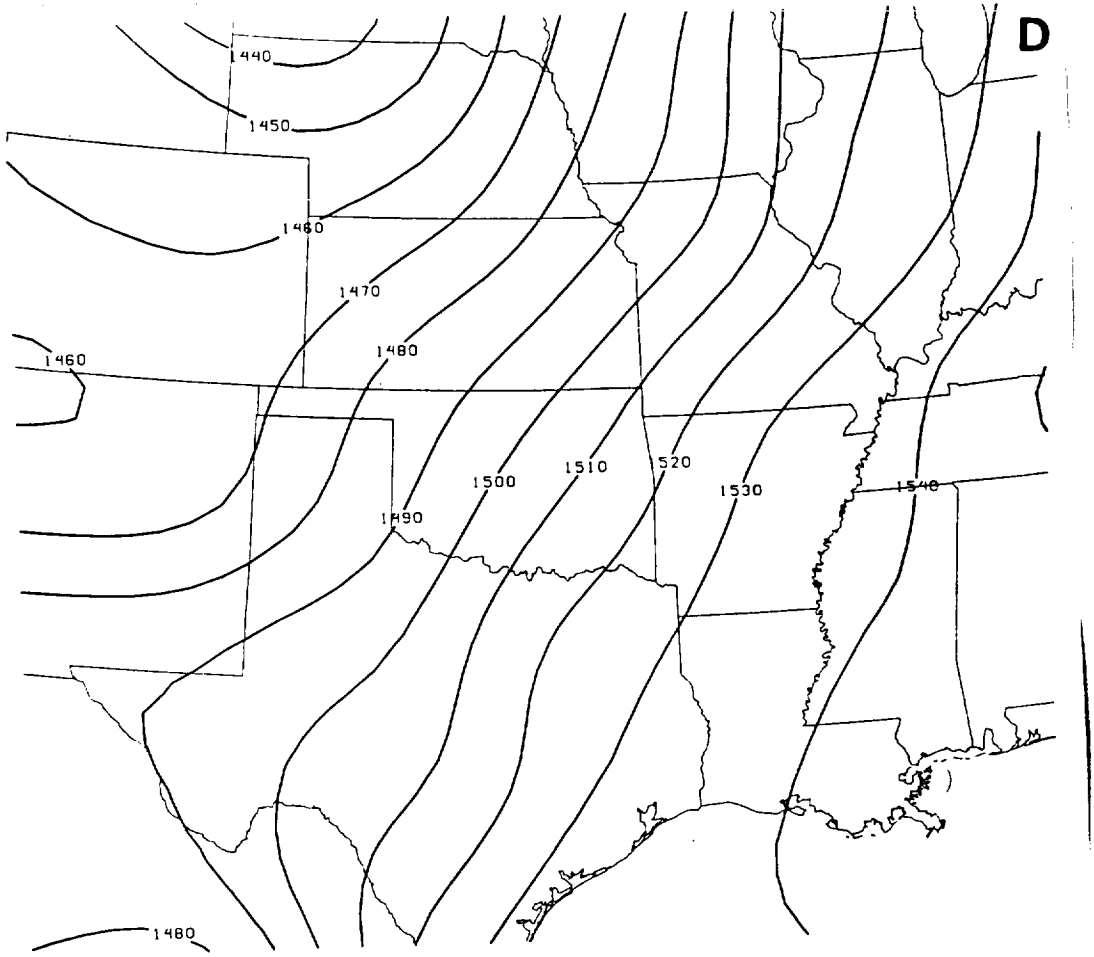

950816/0600 850 MB Interpolated RAOB Heights

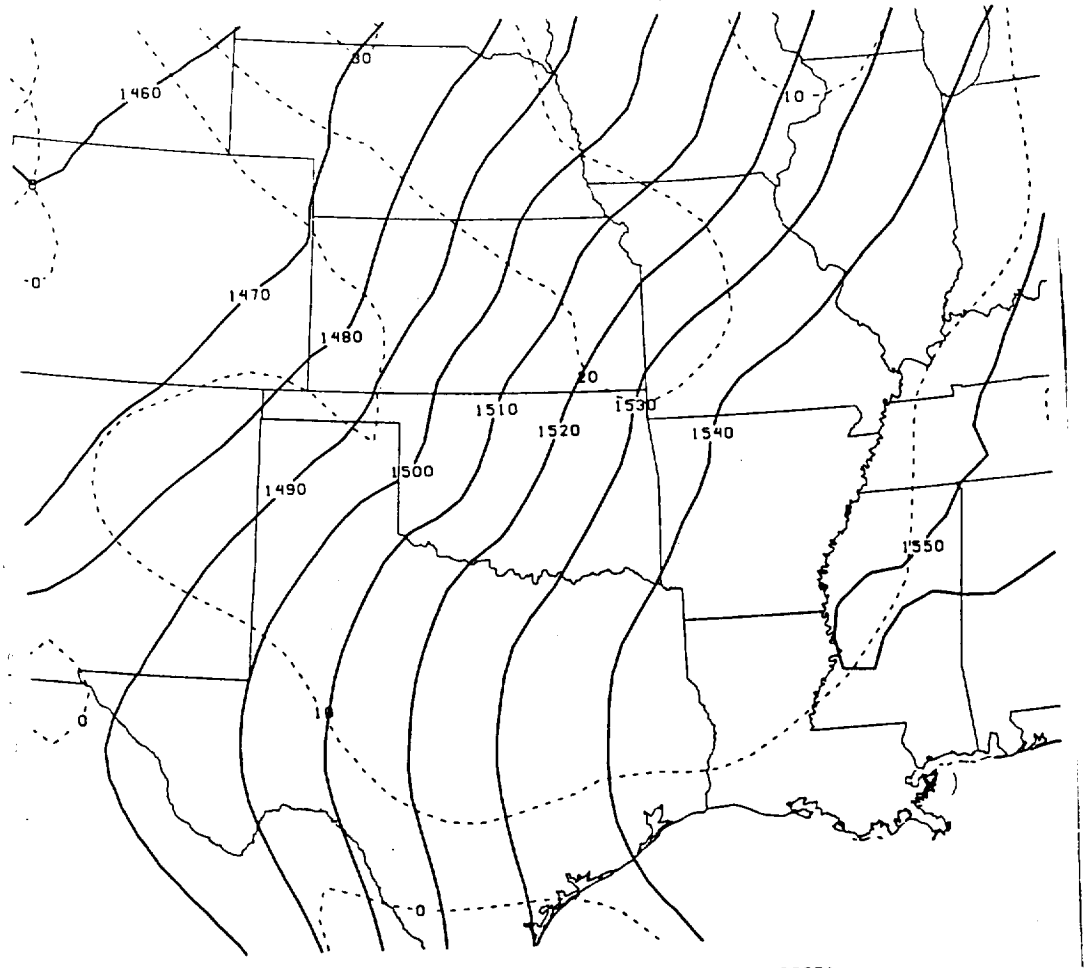

950816/0600 850 MB Derived Height & (Derived-RAOB)

FIG. 24D

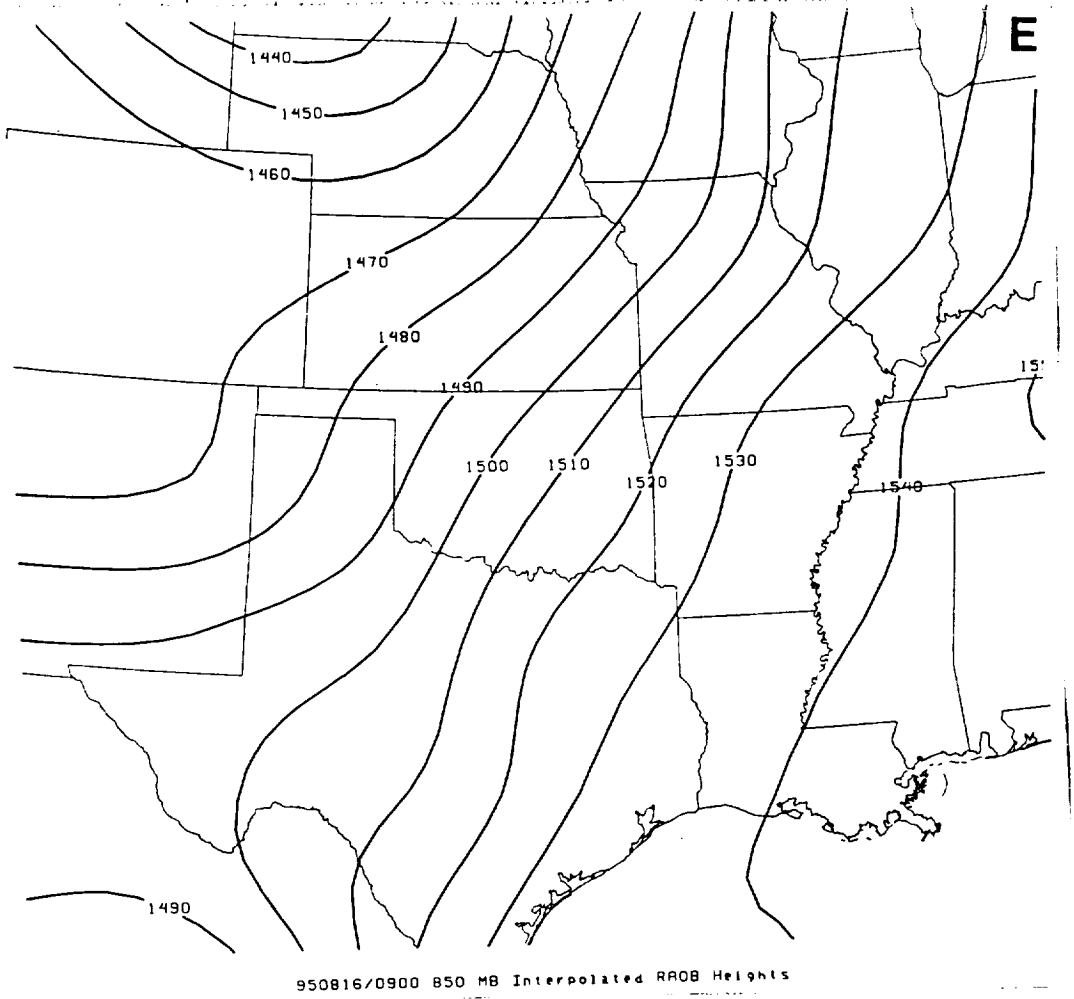
E
1440
1450
1460
1470
1480
1490
1500
1510
1520
1530
1540
1490
950816/0900 850 MB Interpolated RAOB Heights

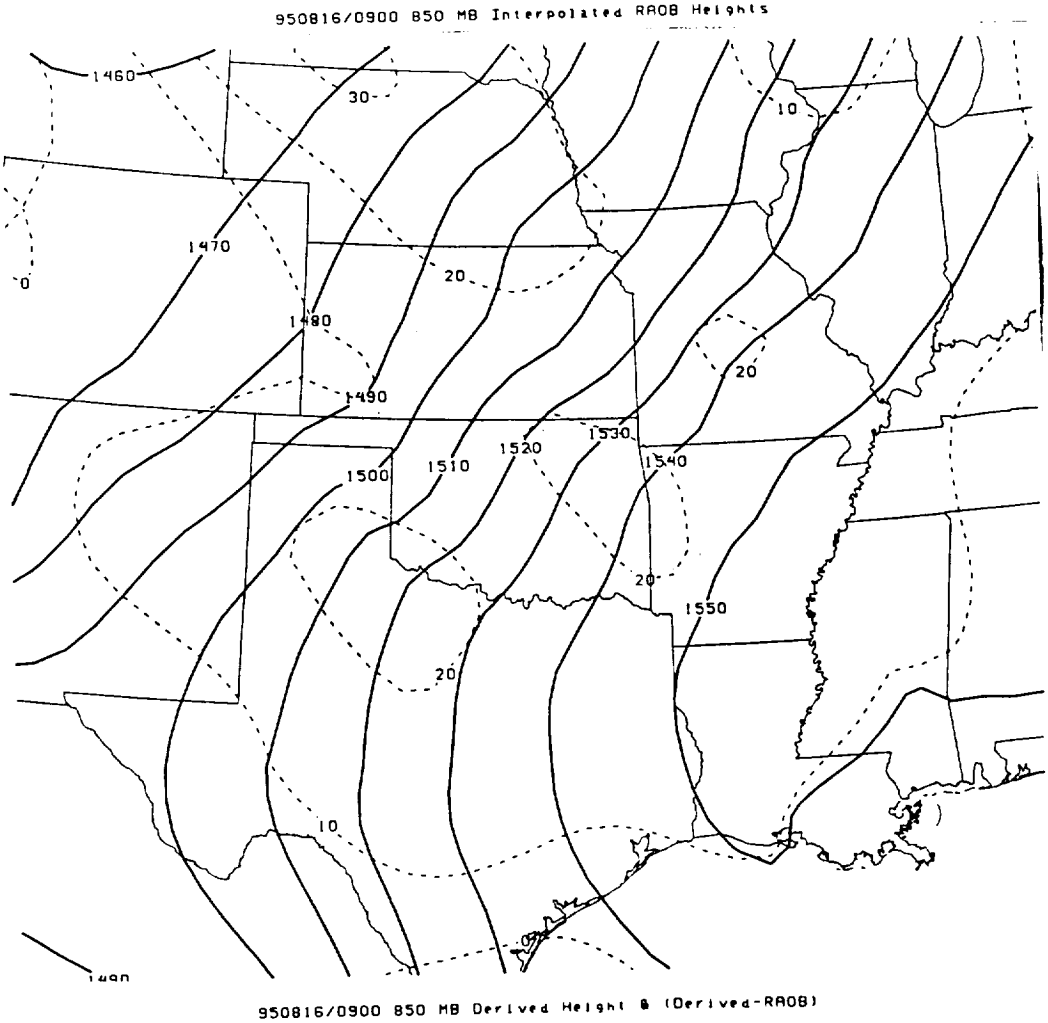
1460
30
10
1470
0
20
1480
1490
20
1530
1520
1510
1500
1540
20
1550
20
10
950816/0900 850 MB Derived Height & (Derived-RAOB)

FIG. 24E

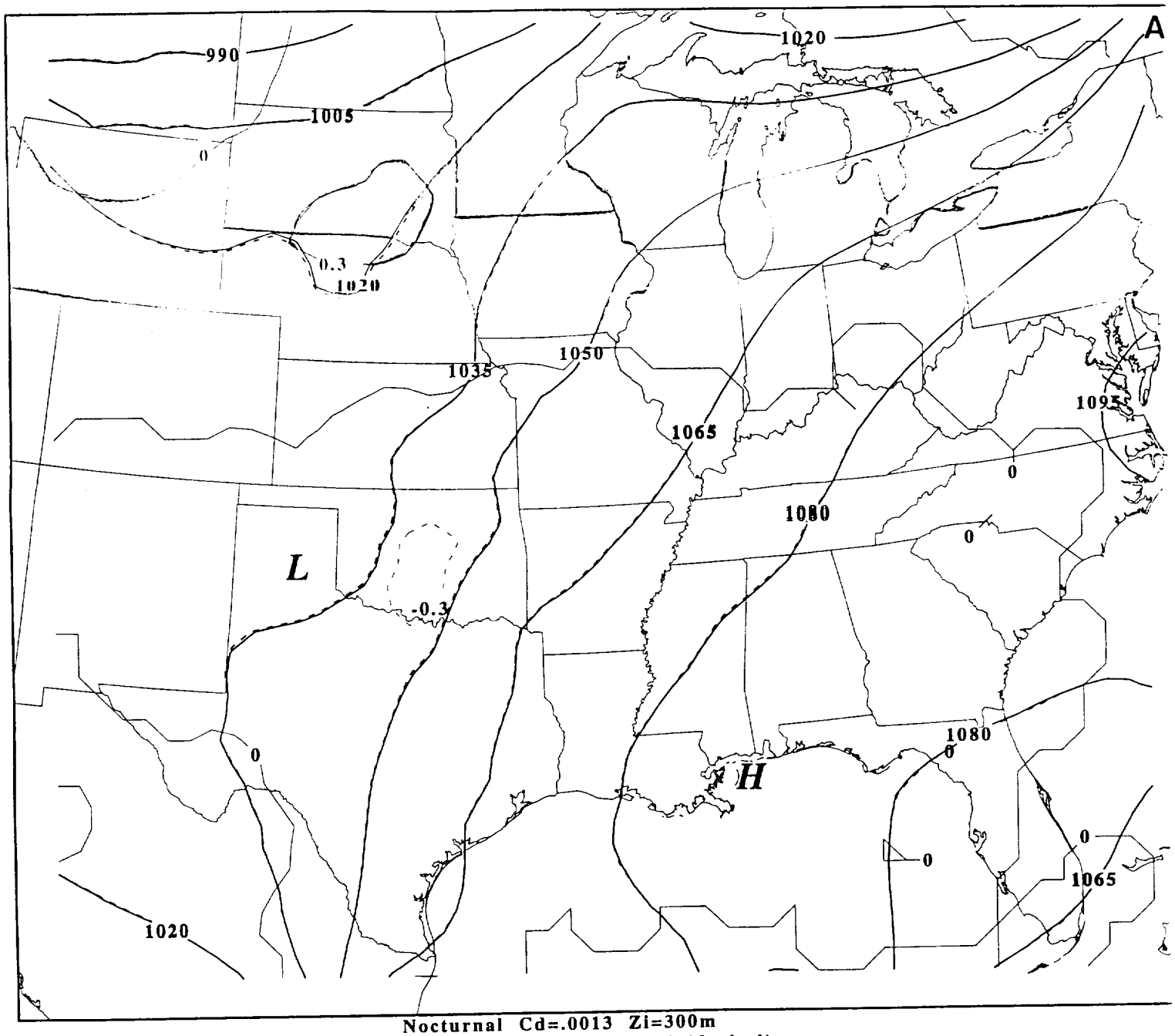

Nocturnal Cd=.0013 Zi=300m
950815/0900 900 MB No Fric(solid) Fric(dashed)

FIG. 25A

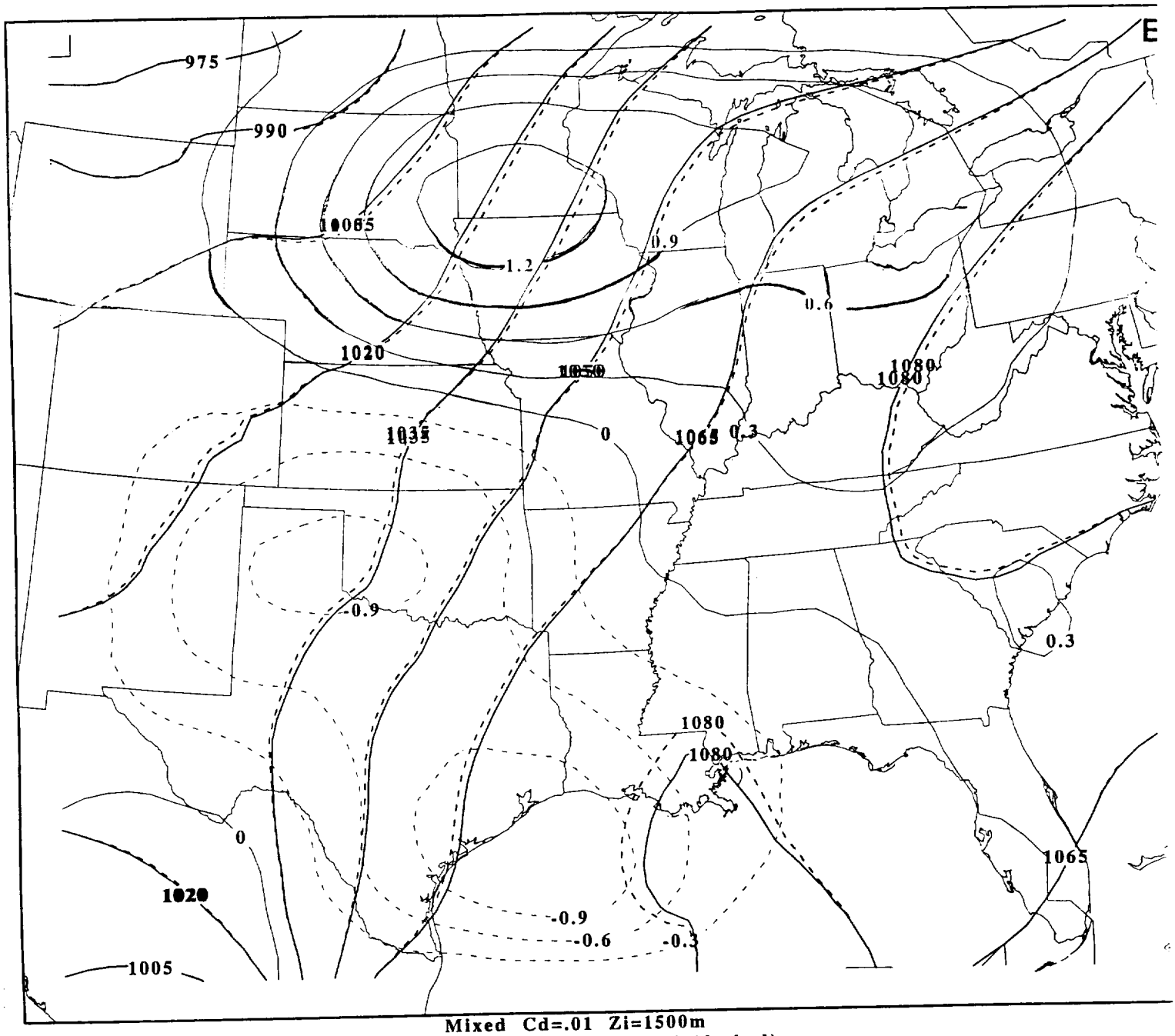
975
990
1006
1.2
0.9
0.6
1020
1050
1080
1080
1035
0
1065
0.3
-0.9
0.3
1080
1080
0
1020
1065
-0.9
-0.6
-0.3
1005
Mixed Cd=.01 Zi=1500m
950815/1900 900 MB No Fric(solid) Fric(dashed)

FIG. 25B

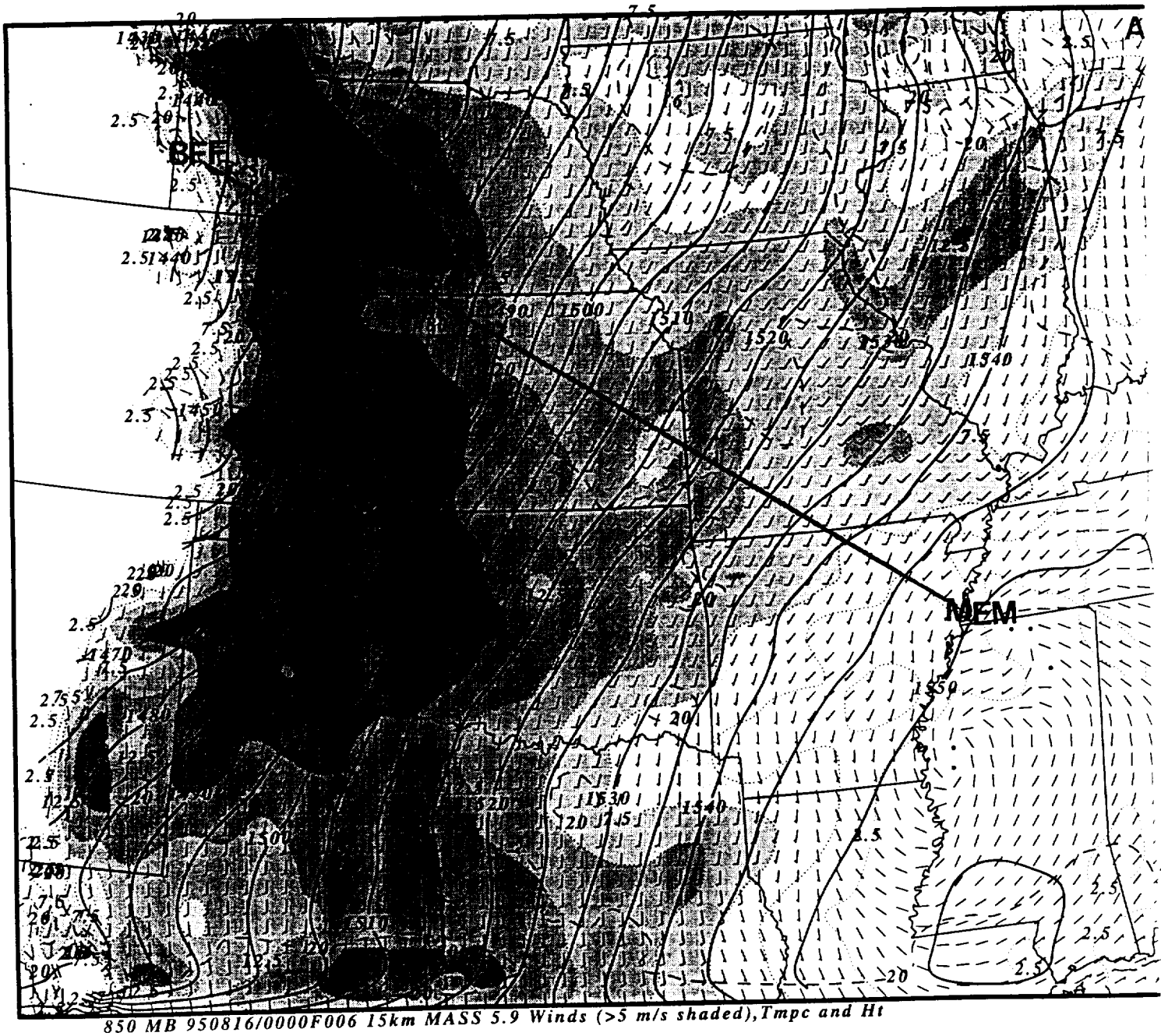
MEM
850 MB 950816/0000F006 15km MASS 5.9 Winds (>5 m/s shaded),Tmpc and Ht

FIG. 26A

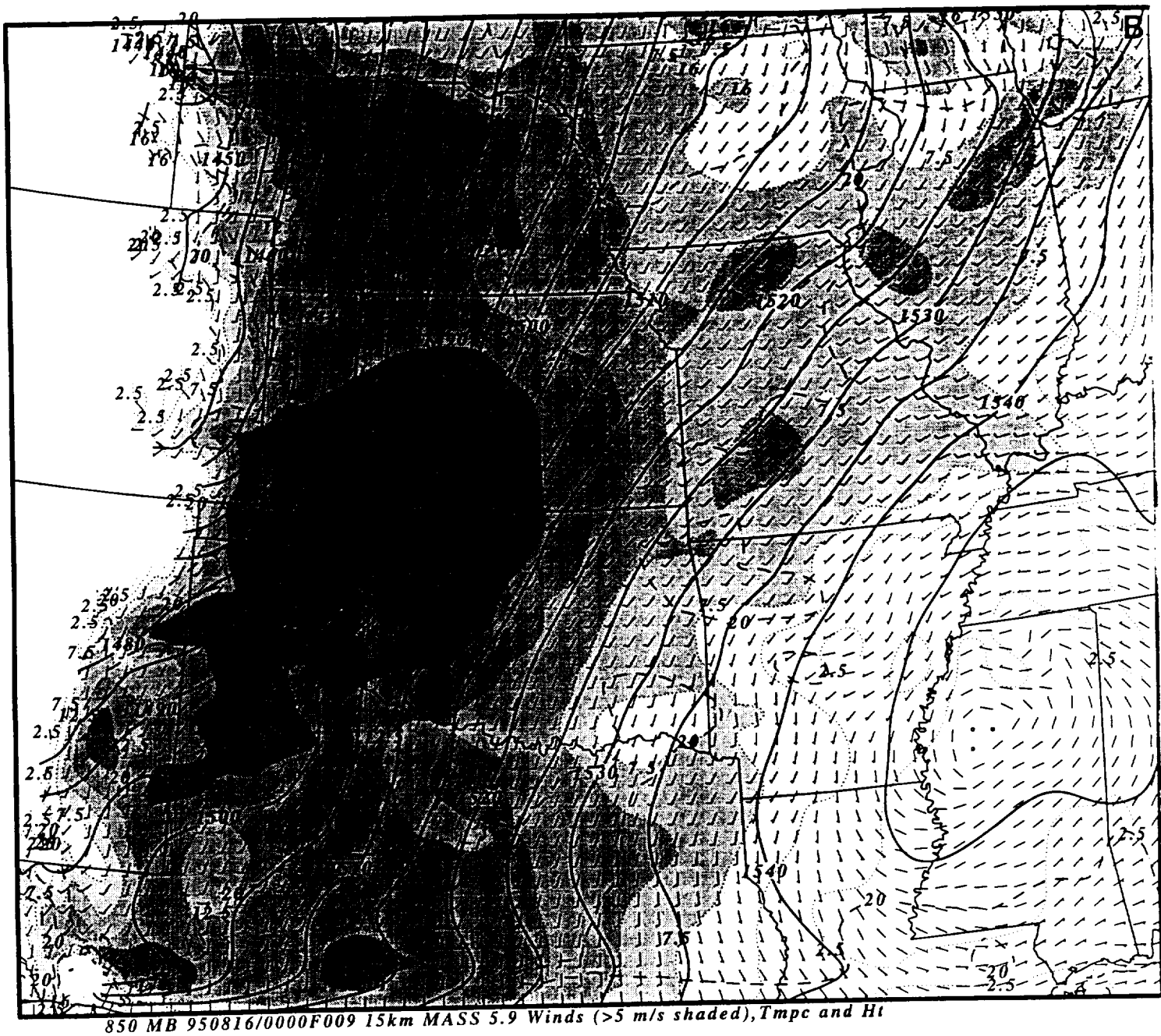

850 MB 950816/0000F009 15km MASS 5.9 Winds (>5 m/s shaded), Tmpc and Ht

FIG. 26B

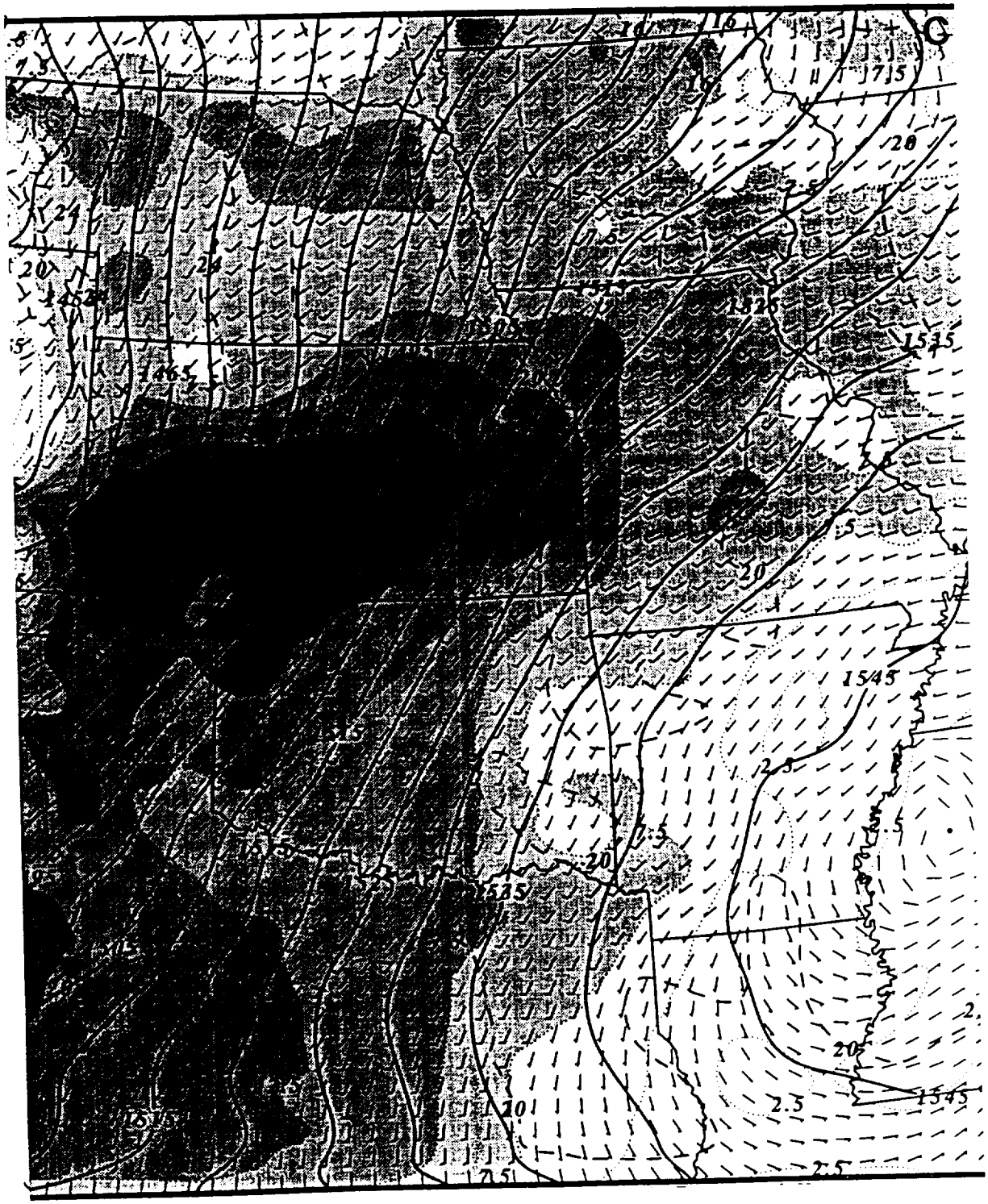
G
1515
1520
1525
1530
1535
1540
1545
1550
1555
1560
1565
1570
1575
1580
1585
1590
1595
1600
1605
1610
1615
1620
1625
1630
1635
1640
1645
1650
1655
1660
1665
1670
1675
1680
1685
1690
1695
1700
1705
1710

D

FIG. 26D

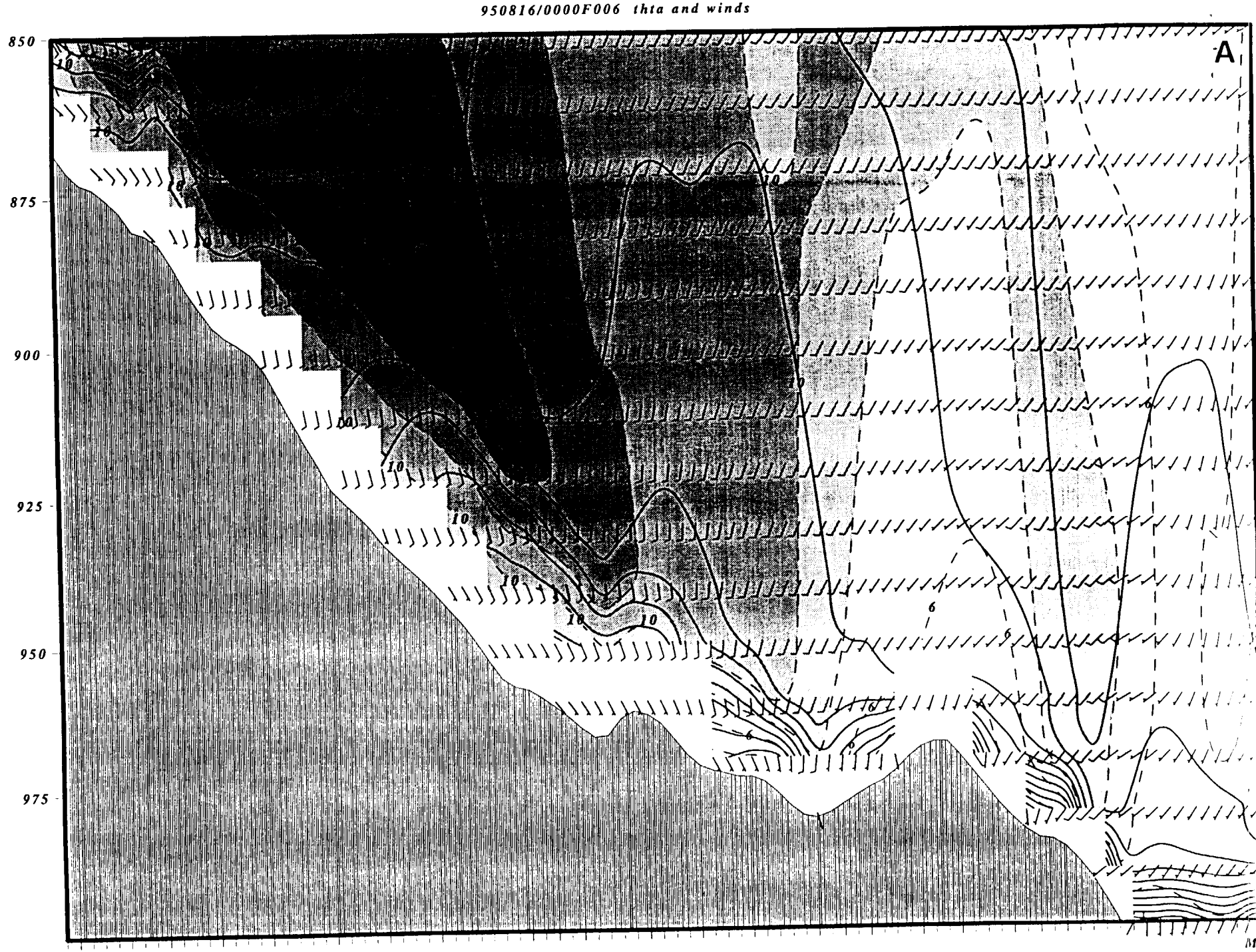

FIG. 27A

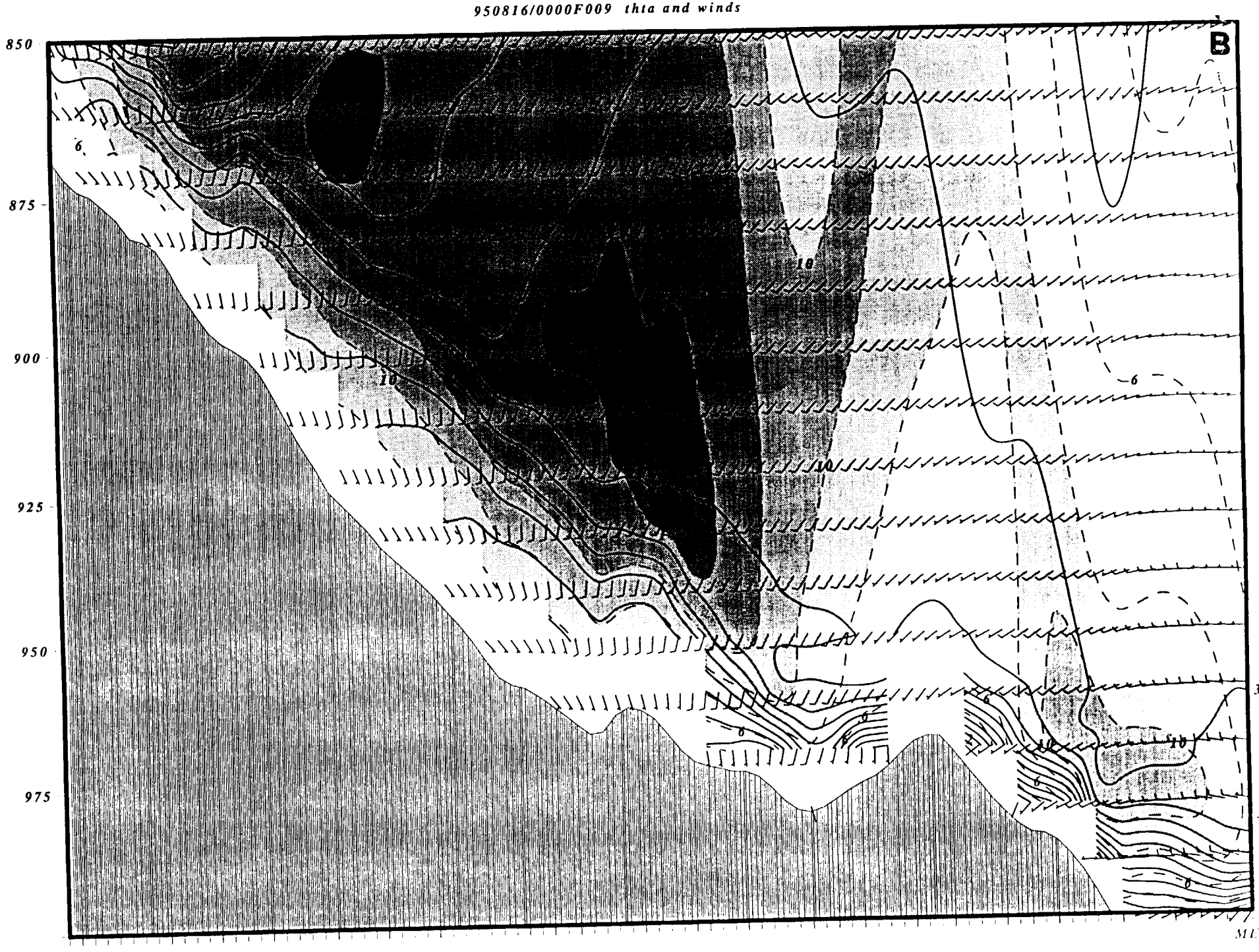

FIG. 27B

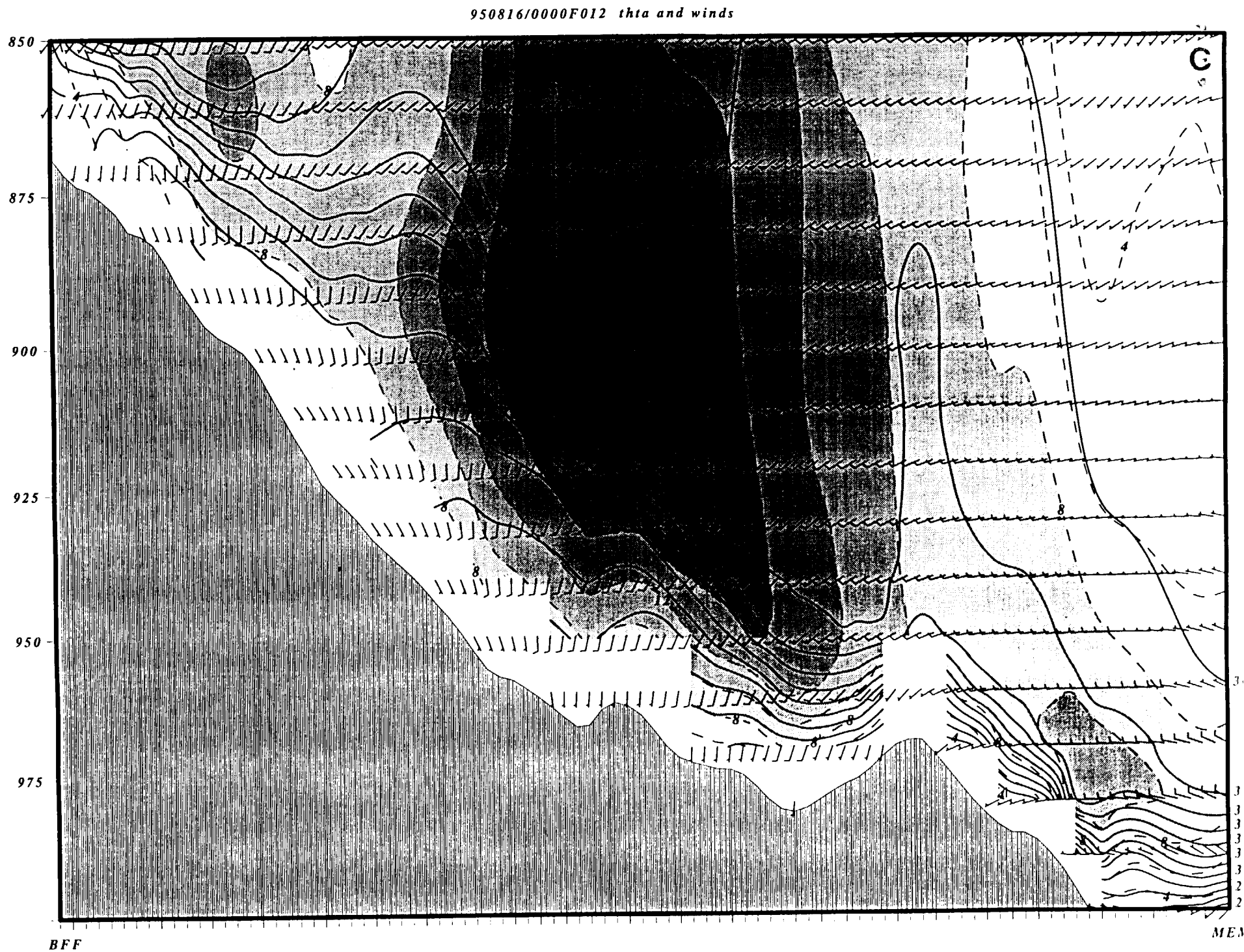
950816/0000F012 thta and winds
850
875
900
925
950
975
C
BFF
MEM

FIG. 27C